UNIVERSITÀ DEGLI STUDI DELL'AQUILA
DEPARTMENT OF CIVIL, CONSTRUCTION-ARCHITECTURAL AND ENVIRONMENTAL ENGINEERING

Ph.D. Course in Civil, Construction-Architectural and Environmental Engineering

Curriculum Civil Engineering

XXXIII cycle

Doctoral Thesis

DEVELOPMENT OF NEW WIRELESS SENSORS AND METHODS FOR CIVIL ENGINEERING APPLICATIONS

SSD ICAR/09

Candidate

CHIARA CASTORO

Coordinator

Prof. MARCELLO DI RISIO

Tutor

Prof. AMEDEO GREGORI

A.A. 2019/2020

UNIVERSITÀ DEGLI STUDI DELL'AQUILA

Department of Civil, Construction and Environmental Engineering

DOCTORAL THESIS

Development of new wireless sensors and methods for civil engineering applications

Ph.D Course in Civil, Construction and Environmental Engineering

XXXIII cycle

Candidate

Chiara Castoro

Thesis Tutor

Amedeo Gregori

January 2022

Development of new wireless sensors and methods for civil engineering applications

Chiara Castoro

Amedeo Gregori

Reviewers:

Alp *Caner*
Leqia *He*

Development of new wireless sensors and methods for civil engineering applications

Chiara Castoro
Candidate ID number: 256967

Department of Civil, Construction and Environmental Engineering- DICEAA
University of L'Aquila

Website: http://diceaa.univaq.it/

To my mom and dad,
to my strength that always guides me.

[Blank page]

Acknowledgements

The PhD scholarship was co-financed with resources from the 2014-2020 National Operational Program (CCI 2014IT16M2OP005), European Social Fund, Action I.1 "Innovative Doctorates with industrial characterization".

Firstly, I would like to express my gratitude to my advisor professor Amedeo Gregori for the support, for his guidance and expertise.

Besides my advisor, I would like to thank all the professors and colleagues who collaborated with me providing insight and expertise that greatly assisted the research. I thank the reviewers for their valuable comments and great expertise.

I thank all my fellow lab-mates, especially Micaela, for the stimulating discussions, for the support, for the hard days we were working together, and for all the fun we have had during these years. I also thank my friends and colleagues from Fuzhou University for sharing a very short but fantastic experience together.

Finally, I thank my partner Ernesto and all my family for supporting me morally throughout the entire Ph.D period, especially during the writing of this thesis, and throughout my life in general.

[Blank page]

Abstract

In the proposed research, effective and innovative monitoring solutions inspired by the principles of low cost, miniaturization, system energy autonomy, and measurement reliability, for remote and widespread monitoring of historical and civil structures in general, have been developed and tested. The advantages of new wireless measuring methods over traditional wired technologies and devices have been investigated. New methods and devices have been proposed for different monitoring purposes. These methods and devices have been developed and tested trough experimental campaigns, in laboratory and in situ, and have been validated with wired traditional techniques for comparison.

The new measuring principle of a new RFID-enabled wireless strain gauge has been tested in static and dynamic conditions, respectively by measuring the elastic modulus of three different materials and by measuring induced environmental vibrations on a steel cantilever. The accuracy of the proposed new technique has been proved to be high, reaching a maximum interrogating distance of 20 meters in laboratory and outdoor, very suitable for structural monitoring.

The use of commercial UHF-RFID tags for civil engineering purposes has been investigated, specifically for the monitoring of out-of-plane displacements, representing an application novelty since commercial tags are usually used in logistics and other purposes. The feasibility of the application of this technique was assessed by laboratory and in situ experimental campaigns. The response of the Tags in laboratory environment demonstrated to be very satisfactory, proving that the application of these wireless RFID tags is feasible, potentially very reliable. In situ experiments showed a weaker response of the Tags due to environmental interference caused by the high presence of metal which affected negatively the transmission of the electromagnetic signal, and consequently the indirect measurements of displacements. Despite some limits, the application is promising and opens up new scenarios for the design of new wireless tags suitable to meet the required needs.

A new wireless RFID sensor for crack width monitoring has been developed and tested in laboratory through a three-point bending tests on different materials. Compared to traditional crack-width measurement procedures, the proposed new technique results to be potentially more suitable, with an interrogation distance up to 1.5 m in this raw state, which could be extended more to allow the positioning of these devices in points difficult to access by traditional wired sensors.

The devices are currently in a raw form and require technological development in order to be applied on large scale. Some critical aspects related to the strong influence of metal can be overcome in future steps of design of the sensors and further investigation is surely required.

In this thesis a large-scale approach to wireless structural monitoring has been also investigated. A sensor network with commercial wireless tri-axial MEMS accelerometers was deployed on the deck of a butterfly-arch stress-ribbon pedestrian bridge located in Fuzhou, Fujian, China, to record the structural response under ambient vibration and perform dynamic identification, finite element modelling and parametric updating. A satisfactory agreement between the model prediction

and the experimental data was achieved. The most accurate model has been chosen to be used as baseline for long-term monitoring of the bridge. In the SHM field, this last study demonstrates the importance of the modelling strategy in simulating the dynamic behaviour of complex structures, as the one considered in this research, in comparison to traditional ones which can be modelled following simplified modelling procedures.

[Blank page]

Sommario

La ricerca proposta intende sviluppare e testare soluzioni di monitoraggio innovative ed efficaci ispirate a principi di basso costo, miniaturizzazione, autonomia energetica e affidabilità di misura, per il monitoraggio remoto e diffuso di strutture storiche e civili in generale. Si sono messi in luce i vantaggi dell'utilizzo dei nuovi metodi di misurazione wireless rispetto alle tecnologie e ai dispositivi cablati tradizionali. Nella tesi sono stati proposti nuovi metodi e dispositivi per diversi scopi di monitoraggio. Questi metodi e dispositivi sono stati sviluppati e testati attraverso campagne sperimentali, in laboratorio e in situ, e validati con tecniche tradizionali cablate per il confronto.

Il nuovo principio di misura di un estensimetro wireless con tecnologia RFID incorporata è stato testato in condizioni statiche e dinamiche, rispettivamente misurando il modulo elastico di tre diversi materiali e misurando le vibrazioni ambientali indotte su un'asta in acciaio. L'accuratezza di questa nuova tecnica si è dimostrata elevata, raggiungendo una distanza massima di interrogazione di 20 metri in laboratorio e all'aperto, molto adatta per il monitoraggio strutturale.

L'applicazione di tag UHF-RFID commerciali nel campo dell'ingegneria civile, è stata proposta per il monitoraggio di spostamenti e deformazioni fuori dal piano di pareti in muratura. Questi tag sono solitamente utilizzati nella logistica per altri scopi e l'applicazione nel campo dell'ingegneria civile costituisce una novità. La fattibilità dell'applicazione di questa tecnica è stata valutata mediante campagne sperimentali di laboratorio e in situ. La risposta dei Tag in ambiente di laboratorio si è dimostrata molto soddisfacente, dimostrando che l'applicazione di questi Tag RFID wireless è fattibile e potenzialmente molto affidabile. Esperimenti in situ hanno mostrato una risposta più debole dei Tag a causa dell'interferenza causata dall'elevata presenza di metallo nell'ambiente, che ha influenzato negativamente la trasmissione del segnale elettromagnetico e di conseguenza le misure indirette degli spostamenti. Nonostante alcuni limiti, l'applicazione è promettente e apre nuovi scenari per la progettazione di nuovi tag wireless adatti a soddisfare le esigenze richieste.

Un nuovo sensore RFID wireless per il monitoraggio dell'apertura di lesione è stato sviluppato e testato in laboratorio attraverso prove di flessione a tre punti su diversi materiali. Rispetto alle tradizionali procedure di misura dell'apertura di lesione, la nuova tecnica proposta risulta essere potenzialmente più adatta, con una distanza di interrogazione che nello stato attuale raggiunge 1,5 m, ma potrebbe essere ulteriormente estesa per consentire il posizionamento di questi dispositivi in punti di difficile accesso con i tradizionali sensori cablati.

I dispositivi si presentano attualmente in forma grezza, e richiedono uno sviluppo tecnologico per raggiungere una prototipazione ed essere applicati su larga scala. Alcuni aspetti critici legati alla forte influenza del metallo possono essere superati nelle future fasi di progettazione dei sensori e si rendono quindi necessarie ulteriori indagini.

In questa tesi è stato anche studiato un approccio su larga scala al monitoraggio strutturale wireless. Una rete di accelerometri MEMS triassiali wireless è stata disposta sulla passerella di un ponte pedonale a nastro con archi a farfalla situato

a Fuzhou, Fujian, in Cina, per registrarne la risposta strutturale in condizioni di vibrazione ambientale ed eseguire quindi l'identificazione dinamica, la modellazioneagli elementi finiti e l'updating parametrico. La previsione del modello e i dati sperimentali hanno raggiunto un confronto soddisfacente. Il modello più accurato è quello che sarà utilizzato come riferimento per il monitoraggio a lungo termine del ponte. Nell'ambito del monitoraggio strutturale, quest'ultimo studio dimostra l'importanza della strategia di modellazione nella simulazione del comportamento dinamico di strutture complesse, come quella considerata in questa ricerca, rispetto a quelle tradizionali che possono essere modellate seguendo procedure di modellazione semplificate.

[Blank page]

Table of contents

List of Figures

List of Tables

Introduction

The research aims to develop, implement, and apply innovative technologies for remote and widespread monitoring of the historical cultural heritage and civil structures in general, inspired by the principles of low cost, miniaturization, system energy autonomy, and measurement reliability. The importance of the theme was strongly highlighted by the recent major seismic events that affected Italy (Abruzzo 2009; Emilia-Romagna 2012; Central Italy 2016). These events, in fact, have confirmed the high seismic hazard of the territory and the high vulnerability of the historic buildings, highlighting the significant constructive deficiencies of the vast architectural heritage, which are often the result of slow processes such as progressive degradation under daily environmental actions (pollutants, thermal effects, etc.). For the conservation, protection, and enhancement of the historical cultural heritage and for its tourism promotion as well as safe usability, it is necessary to propose intelligent and widespread monitoring solutions, to intervene according to the principles of early warning. The same is valid for civil structures in general.

1.1 Background and motivations

Structural Health Monitoring (SHM) is nowadays resorting to intelligent monitoring systems to study the characteristics and the evolution of damaged infrastructures or the behaviour of the structures under loading and fatigue as well as material aging. To obtain a distributed assessment of the structural condition, several sensors are spreaded over the structure, preferably wireless sensors which permit a fast and easy installation even in measurement points difficult to access.

Wireless Sensor Networks (WSNs) are largely used for this scope as their use is also growing in aeronautical vehicles and in industrial equipment to monitor several parameters (e.g. vibration, temperature). WSN nodes are generally battery-powered and are equipped with an embedded microprocessor which allows the digital read of the sensor and the data storage while the data transmission is performed by a wireless communication device. Although the unitary cost of a node is in general relatively low, the deployment of a WSN has a not negligible cost when the number of nodes is large. The life span of these wireless sensors is mainly limited by the battery's life so that the wireless link makes use of low power radiation (typically) to save energy but, consequently, the sensor node does not support high data rate streaming of sensor data and is subjected to data loss. For

these reasons, passive wireless sensors (i.e., without power supply) gain a growing interest in SHM applications. They usually consist of a sensing unit and a data transmitting unit. The sensing unit changes its impedance in accordance with the variation of the physical quantity under measurement. This change of impedance shifts the resonant frequency of the circuit where the sensing unit is connected. The frequency shift is remotely measured using an additional interrogation unit. Recently, the research investigated the use of antennas operating at microwave frequency as wireless sensing units. They have a long lifetime without or negligible maintenance and can be widely distributed or embedded everywhere. The main novelty in these devices is the lack of a specific sensing unit, in fact the antenna is itself the sensor. Some include a Radio-Frequency IDentification (RFID) microchip to perform the modulation of the back-scattered signal. The small change of the shape of the antenna in consequence of the forces applied to the structure where the antenna is stuck on shifts the resonance frequency of the antenna that is remotely detected by means of a power measurement or, equivalently, a measurement of the change of the radar cross section of the antenna. With the fast development of wireless communication and microelectronic technology, the low cost and low power of wireless sensors is emerging as a promising alternative solution for rapid and low-cost sensors deployment in a structural monitoring system.

1.2 Objectives of the research

The proposed research intends to develop effective monitoring solutions, technologically advanced and applicable on the small and large scale, to attract economic investments, including private ones, and satisfy the economic, social, and safety needs of the territory. Specifically, the objectives of the research are to develop and apply new wireless technologies capable of performances similar, or superior, to traditional ones for the structural health monitoring of buildings. In this research, the advantages of wireless systems over wired systems and the advantages of new wireless measuring methods and devices over the existing wireless devices and technologies are investigated. Some important aspects which are the innovation goals of the research are represented by:

- The use of a wireless technology to eliminate the need for wiring and to allow reading of the devices even at considerable distances and in places that are difficult to reach.
- The application of a new measurement principle for environmental and engineering quantities using new knowledge in the field of electromagnetic and microelectronic.
- The use of Ultra High Frequency (UHF) RFID wireless devices, which operates at 867/868 MHz. This means reduced interference because the devices operate in a different frequency bandwidth compared to the frequencies of commercial wireless devices (usually 2.4 GHz, the same frequency of Wi-Fi, Bluetooth, etc.).
- Low cost of the proposed devices, with a respective lower cost of the overall monitoring system and his maintenance.
- Miniaturization of the devices. The small size of the instrumentation, which can be reduced to that of a 1 cent coin, makes the installation of a large

number of devices particularly suitable for large-scale monitoring of monumental and historical buildings which are often characterized by surfaces not compatible with traditional instruments.

- Energy autonomy and reduced maintenance required by devices and data transmission systems.

- Versatility of the devices regardless of the material (stone, wood, brick, etc.) and the type of structure (bridges, buildings, artwork, historical monument, etc.).

1.3 Organization of the thesis

The thesis is organized as follows:

Chapter 1 introduces the aims and scopes of the research, with respect to the theoretical background on the topic.

Chapter 2 reviews the state of the art of the Structural Health Monitoring (SHM) describing the SHM systems and applications and the role of wirless sensor networks (WSNs) in SHM.

Chapter 3 describes the application of a new wireless strain measuring method and investigates his effectiveness through experimental campaigns. The new sensor is a RFID-enabled semi-passive wireless strain gauge which is capable of measuring deformations with accuracy and precision comparable to that of wired sensors, reaching long distances, and capable of measuring even dynamic phenomena. This sensor, already patented by the University of L'Aquila, is a prototype which uses a battery activated only for the necessary measurement time via RFID technology. Young's elastic modulus measurements were carried out on three different materials using the wireless strain gauge and the results were compared with those obtained using wired sensors. A calibration of the sensor was applied. The feasibility of this new method was confirmed by the unique relationship between the deformation values and the measured frequency variations. In comparison with a traditional measurement procedure, the accuracy of the proposed new technique is potentially higher considering an interrogation distance of up to 20 meters, which is certainly suitable for structural monitoring. Furthermore, the measurement method was also validated in dynamic conditions, by measuring the vibration induced on a steel cantilever anchored at one end to a steel staircase. The strain measurement was carried out with the wireless strain gauge sensor and with the simultaneous reading of a laser, resulting quite precise and sensitive compared to the latter. The results of the research are presented and discussed.

Chapter 4 presents the application of commercial wireless RFID tags (which are generally used in logistics, retail, healthcare, and waste management to return information on the traceability and identification of the objects on which they are applied) in civil engineering applications. In particular, for this study the UHF RFID tags were used to monitor the displacements of two brick walls 2.70 m high and 1 m wide, subjected to out-of-plane actions induced by a concentrated load along the middle of each wall. The innovation of this research is represented by the novelty of the application of this type of sensors in civil engineering. These tags are 90 mm x 17 mm in size, with a thickness of 38 μm. They were positioned following a 3x2 grid on each wall, and a displacement transducer was positioned

to validate the measurements. Despite some technology limits, the application of these commercial devices in civil engineering areas is promising and opens up new scenarios for the design of new wireless devices suitable to meet the required needs. The potential use of this new measurement technology allows the advantage of a wireless, low-cost, non-invasive, and completely passive widespread monitoring.

Chapter five describes the development and application of a new wireless RFID sensor for crack width monitoring. The device, conceived together with the Industrial and Information Engineering and Economics department (DIIIE) of the University of L'Aquila, is a RFID tag with bifilar transmission line. To evaluate the effectiveness of the proposed measuring method and device, an experimental campaign was carried out. In particular, three-point bending tests were carried out on bricks of three different materials (unreinforced mortar, reinforced mortar with PVA fibers, and reinforced mortar with basalt fibers) to monitor the crack width opening. Crack width measurements were carried out using the wireless crack meter and, at the same time, a wired displacement transducer for comparison. The feasibility of this new method was confirmed by the relationship between the deformation values and the measured frequency variations. In comparison with traditional crack width measurement procedure, the accuracy of the proposed new technique is potentially higher considering in this raw state a starting interrogation distance of 1,5 meters (that can be considerably increased with an improved version of the device), which is certainly suitable for structural monitoring. These new devices are in a raw form and require technological development to be applied on a large scale but their potential in structural monitoring could be very high.

Chapter six proposes a large-scale approach to wireless structural monitoring. It is a study developed in collaboration with Fuzhou University, in Fuzhou, China. The dynamic identification and Finite Element (FE) modelling of a butterfly-arch stress-ribbon pedestrian bridge located in Fuzhou University was developed. The current case study is the first example of this structural system in China and not many others of this particular kind are present worldwide, representing a good example of building heritage to protect. The aim is to investigate the dynamic behaviour of the structure and develop a highly accurate FE model which can serve as baseline for long-term monitoring of the bridge during its life cycle. A highly synchronous tri-axial wireless sensor network was deployed on the bridge deck to record the structure's ambient vibration and through Stochastic Subspace Identification method an estimate of the operational modal parameters was achieved. Eight stable modes were found, associated with prevalent bending and torsional deformations. Four distinct FE models of the bridge with progressive complexity and accuracy were developed. The most accurate FE model was used for the automatic parametric optimisation based on a sensitivity algorithm with 8 parameters. The effect of non-structural elements (handrails) and the effect of prestress on the modal features were also investigated. The results of the research are presented and discussed. The most accurate developed FE model yielded a good representation of the dynamic behaviour of the structure and can be used as the baseline for a long-term monitoring of the bridge during its life cycle.

Finally chapter 7 summarizes concluding remarks and shows future perspectives.

State of the art of the SHM applications and systems

2.1 Structural Health Monitoring (SHM)

The aging of civil structures is a major issue in the construction industry. The prediction of a realistic lifetime of an existing structure in service is an important issue to reduce costs for the future. Therefore, it will be necessary to determine the real lifetime of structures which is often much longer than that estimated by the usual theoretical models. Most structures can be used much longer than their calculated life cycle and this reduces the overall costs of the structures. The process of continuously monitoring the status of a structure to detect damage is known as Structural Health Monitoring (SHM).

The importance of health monitoring of civil structures has gained considerable attention over the last three decades. A variety of methods have been employed for SHM, which have improved over time with the evolution of the relative technology. Structural health monitoring can be defined as the diagnostic monitoring of the integrity conditions of a structure. The intent is to detect and locate damage or degradation in structural components and to provide this information quickly. The damage may result from fatigue, earthquakes, strong winds, explosions, material aging, etc. Early detection of damage or structural degradation prior to local failure is important in order to prevent catastrophic failure of the system.

2.2 SHM applications and systems

The first modern SHM applications began within the aerospace industry during the late 1970's and early 1980's. Since as early as 1980, SHM and vibration-based damage assessment of bridges and buildings have existed in the civil engineering community (Farrar and Worden, 2006). More recently, with advances in SHM technology, SHM has expanded throughout the engineering disciplines, making it more interdisciplinary than ever before. A complete and successful SHM application, therefore, must also consider the socio-organizational and nontechnical challenges which are highly interrelated with both the fundamental knowledge needs and technological needs (Catbas et al., 2004).

Damage detection refers to a broad research area, and it can be utilized for

different purposes, such as validation of the properties of a new structure and long-term monitoring of an existing structure. Damage detection is also a key component of SHM, with a variety of existing research studies which explore various detection methods. A thorough review of civil SHM applications and associated damage detection methods can be found in Brownjohn et al. (2004). In order to detect damage, it is first necessary to define what is meant by the term damage. Any structural or material change that affects the behavior of the structure adversely and shortens its operation life may be considered damage. In this thesis, the types of damage measured thorough the use of wireless sensors are limited specifically to those most commonly experienced by civil infrastructures and buildings: deformations, cracks opening, boundary condition changes and local stiffness losses. However, the type of damage capable of being detected, using the new methodologies presented in this thesis, is not limited to only these types. Any damage resulting from a structural or material change that affects the dynamic properties of a structure during the monitoring period, in theory, can be identified using the presented methodologies.

Development of novel damage detection methodologies, coupled with introduction of new sensor technologies provides the opportunity to expand the damage detection options available in the context of SHM. It is widely accepted that a single sensing technology or data analysis method cannot solve every SHM problem. Therefore, the study presented in this thesis will serve to contribute to the existing methodologies and sensors.

Being a multidisciplinary field of research spanning over three decades, a tremendous variety of research exists. Much of this research has been either purely analytical or only laboratory based, however, research demonstrating full-scale application of SHM systems has become more common as of recently. In the past, signal reliability and power supply issues were serious limiting factors for application of wireless sensors on a full-scale. Research contributions and technological advances in wireless sensor technology have begun to offer wireless sensors as a viable alternative to their wired counterparts (Farinholt et al., 2010), although, there are still major questions to be answered. Utilization of wireless sensors encourages further development of damage detection methodologies.

2.2.1 Wireless sensor networks for structural monitoring applications

Traditionally, SHMs are composed of a network of sensors distributed throughout a structure. The networks generally rely on a central source of power and data acquisition which requires cables to link the sensors with the power and acquisition hardware hub. Positioning the cabling is very expensive and time consuming (Celebi, 2002). Even a small system consisting of 10 to 15 sensor channels installed in a building can cost thousands euros per sensor channel. However, larger monitoring systems are more commonly used, often with 100 or more sensors, in long-spanning bridges. The larger number of sensors is typically used because the size of the structure is large and the points where the sensors are installed are generally difficult to access. Moreover, in the event of an earthquake or other extreme events, wired links are prone to break, resulting in unreliability of the data links.

To avoid the many downfalls of wired systems, the use of wireless technologies called Wireless Structural Health Monitoring Systems (WSHMS) has been proposed

for structural monitoring (Straser et al., 1998). Initial interest in wireless sensors was motivated by their low cost. Undoubtedly, the elimination of extensive lengths of wire gives wireless structural monitoring systems the advantage of easier installation and substantially reduced costs (Lynch and Loh, 2006).

The structural monitoring of large and complex infrastructures requires the use of a number of specific sensors distributed on a large area or volume to form a monitoring system composed of independent or interconnected sensor nodes like a smart skin. Because of the complexity of that monitoring system, some kind of intelligence is required to make easy the managing of the system and the handling of the large amount of measured data. In particular, the communication between the sensor nodes and a managing unit that collects and stores the information gathered from the sensors spread over the structure is a critical issue that preferably has a solution with wireless systems. In fact, wireless sensors permit a fast and easy installation even in points difficult to access while their cost is lower than that of a wired system.

Wireless sensor networks (WSNs) are favorite candidates for structural health monitoring (SHM) of large structures. As already discussed in the previous section, as an interdiscipline consisting of sensor, communication, and wireless technology, WSNs were initially applied in the military and then extended to environmental monitoring, agriculture, medical treatment, and civil engineering (Jeong et al., 2010; Lin et al., 2007; Liu and Yuan, 2008; Lynch et al., 2003; Melik et al., 2008, 2009; Mitchell et al., 1999; Mohammad and Huang, 2011; Park et al., 2008; Spencer, 2003; Straser et al., 1998; Yu et al., 004a,b).

A variety of wireless sensor networks communication technologies have been investigated in recent years. Straser et al. (1998) expressed one of the earliest attempts to develop a wireless structural health monitoring system for civil infrastructures. Recently, advances have been made in the development of wireless smart sensor and actuator technology. The wireless sensor developments may reduce the need for visual inspection as a method of assessing structural integrity and reduce potential safety risks in large civil structures such as highways, bridges and buildings.

The advantage of the wireless sensor networks technology is the smallness of the devices, the flexibility of the network structure and also an easier implementation of the network through the wireless communication unit. Moreover, the cost of the device is low, and it becomes possible to process information in a decentralized manner. With these characteristics, wireless sensor networks add more value than other technologies; they create networked systems that are scalable (because of the possibility to more easily increase the number of devices in the network) and robust (because if a node in the network fails, the remaining nodes can still perform the global task).

Various types of sensors have been developed during the past decades (such as strain-gauges and optical fiber sensors) while SHM technology is becoming important in a wide range of technical fields, most of the time in combination with structural use of special composites and high-performance materials (Gasco et al., 2011). Actually, it is more and more understood as the SHM system can improve safety and reliability of structures by autonomously monitoring the conditions or detecting critical damage. In Liu and Yuan (2008), authors state that in comparison with traditional wired sensor networks, wireless systems for SHM have numerous advantages in terms of better flexibility, software or hardware

expandability, cost effectiveness, and fault tolerance. Interesting applications of wireless sensors made in aerospace, civil, and environmental engineering are discussed in Chang et al. (2003); Ibrahim and Cumming (2011); Kesavan et al. (2008); Tata et al. (2009) comparing the practical needs concerning space requirements and cost increments with those of traditional wired techniques. In Son et al. (2006), the use of WSNs has been presented as a useful tool even in forest fire surveillance, allowing real-time acquisition, evaluation, and analysis of environmental information including temperature, humidity, sound, vibrations, and smoke as well as pictures of buildings and forest. Some advances in research, development, and implementation of smart sensor networks and health monitoring systems for civil infrastructures are presented in Ou (2006) and in Yu and Ou (2008). In particular, cases of study of WSNs and their integrated systems and implementations in offshore platform structures, hydraulic engineering structures, large span bridges, and large space structures have been reported. Other researches on wireless sensing technology applied to SHM for buildings and civil engineering structures for damage detection are discussed in Dyke et al. (2000). During the entire last decade, implementation of wireless transmitters for continued structural damage monitoring became a promising research field to be often related to new patented inventions and devices. In SMbulletin (2002), the authors present a new methodology for operating a monitoring system that provides near-real-time structural condition assessment for extreme events and long-term deterioration information, using MEMS-type accelerometers. This proposed structural monitoring system comprises modular, battery-powered data acquisition devices which transmit structural information to a central data collection and analysis device over a wireless data link. Data acquisition devices comprise mechanical vibration sensors, data acquisition circuitry, wireless transmitter, and battery. For sophisticated analysis after a natural hazard or extreme event, the authors suggested that powerful computers may be interfaced with the central device.

WSNs have been extensively investigated in recent years and many practical challenges are still to be faced when employing such a technology for many SHM applications (Lynch and Loh, 2006).

A new wireless strain measuring method

3.1 Introduction

As previously said, many practical challenges are still to be faced when employing WSNs for SHM applications. In fact, a WSN must remain in operation over multiple decades with maintenance costs low enough to justify its integration into a given structural maintenance strategy. These technical barriers include ensuring reliable power sources for sensor nodes, reducing installation and maintenance costs, and automating the collection and analysis of data acquired by a WSN.

As a possible solution to overcome the mentioned challenges, in Mascarenas et al. (2010) is discussed the use of sensor nodes that collect measurements from a structure in a completely passive manner without any electrical power. In Köppe and Bartholmai (2011), a wireless sensor network with temperature-compensated measuring technology for long-term structural health monitoring of buildings and infrastructures is instead presented. A brief summary and comparison among benefits and disadvantages related to active and passive wireless sensors are given in Jang and Kim (2012) together with the presentation of a passive wireless structural health monitoring sensor made with a flexible planar dipole antenna. In fact, it is understood that chipless passive wireless sensors can give real-time structural information for SHM without space and battery constraints in harsh environmental conditions (Lin et al., 2007; Melik et al., 2008, 2009; Mohammad and Huang, 2011). Chipless passive wireless strain and damage detection sensors based on a frequency selective surface are presented in Jang et al. (2012).

In this chapter, the application and validation of a new kind of sensor node for mechanical stress detection which is obtained as a hybridization of an RFID tag and a resistive strain gauge is reported. The assessment of the sensor tag is demonstrated by means of measurements of the Young's modulus of different materials and by a comparison with the results obtained using a calibrated wired system. A calibration procedure of the new sensor tag is developed, and a detailed measurement campaign using many instrumented specimens is reported. The sensor is validated also in dynamic conditions.

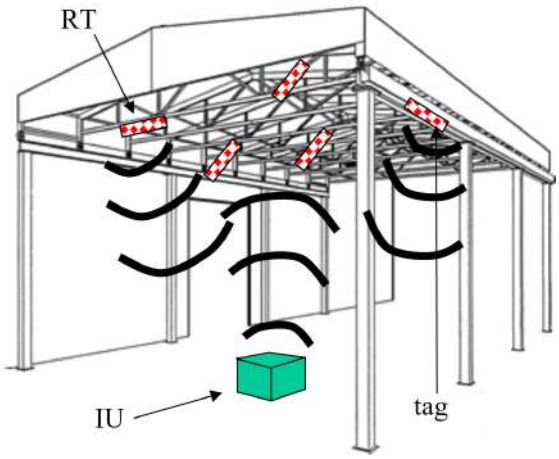

Figure 3.1. Scheme of the measurement set-up. Tags are represented as dotted rectangles; the interrogation unit (IU) is shown as a box on the ground. RT means responding tag.

3.2 RFID-enabled semi-passive wireless strain gauge: hybridization of an RFID tag and a resistive thin-film strain gauge

3.2.1 Description and operation of the device

The new device, which has been tested and validated, is a semi-passive wireless strain sensor tag, which uses a piezoresistive thin-film strain gauge (like a wired sensor), but it can be passively interrogated as an RFID tag. Like in an RFID system, there is an interrogation unit (i.e., a commercial RFID reader) that radiates an electromagnetic wave that impinges on the antenna of the sensor tag waking it up. The strain gauge varies its resistance in accordance with the applied strain and drives an oscillating circuit that modulates the electromagnetic wave back-scattered by the sensor tag antenna. The modulating frequency is dependent on the applied strain and can be easily measured by means of a spectrum analyzer or a frequency meter once the modulated back-scattered wave is received back by the interrogation unit. The prototype of the proposed sensor tag makes use of a battery to power the oscillating circuit that is maintained turned off for all the time except for a short time interval during the measurement interrogation. For this reason, the life span of the battery can be very long. A detailed description of the sensor tag is reported in Di Giampaolo et al. (2016).

Since each sensor tag is autonomous and independent from other nearby deployed sensors, the resulting network has the simple star topology where the central unit is an RFID reader that interrogates one-by-one all the deployed sensor tags.

The overall SHM system consists of an interrogating unit (i.e., a reader) placed in a convenient position (e.g., near the ground in Figure 3.1) and several sensor tags deployed on the structure to be monitored (e.g., in positions difficult to access). Tags are fixed to the structure; they are designed to remain operative for several years, while the interrogation unit is intended to be portable and placed at the measurement location only when needed (obviously, it can be also used for a permanent monitoring of the structure). All sensor tags are quiescent (i.e., inactive) for all the time except for the short time interval when interrogated. During interrogation, they measure the strain affecting the portion of the structure where each of them is stuck on and send back to the interrogation unit a signal

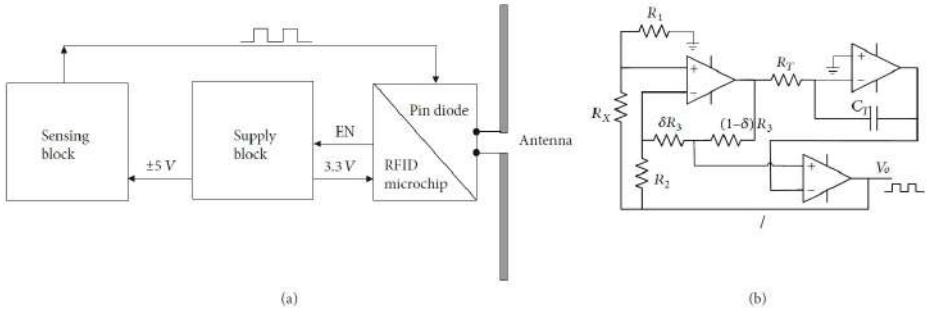

Figure 3.2. (a) Scheme of the sensor tag; three main circuital blocks: an RFID block, a supply block, and a sensing block. The sensor tag is quiescent and can be activated on demand. (b) Schematic of the resistance-to-frequency converter circuit.

encoding the strain measured value. The optimal operation of the system is achieved when the interrogation unit has a line of sight with each sensor tag, but the system is able to work even in non-line of sight conditions. As sketched in Figure 3.1, the distance between the interrogation unit and the sensor tags can be of several meters. Like in logistic applications, the number of tags that can be handled by a single interrogation unit is large (e.g., a commercial reader can interrogate several tags per second), but that number can be larger or smaller in agreement with the repetition time of interrogations. In case of static objects (i.e., the change of the status of the monitored structure is slow compared to the measurement time), the interrogation rate can be low (the number of tags interrogated in the time unit is not an issue), and as a consequence, the number of tags that can be handled by an interrogation unit is limited only by the maximum interrogation distance, i.e., the distance over which the tag is not getting enough power to be woken up. The developed sensor consists of three main circuital blocks: an RFID block, a supply block, and a sensing block as shown in Figure 3.2(a). The RFID block consists of an antenna, a commercial RFID microchip (i.e., an NXP GMiL+), and a pin diode with its feeding network. The antenna is a dipole-like antenna operating at 868 MHz; the pin diode is connected to the antenna terminals by means of a feeding network, and it is used to modulate (on-off) the back-scattered signal. The RFID microchip, powered by an external battery, allows the reading/writing distance of the sensor tag up to 30 m (nominal) and allows the remote control of the voltage level of a logic pin by means of an appropriate writing of the configuration word in its memory. This voltage level is used to switch the supply and sensing blocks on and off.

The sensing block is essentially a resistance-to-frequency converter circuit whose output is a squared wave signal that is used to drive the pin diode connected to the antenna terminals. Under the squared wave signal, the input impedance of the pin diode switches between two values (low and high impedance) performing an amplitude modulation of the electromagnetic wave that is back-scattered by the antenna (Figure 3.2(a)). Since the frequency of the squared wave signal is proportional to the strain gauge stretch, the back-scattered signal, amplitude modulated by the squared wave signal, carries the information concerning the strain measured by the strain gauges. Details of the resistance-to-frequency converter are shown in Figure 3.2(b). It is composed of a full Wheatstone bridge strain gauge circuit (i.e., four piezoresistive thin-film strain gauges like in a wired sensor) and an operational amplifier that amplifies the small voltage changes across the bridge.

Actually, the Wheatstone bridge is a well-known circuit consisting of four resistive arms with resistances R_1, R_2, R_3 and R_4, and an excitation voltage, V_e, applied across the bridge. The output voltage V_o is zero when $R_1/R_2 = R_4/R_3$

and the bridge is said to be balanced. Any change in resistance in any arm of the bridge will result in a nonzero output voltage.

A possible configuration for strain measurements is the so-called quarter-bridge. It has a strain gauge at one arm of the bridge (active arm), e.g., R_4, which is the only changing resistance of the bridge. $R_4 = R_0 + \Delta R$, where R_0 is the unstressed resistance (or nominal resistance) of the strain gauge and ΔR models the strain-induced change in resistance due to an applied strain ϵ.

It is $\Delta R = R_0 \cdot GF \cdot \epsilon$, where GF is the Gauge Factor, i.e., the sensitivity of the strain gauge to strain which for metallic strain gauges is typically around 2. If we assume that $R_1 = R_2$ and $R_3 = R_0$, the output voltage is

$$V_o = \frac{GF \cdot \epsilon}{4} \cdot \left[\frac{1}{1 + GF \cdot \epsilon/2} \right] \tag{3.1}$$

In practice, considering that the strain measurements rarely involve quantities larger than a few millistrain, the output voltage (Equation (3.1)) cannot be larger than a few thousand of the excitation voltage. For these reasons, wired systems resort to an amplification of the output voltage to bring the signal to a level where it can be conveniently handled for indication or recording. In the proposed wireless system, instead, the resistance-to-frequency technique is used in order to codify the strain measurement into a modulation frequency while preserving the high sensitivity of the Wheatstone bridge. A deeper description of the resistance-to-frequency converter is provided in Di Giampaolo et al. (2016).

The unbalance voltage due to the resistance change is then integrated, and its polarity is fed back to the bridge as the bias voltage to sustain the oscillation. The oscillation frequency changes quite linearly with the stretching of the strain gauges. The output of this circuit drives a pin diode circuit for modulating the backscattered signal.

The interrogating unit consists of a commercial RFID reader (the same kind used in logistics) and a spectrum analyzer connected to an antenna and to a personal computer (Figure 3.3); alternatively, we have used a Universal Software Radio Peripheral (National Instruments NI USRP 2920) particularly suited for dynamic measurements. At the start of measurements, the interrogation unit sends, by means of the RFID reader, an electromagnetic wave which delivers both the energy to wake up the tags and a query command to boost the tags to reveal themselves. Awaken tags modulate the electromagnetic wave that scatters back from their antennas with a random numeric code revealing their readiness for communication. Then, the RFID reader performs the inventory of all the responding tags which identify themselves sending back their ID. Once the inventory is completed, the interrogation unit starts with the measurements of the strain gauge status of the inventoried tags.

The measurement procedure is repeated identically for each one of the responding tags and consists of three steps. In the first step, the interrogation unit opens a specific reading/writing session with the i^{th} responding tag identified by means of its ID and enables that tag (with appropriate writing of the configuration word located in the memory of the tag) to switch on the supply circuit block which supplies energy to the sensing block. After that, during the second step, the interrogation unit sends a continuous wave (CW) signal and waits for the signal back-scattered from the tag which delivers the strain gauge status information.

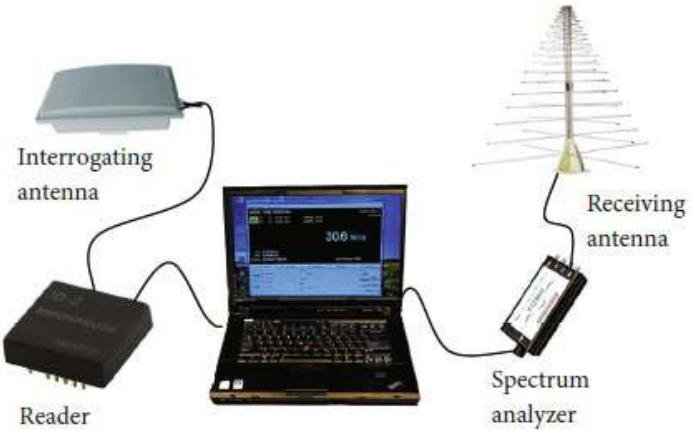

Figure 3.3. The interrogation unit consists of a commercial RFID reader and a spectrum analyzer connected to an antenna and to a personal computer.

In fact, the strain gauge varies its resistance in accordance with the applied strain and drives an oscillating circuit (inside the sensing block) which modulates the electromagnetic wave back-scattered by the tag antenna. The modulating frequency is linearly dependent on the applied strain, so the back-scattered signal has a different frequency modulation in accordance with the strain gauge status. Once the modulated back-scattered signal is received by the interrogation unit, the modulating frequency is easily measured by means of a spectrum analyzer and the strain status is retrieved. Once the strain measurement is completed, the interrogation unit becomes the step three. A new reading/writing session is open to disable (by writing the appropriate memory location of the tag) the supply circuit block, and consequently, the sensing block is switched off. The modulation of the back-scattered signal finishes, and a CW signal arrives to the interrogating unit which closes the communications with that tag and starts to interrogate another inventoried tag repeating the above-described three steps. Therefore, the sensing circuit is kept turned off all the time except for the short time interval during the measurement interrogation.

3.3 Experimental validation of the proposed wireless strain measuring method

3.3.1 Elastic modulus assessment of three different materials: steel, brass, and aluminium

To evaluate the effectiveness of the proposed sensor tag, a campaign of measurements has been performed. Tasks of this experimental activity were the calibration of the sensor and the comparison of the wireless measured data with those achieved with a consolidate method based on wired sensors. Specific tests have been also performed to estimate the maximum interrogation distance for the wireless sensor. Inside a laboratory room, with several obstacles making this environment noisy, the sensor tag was proved to allow for an interrogation distance even larger than 20 meters. To prove the effectiveness of the proposed new wireless strain measurement technique, the elastic properties of three materials have been investigated using wireless sensor tags in place of the wired strain gauges. In particular, the elastic modulus assessment of steel, brass, and aluminium samples, respectively.

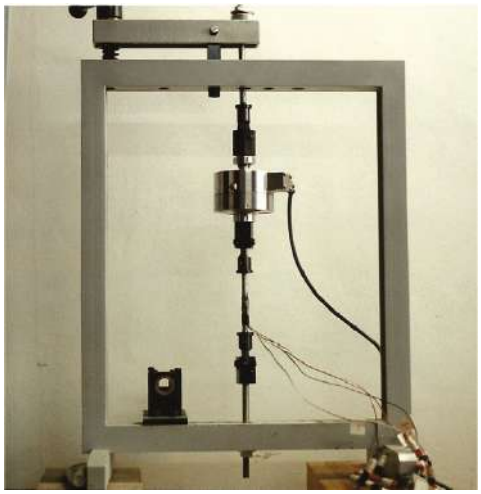

Figure 3.4. Steel frame for the laboratory tests.

These estimations have been first performed in accordance with a common wired strain gauge technology. Subsequently, the estimation of the elastic modulus of the three materials has been repeated on the base of the wireless strain measurements.

The experimental tests were performed in accordance with the wired strain measurement technique, and those concerning the new proposed method have been all carried out operating a specific apparatus. In particular, the experimental apparatus included a manual compensator (working with the principle of the Wheatstone bridge) and a vertical metal frame (Figure 3.4) that mainly consists of a rigid steel-made structure built for a laboratory test and standing in the vertical plane and designed to apply controlled forces up to 10kN in tension. In particular, a manually driven wheel is mounted on the top of the testing frame. The wheel controls a lever mechanism by which a variable tensile force is introduced in the specimen causing it to extend. A load cell mounted in series with the specimens (and electrically connected to the compensator) allows the measurement of the tensile force applied during the tensile test.

Operating the just mentioned apparatus in a proper way, the elastic modulus E (Young's modulus), the shear modulus G, and/or the Poisson's ratio ν of any elastic material can be assessed. So far, only specimens of material previously instrumented with wired strain gauges have been considered for tests.

Three different solid metal pieces made of brass, aluminium, and steel, respectively, have been selected and machined to obtain a couple of identical specimens from each of them. The two specimens of each couple have been assumed to be homogeneous and to univocally represent the same material. To perform tensile tests, the specimens had to be previously worked and instrumented. Once machined, specimens have been characterized from a dog's bone shape, with the two hands kept bigger to secure the specimen to the testing apparatus and to favorite a regular strain diffusion along the central, cylindrical portion of the specimen (stalk) when applying tensile forces. The cylindrical portion of the specimens measures 8 mm in diameter and about 100 mm in length (Figure 3.5).

During the test, the applied tensile forces have been measured and controlled by means of a load cell mounted in series with the specimen and electrically connected to the compensator. The load cell is characterized by a maximum load capacity of 20 kN, a maximum output signal of 4000 mV/V, and a scale factor $k = 2$. The number and the magnitude of the load increments applied during the tensile

Figure 3.5. One of the instrumented steel specimens.

test have been set in accordance with the different strengths and stiffness of the various metal specimens. In particular, load increments have been limited in the range of $0.75 \div 1$ kN (equivalent signal variation: $150 \div 200$ mV/V) and have been repeated several times upward and downward, respectively. A complete load sequence includes a number of steps upward to a maximum load value and an equal number of load decrements downward to a zero load value, so to obtain a closed loop. The maximum applied load has been fixed in advance and kept low enough to avoid the specimens to yield: about half of the yield threshold was reached as maximum stress.

According to the elastic theory, tensile strains resulted in the specimen while loads are being applied. During the experiments, tensile strains have been detected and measured by means of several strain gauges previously mounted on the specimen and electrically connected to the compensator. In particular, each specimen has been instrumented with two single grid strain gauges glued on the opposite side of the specimen, the grids being aligned with the longitudinal axis of the specimen. Common strain gauges 3/120LY4x type, characterized from $R = 120\Omega$ and a scale factor $k = 2$, were adopted.

The number of strain gauges used in each single test varies from two to four according to the half or to the whole bridge configuration, respectively. The reason for multiple gauges mounted on the same specimen first comes from the undesired possibility that applied tensile force could act eccentrically with respect to the ideal longitudinal axis of the specimen. In fact, applied loads acting with casual eccentricities introduce undesired bending actions so that a not uniform strain distribution across the transversal section of the specimen may result. An average signal computed from strain gauges mounted on opposite sides of the same specimen allows to compensate for this undesired effect and accounts for the ideal, uniform tensile strain to be considered in the tensioned specimen. On the other hand, when more arms of the Wheatstone bridge have been made active, the sensitivity of the bridge increased. Moreover, due to a possible temperature change during the test, the need for a second signal compensation rises as well. For this reason, signals from gauges mounted on the loaded specimen are combined with those recorded, at the same time, from gauges mounted on a second, identical specimen kept unloaded. In this research work, both the mechanical and thermal compensations of the strain measurements have been performed at once, recording signals from gauges in a whole bridge configuration.

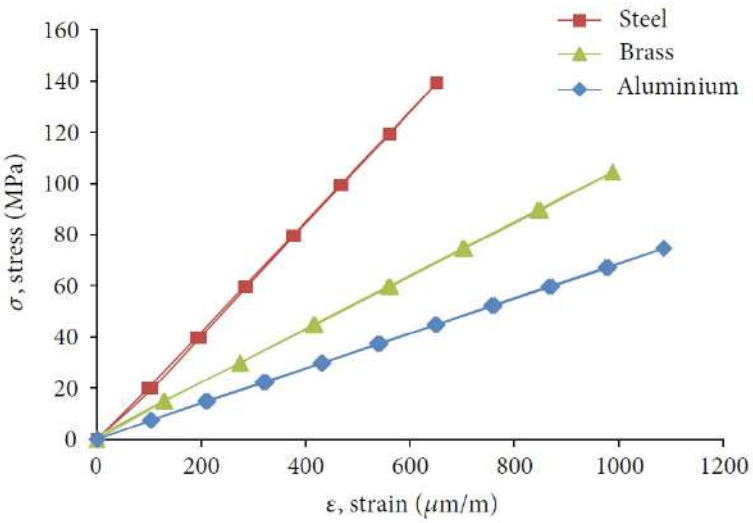

Figure 3.6. Experimental stress-strain curves obtained from tensile tests on steel, brass, and aluminium specimens using the wired method.

3.4 Results

3.4.1 Experimental results from the wired measuring method

Experimental curves obtained from separate tensile tests carried out on the brass specimen, on the aluminium specimen, and on the steel specimen, respectively, have been reported in the graph of Figure 3.6. The values of the applied stress σ have been reported on the vertical axis and measured strains ϵ in the horizontal one.

As expected, the experimental data clearly proved the elastic behavior of the specimens. According to the Hooke's law ($\sigma = E \cdot \epsilon$), the estimation of the elastic modulus E of each different material was then obtained as a slope (angular coefficient) of the linear regressions built on the experimental data. Both the ascending and descending branches of each experimental curve have been considered in these calculations. In fact, it is worth to note that a curve actually consists of a very narrow loop in which the ascending and the descending branches, respectively, do not precisely overlap each other. This fact (undesired) is usually assumed to depend from hysteretic phenomena (unavoidable) taking place during the loading/unloading cycles. In our research, the loop amplitude was made sure to remain always negligible and not to affect the test repeatability. This explains why loops are not clearly visible from curves plotted in Figure 3.6. On the other hand, linear regressions built on experimental data are found to be very accurate and characterized by R^2 values almost equal to 1. In this experimental work, the mean value of the three measurements repeated on each metal specimen has been assumed as the reference value for the elastic modulus E_{ref} of the considered material. Single experimental results and E_{ref} values have been reported in Table 3.1.

3.4.2 Experimental results from the wireless measuring method

To prove that the wireless sensor tag is a reliable measuring tool, the elastic modulus assessment previously carried out on the base of the wired method has been attempted in the wireless mode. As before, tensile loads (and stresses) continued to be measured by means of the same load cell and compensator.

Material	Stress step (MPa)	Max. Stress (MPa)	E_1 (MPa)	R_1^2	E_2 (MPa)	R_2^2	E_3 (MPa)	R_3^2	E_{ref} (MPa)
Steel	20	140	219200	0.99	223700	0.99	223100	1.00	222000
Brass	15	105							
Aluminium	7.5	75							

Table 3.1. Estimation of the reference elastic modulus E_{ref} of the materials and R^2 of the single linear regressions. Wired method.

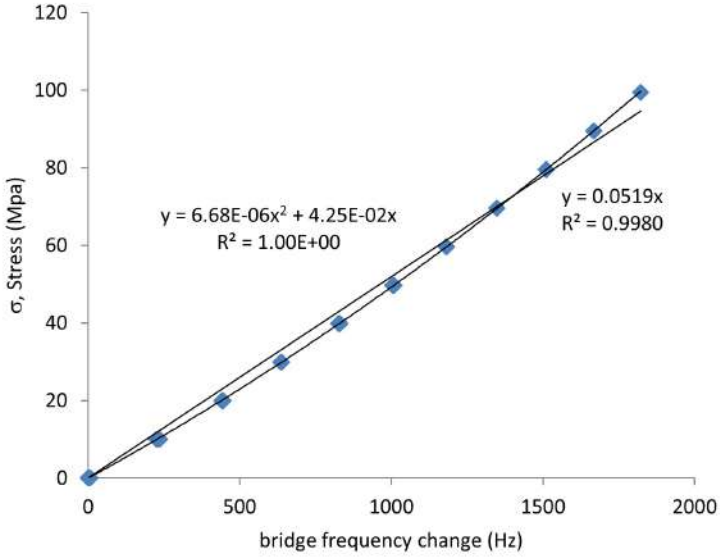

Figure 3.7. Wireless sensor tag frequency variation recorded during the tensile test on the brass specimen.

Data plotted in Figure 3.7 show the results of a tensile test performed on the brass specimen and recorded in accordance with the new wireless method. Values of the applied stress σ have been reported on the vertical axis, and the recorded bridge frequency changes on the horizontal one. To be consistent in the experimental procedure, stress increments and load sequence have been repeated as in previous tests carried out to estimate reference elastic modulus E_{ref} of the brass specimen in accordance with the wired method. Experimental data in Figure 3.7 highlight that a relationship exists among the applied load increments and the frequency changes (i.e., the modulation frequency of the back-scattered signal) measured from the interrogation unit. Actually, a linear regression built on the experimental data was found to be very satisfactory, with the coefficient R^2approaching unit ($R^2 = 0.9931$). On the other hand, considering experimental data more into details, it is noted that the experimental curve yet consists of a very narrow loop (as for wired gauge strain measurements) in which the ascending and the descending branches tend to a unique monotonic curve perfectly fitted by a second order polynomial regression ($R^2 = 1.00$) (Figure 3.7). This was confirmed also for different materials. About the weak non-linearity of the experimental curve, it is worth to note that it mainly depends on the actual value of the hardware parameters, i.e., the tolerances of the electronic components (in particular, resistances and capacitances) that make the response of the sensor tag not perfectly linear as explained in Di Giampaolo et al. (2016). Fortunately, the level of non-linearity can be made small by means of an accurate choice of the electronic components so that the resulting non-linearity can be ignored as shown by the R^2 value calculated for the linear regression plotted in Figure 3.7, approaching unit.

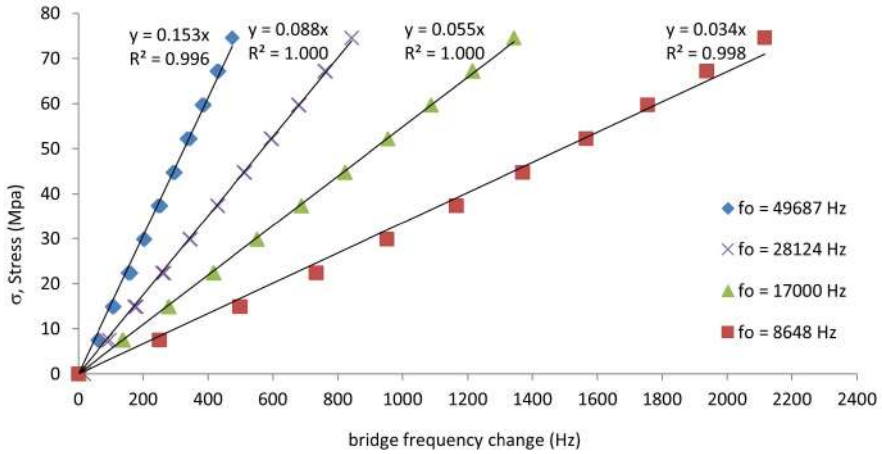

Figure 3.8. Effect of the tuning of the sensor tag. The frequency f_0 in unstressed condition depends on specific circuital parameters.

On the other hand, observing the four curves of Figure 3.8, referring to tensile tests carried out on a unique aluminium specimen, it can be noted that they significantly differ from each other for the entity of the frequency increments recorded in consequence of the same strain variation produced in the specimen. This is because the frequency response of the sensor tag changes in the four experiments; in particular, the frequency domain and the slope of the response are different. The change of the frequency response is achieved by means of different choices of the values of the electronic components of the oscillating circuit (Di Giampaolo et al., 2016). Therefore, the sensor tag can be tuned to have different frequency responses, and each response is characterized by a different reference frequency value f_0 (i.e., the frequency in unstressed condition). For these reasons, the four series of measurements shown in Figure 3.8 have been operated into different domains and have different slopes. Linear regressions plotted in Figure 3.8 are characterized from different slopes $\Delta\sigma/\Delta f$ and clearly show the highest bridge frequency changes when using the sensor tag characterized by the lowest initial frequency $f_0 = 8648$ Hz (red square dots curve). Consequently, the sensor tag characterized by higher initial frequencies results to be less and less sensitive to the same stress (strain) increments applied to the specimen.

3.4.3 Calibration

According to the wired method, a unique, direct proportion exists among the strain variations, the gauge resistance changes, and the consequent current change in the Wheatstone bridge of the compensator. Similarly, the sensor tag gives a change of the modulating frequency of the back-scattered signal in accordance with the real strain increment occurring in the gauge, but it depends on the reference frequency in unstressed condition, and it suffers from possible non-linearity. In order to investigate these characteristics of the sensor tag, a large campaign of new tensile tests has been carried out making the initial frequency f_0 variable in a wide range of values. As explained in Di Giampaolo et al. (2016), this is possible operating a suitable tuning of the electrical resistance of the circuit. Tensile tests are extended to specimens made of steel, brass, and aluminium, searching for a general validation of the proposed method. As already done in Figure 3.7, the linear regressions are calculated on the experimental data and the angular coefficient $E_{app} = \Delta\sigma/\Delta f$ of each of these regressions is regarded as an apparent

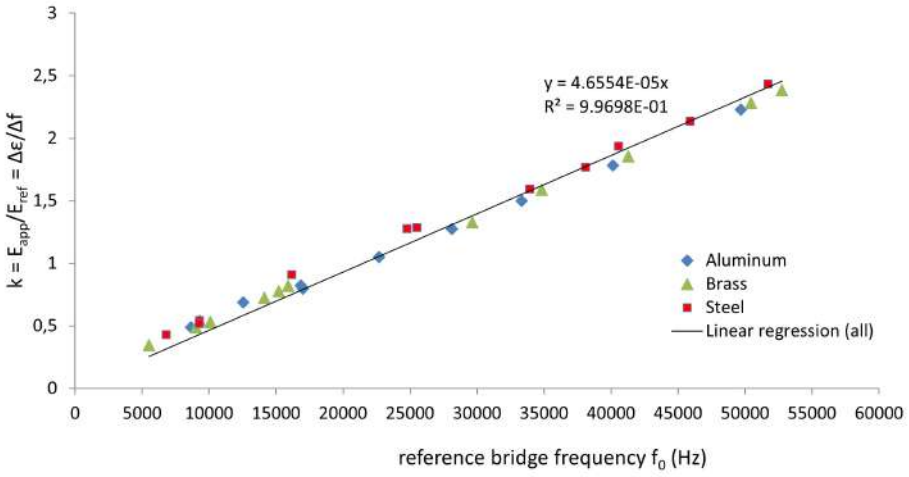

Figure 3.9. Experimental values for $k = E_{app}/E_{ref}$ as a function of the initial frequency f_0. Values of k also express the ratio among the real strain increment in the gauge ($\Delta\epsilon$) and the measured frequency variation Δf.

value of elastic modulus for the tested specimens. Results of these calculations, made with respect to a significant number of different f_0 values and extended to all the considered materials, have been reported in Figure 3.9. The ratio $k = E_{app}/E_{ref}$ among the calculated values of apparent elastic modulus E_{app} and the reference value of the Young elastic modulus E_{ref} (previously determined for various materials using the wired method) have been plotted with respect to the considered initial frequency f_0.

In particular, a unique linear relationship has been highlighted among experimental k values and f_0 ones, independently from the considered materials. That relationship can also be written as

$$k = \frac{E_{app}}{E_{ref}} = \frac{\Delta\sigma/\Delta f}{\Delta\sigma/\Delta\epsilon} = \frac{\Delta\epsilon}{\Delta f} \tag{3.2}$$

so that the variable k represents the ratio among the real strain increment to be measured ($\Delta\epsilon$) and the measured frequency change (Δf). This ratio depends on the considered frequency f_0. Then, linear regression calculated in Figure 3.9 provides the calibrating law to translate the measured frequency changes into the actual strain variation experienced by the specimen.

If nonlinearity of the experimental $\Delta\sigma$ - Δf curves is taken into account, at each step i of a single tensile test, stress increments $\Delta\sigma_i = \sigma_{i+1}$ - σ_i and, consequently, single real strain increments $\Delta\epsilon_i = \epsilon_{i+1}$-$\epsilon_i$ may be directly related to the correspondent frequency variations $\Delta f_i = f_{i+1}$ -f_i. This allows to compute several local values of the apparent elastic modulus, here named secant values $E_{sec,i} = E_{sec}(f_i) = (\sigma_{i+1}$ - $\sigma_i)/(f_{i+1}$ - $f_i)$ which depends from the actual frequency f_i at the step i. Consequently, a new definition for the ratio k (Equation (3.2)) can be given with respect to the $E_{sec,i}$ values in place of the E_{app} ones, highlighting the continued dependence of ratio $k = E_{sec}/E_{ref}$ from the current f_i value in place of the initial value f_0. In these terms, ratio k can be regarded as a continue function of the actual bridge frequency f_i in accordance with the following expression:

$$k = k(f_i) = \frac{E_{sec}(f_i)}{E_{ref}} = \frac{(\sigma_{i+1} - \sigma_i)/(f_{i+1} - f_i)}{(\sigma_{i+1} - \sigma_i)/(\epsilon_{i+1} - \epsilon_i)} = \frac{\Delta\epsilon_i}{\Delta f_i} \tag{3.3}$$

Equation (3.3) highlights the existing relation between the real strain increment to be measured $\Delta\epsilon_i$ and the frequency change Δf_i measured in place of it. The

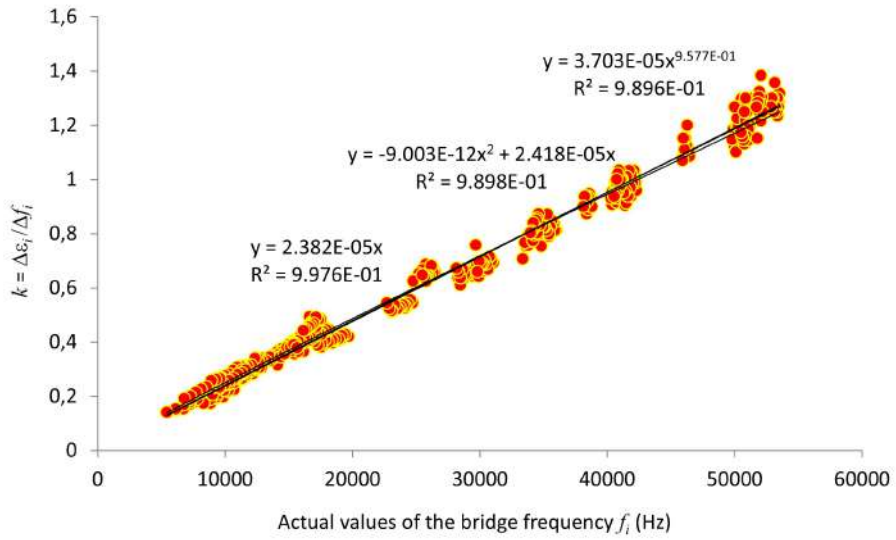

Figure 3.10. Different regressions carried out on experimental values of the ratio $k = \Delta epsilon_i \; / \; \Delta f_i$ considered as a function of the current bridge frequency f_i.

ratio k between these two variables is modelled as a continuous function of the instantaneous frequency f while strain increments (and consequent frequency changes) are taking place. A plot of $k = k(f_i)$ calculated for each tensile test is shown in Figure 3.10.

In particular, experimental $\Delta\sigma$ vs. Δf curves recorded from tensile tests were first considered as sequences of individual steps i, whose stress increments $\Delta\sigma_i$ could be converted into the real strain variations $\Delta\epsilon_i$ in accordance with Hooke's law $\Delta\epsilon_i = \Delta\sigma_i / E_{ref}$ for each specific material. Subsequently, the values of the ratio $k = \Delta\epsilon_i / \Delta f_i$ among the calculated real strain variations $\Delta\epsilon_i$ and the related frequency changes Δf_i recorded at the step i have been computed and plotted with respect to the instantaneous bridge frequency value f_i considered at the beginning of each considered step i.

Data in Figure 3.10 refer to the entire bunch of experimental values obtained from tensile tests performed on all the three different couples of metal specimen. These data clearly show the real strain increment and the correspondent frequency change to be strictly related to each other. In particular, several regression laws have been calculated on the experimental data, including an exponential form, a second order polynomial, and a linear equation, respectively. The first two regression laws showed to fit experimental data not significantly better than the linear regression one, this latter being characterized from an R^2 value very close to unity. Assuming $k = k(f_i)$ as a continue function of f_i, the differential $k = \Delta\epsilon / \Delta f$ can be considered and the real strain variation $\Delta\epsilon$ is calculated in accordance with the following integral expression:

$$\Delta\epsilon = \int k(f) df \tag{3.4}$$

If the linear regression law $k = 2.382\text{E-}05 \cdot f$ (indicated in Figure 3.10) is substituted in Equation (3.4), the strain increment $\Delta\epsilon$ occurring in the gauge while the measured frequency changes from value f_1 to value f_2 is simply calculated as

$$\Delta\epsilon = 1.1912 \cdot 10^{-5} (f_2^2 - f_1^2) \tag{3.5}$$

Once again, it is worth noticing that Equation (3.5) is independent from the

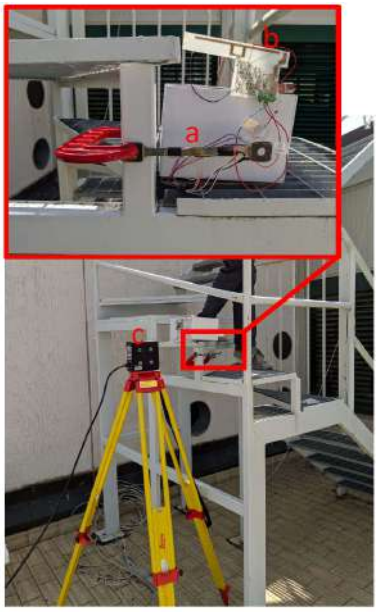

Figure 3.11. Dynamic measurement set-up: (a) instrumented cantilever anchored at one end to the structure of a steel staircase; (b) wireless sensor tag; (c) laser detector.

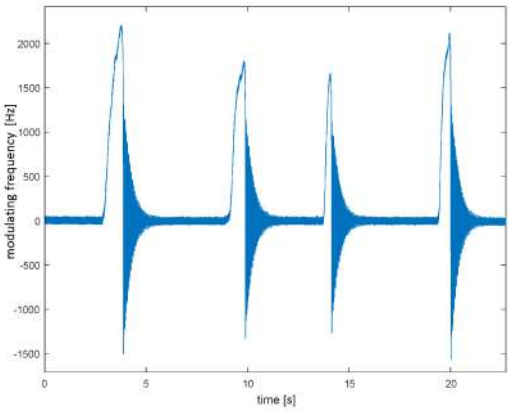

Figure 3.12. Response of the oscillating cantilever under repeated pulse loading. The enlargement of free vibration is shown in Figure 3.13.

material of the specimen. Also, the validity of Equation (3.5) extends to a very wide range of frequency values (from just a few Hz up to 60 kHz). On the other hand, measurements performed with a sensor tag having lower initial frequency result to be more sensitive than that having higher initial frequency. In fact, in the former case, the ratio $k = \Delta\epsilon/\Delta f$ is less than unity. In this condition, the frequency variation of 1 Hz corresponds to a strain variation lower than 1 ϵ, representing a great improvement with respect to strain measurements performed with traditional techniques. In fact, electrical current variations in gauges are generally detected with such a limited resolution that only a precision of several ϵ may correspond, this representing a limit for the traditional method of measuring strains with wired gauges. In comparison, the proposed new method may enhance the strain measurement resolution even below 0.2 ϵ if the initial frequency is set lower than about 10 kHz.

3.4.4 Experimental results from the wireless measuring method: Dynamic measurements

A steel cantilever about 25 cm long has been anchored at one end to the structure of a steel staircase as shown in Figure 3.11 so that it can vibrate after an initial displacement of its free end. The cantilever is instrumented with the proposed

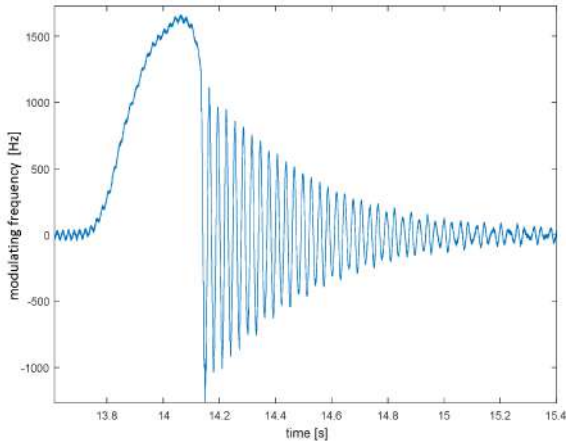

Figure 3.13. Enlargement of the third response of Figure 3.12. It shows the loading and free vibration of cantilever.

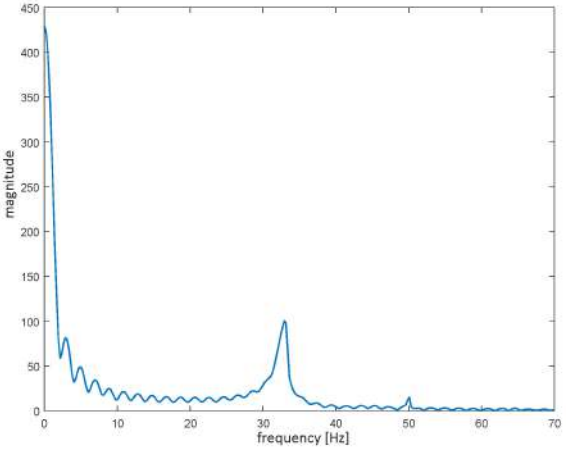

Figure 3.14. Spectrum of the signal of Figure 3.13: the continuous component (frequency zero) depends on the part of the signal corresponding to the static condition of the cantilever, the peak at 33.14 Hz is the natural frequency of vibration of cantilever, and the small peak at 50 Hz is the hardware noise (supplying network of the central unit).

sensor that changes the modulation frequency of the back-scattered signal dynamically according to the vibration movement. In fact, the strain gauge alternates extension and compression in agreement with the natural frequency of the beam, while the back-scattered signal changes its modulating frequency according to the extension and compression of the strain gauge. The analog modulated signal coming back from the sensor is received, sampled, and recorded by a Universal Software Radio Peripheral (National Instruments NI USRP 2920). A subsequent demodulation and filtering permit to determine the vibration frequency and the damping of the vibration.

Figure 3.12 shows the modulation frequency of the received signal with respect to time in the case of repeated bending (with a pulse load) of the free end of the cantilever with a time interval of about 5 seconds. After each bending, the load is quickly removed permitting the cantilever to have free vibration. Figure 3.12 shows four responses of the cantilever under repeated loading and free vibration.

Figure 3.13 shows an enlargement of the third response. Until about 13.8 s the cantilever is static, the small ripple concerns hardware and numerical noise. From 13.8 s until about 14.1 s, the modulation frequency increases because of the progressive loading of the free end of the cantilever. After 14.1 s, the load is quickly removed and the cantilever is under free vibration; the modulation frequency becomes oscillating since it follows the alternating extension and compression of the strain gauge glued on the cantilever. The frequency of that oscillation corresponds to the natural frequency of the cantilever as shown in Figure 3.14 that is the spectrum of the signal of Figure 3.13. The continuous component in

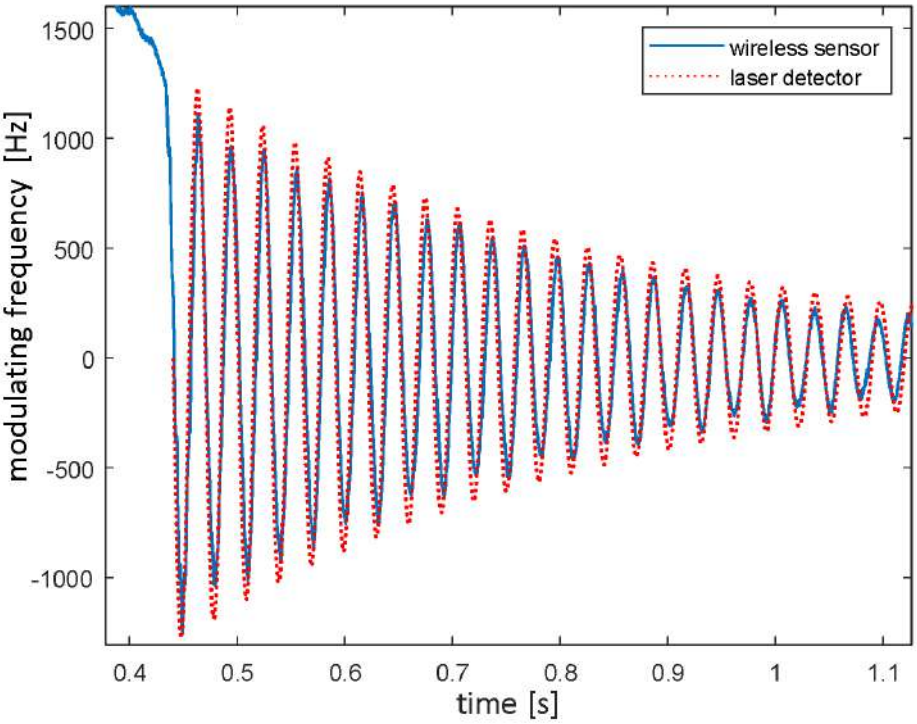

Figure 3.15. Comparison between the response of the wireless sensor and measurement with a laser detector (after a suitable scaling and translation).

Figure 3.14 depends on the part of the signal corresponding to the static condition of the cantilever, the peak at 33.14 Hz is the natural frequency of vibration of the cantilever, and the small peak at 50 Hz is the hardware noise (from supplying network). Because of the damping of vibration, the oscillation of Figure 3.13 (i.e., the modulation frequency) decreases along the time. The response of the sensor has been compared to that measured by a laser detector (also shown in Figure 3.12) obtaining excellent agreement (shown in Figure 3.15).

3.5 Conclusions

A new method for measuring strains has been proposed. It consists in a wireless technique based on a traditional strain gauge integrated into an electrical circuit together with an RFID tag. While traditionally strain measurement is usually performed by reading the current variation occurring in the circuit as a consequence of the resistance change in the strain gauge, in the proposed new method, an interrogating antenna is used to detect the modulation frequency of an electromagnetic signal that varies in accordance with the strain to be measured. Several tensile tests have been carried out on metal specimens made of different materials, including steel, brass, and aluminium. Feasibility of this new method has been proved determining a unique clear relationship among the strain values and the measured frequency changes. The tag sensor is able to measure dynamic phenomena as assessed by experiments with vibrations of tens of Hz. The detectable frequency of vibration is not limited by the sampling rate because the sampling is performed in the central unit (not in the tag sensor) that can be equipped with a suitable sampling device. The limit in measuring oscillating phenomena is given by the bandwidth of the strain gauge that is in the order of KHz, while the bandwidth of electronic components is much larger in the order of MHz. So, the tag sensor

should be able to measure oscillations up to a few kHz. A calibration of the measuring system has been proposed, showing that it remains valid for a large range of working frequencies and for large strain intervals as well. In comparison with a traditional strain measuring procedure, the accuracy of the proposed new technique has been proved to be potentially higher. Effectiveness of the proposed wireless method has been proved up to a maximum interrogating distance of 20 meters in a laboratory room and outdoor, making this new strain measuring technique suitable for structural monitoring.

Use of commercial RFID tags for civil engineering purposes: displacement monitoring

4.1 Introduction

Structural Health Monitoring (SHM) is going on resorting to intelligent monitoring systems to study the characteristics and the evolution of damaged infrastructures or the behaviour of the structures for loading and fatigue effects as well as material aging. In particular, new wireless methodologies are increasingly used and developed, since the use of wireless sensor networks (WSNs) permit a fast and easy installation even in measurement points difficult to access and allow to spread over the structure a large number of sensors, to obtain a distributed assessment of the structural condition, with low costs of the devices and low maintenance costs. In this Chapter, the use of pure commercial RFID tags (not being embedded in antennas) has been investigated to be employed for civil engineering purposes, specifically for the monitoring of out-of-plane displacements of brick walls in a passive manner (without the consumption of energy power).

4.2 Background: commercial UHF-RFID tags

The RFID technology is used commercially for the identification and/or automatic storage of data relating to objects or animals. It is based on the storage capacity of certain electronic labels, called Tags (or transponders), of information regarding the object to which it is coupled. These tags respond to remote interrogation by devices called readers. Over the years, the RFID technology has developed and has been used in many sectors: industrial, automotive, medical, e-Government (see passports, identity cards, etc.), transport and other uses. Given its versatility, it is considered a general purpose technology. Through the use of RFID technology it is possible to create a system of interconnected objects that allow the collection and processing of data in a single large global network.

Specifically, an RFID system consists of four fundamental elements:

1. The Tag is a small device which consists of an integrated circuit (IC) with

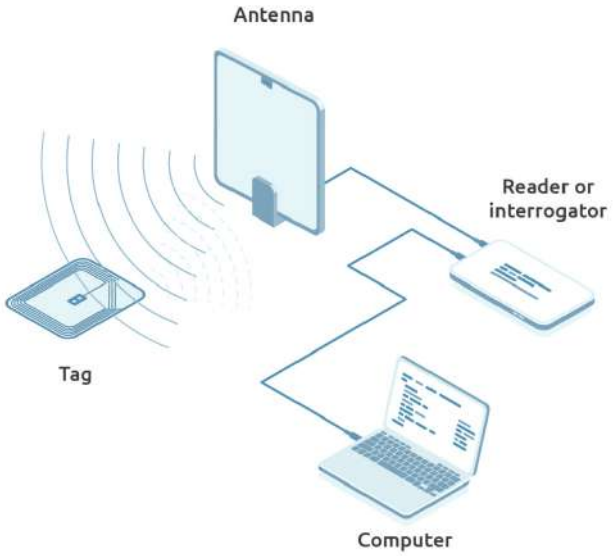

Figure 4.1. Example of a RFID reading system and its components: Tag, Antenna, Reader, Computer

simple control logic functions, with memory, incorporated into a paper or plastic label. Once activated by the other elements of the system through an electric or magnetic field, the Tag is able to transmit the information it contains. Such information can be not only read, but also modified through write operations. Generally, the data contained in the tag memory has a unique identification code.

2. The antenna allows to send and receive the data contained within the tag through electromagnetic waves. These waves are collected by the antenna contained in the RFID tag and used to power the microchip which releases information to be returned to the reader.

3. The Reader is the element of the system that has the task of reading and filtering the information on the Tags. The Antenna and readers can be combined in a single device or be two distinct devices.

4. The management system (host computer, server) is the information system that is connected to the network and to the reader. This system allows, starting from the identification codes coming from the tags, to obtain all the available information associated with the objects and to manage this information for the purposes of the use case.

In figure 4.1 is represented a RFID system with its components.

Tags can vary in shape, size, material and operating frequency but all of these can be grouped into three large families: Active, Passive and Semi-Passive or Semi-Active.

In this study, passive tags have been used. Passive tags do not have their own energy source but receive it from the signal coming from the Antenna.

In particular, passive UHF-RFID tags have been used. In the far-field region, the interaction of the components is dominated by the electromagnetic field created by the antenna. The RFID tag resonates with the frequency of the electromagnetic field and the current generated activates the chip. Tags of this type are part of

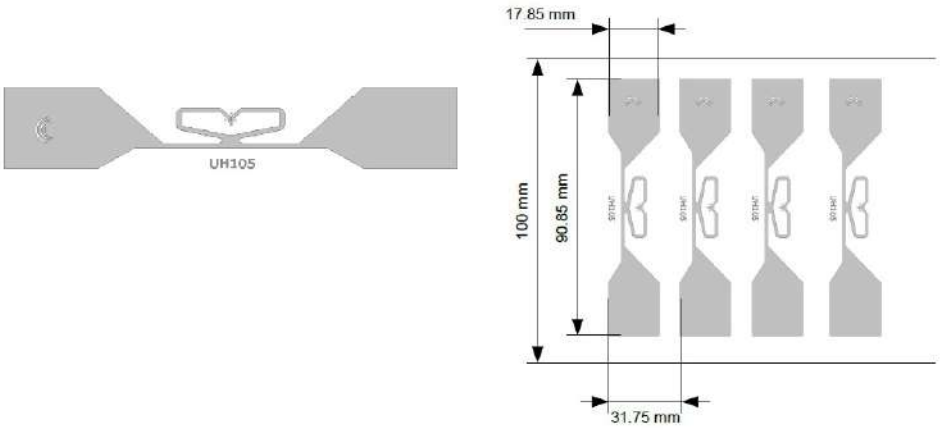

Figure 4.2. Detail of the commercial UHF-RFID tag: UH105

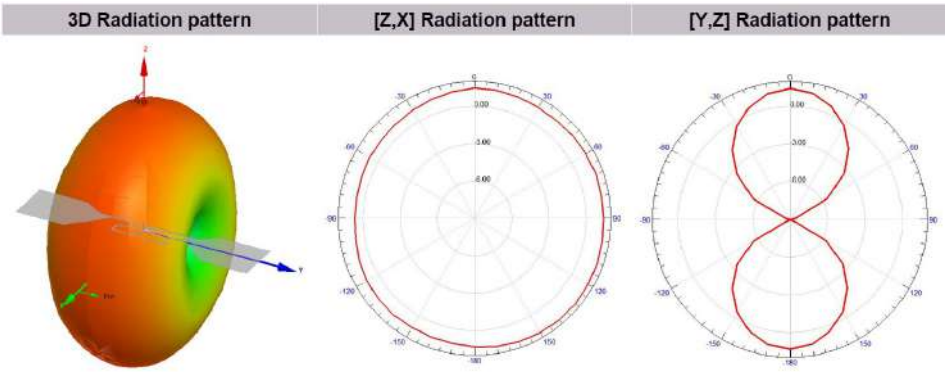

Figure 4.3. Radiation pattern of the UH105 tag

the UHF class which operates at 867/868 MHz. The distances in which they can operate are of few meters, up to 30 meters.

More specifically, the commercial UH105 tags have been used (figure 4.2). UH105 tag is a completely passive transponder made by LAB-ID. Its dimensions are $90.85 \times 17.85\ mm^2$ and consists of an aluminium dipole antenna (9 μm thick) and a polyester (PET) substrate with a thickness of 38 μm. An EPC Class 1 Gen2 Impinji Monza 5 chip, operating in the 840 MHz – 960 MHz band, is connected to the antenna. This tag has been designed to be used in logistics and in fields where there is a high concentration of tags. This is possible thanks to its good radiative properties, and to its good properties of insensitivity to its orientation in the space in which it is positioned, that allow it to be detected at a great distance.

The main features of this commercial tag are reported in Table 4.1 and figure 4.3.

Composition	Material	Thickness [μm]
Top	Aluminium	9 ± 5%
Support	Polyester PET	38 ± 5%
Tag	Operating frequency	Operating temperature
	840 - 960 MHz	-40 °C to +85 °C

Table 4.1. Features of the commercial UHF-RFID tag.

4.3 Application of the UHF-RFID tags for civil engineering purposes: experimental investigation

In this study the UHF-RFID tags (UH105) were used to monitor the displacements of two brick walls 2.70 m high and 1 m wide, subjected to out-of-plane actions induced by a concentrated load along the middle of each wall. The innovation of this research is represented by the application of this type of sensors in civil engineering.

Since no literature is reported about this type of application of RFID tags for civil engineering monitoring purposes, experimental tests were first conducted in the laboratory room in a controlled environment to investigate the feasibility of the application, and then performed on site.

4.3.1 Monitoring displacements under out-of-plane actions: laboratory experiments

Two experimental campaigns were carried out in the laboratory to assess the feasibility of using RFID tags for the monitoring of out-of-plane displacements.

The experimental set-up of each campaign was organised considering the in situ distances and spaces, in order to make then a comparison between the results in the same conditions, except for the environment. It is known, in fact, that the RFID tags and the antenna are sensitive to the presence of metal in the environment, since they work with electromagnetic waves. Each tag reflects part of the electromagnetic power received, which is detected by the Reader antenna. The phenomenon of reflection of the electromagnetic waves is known as "back-scattering" and is similar to that on which the operation of radar systems is based. The presence of metal or other obstacles around the electromagnetic field can alter or shield the signal, modifying the expected results. For this reason, the experiments were carried out first in the laboratory room where the presence of metal was very low and no environmental obstacle was present.

The first campaign considered six tags positioned following a 3x2 grid. A ID number identified each tag, so they could be named as follows: Tag 1.4, Tag 2.1, Tag 1.3, Tag 1.1, Tag 1.5, Tag 2.2.

The tag were positioned on a polystyrene panel, which acts like a "transparent" panel to the electromagnetic waves and does not modify the back-scattered signal. The tags were positioned as depicted in Figure 4.4. The Antenna was positioned in front of the panel, at a distance of 60 cm. The projection of the center of the antenna on the panel falls at a distance of 3 cm below the central axis of the tags of the central row (in red in Figure 4.4). The panel was subjected to rigid out-of-plane displacements, orthogonal to the plane of the panel and the antenna by the use of a micrometric screw. In particular, the panel was moved towards the antenna at steps of 5 mm, reaching the final distance of 60 mm respect to the starting position. The Antenna works at 867 MHz and the acquisition system was set with a power of 20 dBm which was sufficient for a correct reading of each tag.

A second laboratory experimental campaign was performed, with a similar set-up. The tags chosen for the 2nd experimental campaign were: Tag 2.4, Tag 2.2, Tag 2.1, Tag 1.4, Tag 2.3, Tag 1.2.

Only few tags have been chosen for both experimental campaigns, this in order

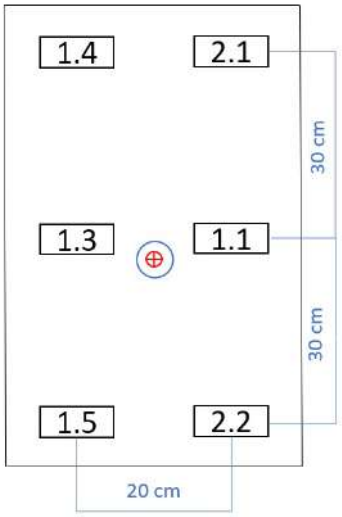

Figure 4.4. 1st laboratory campaign: scheme of the experimental set-up. In red, the projection of the center of the antenna on the polystyrene panel.

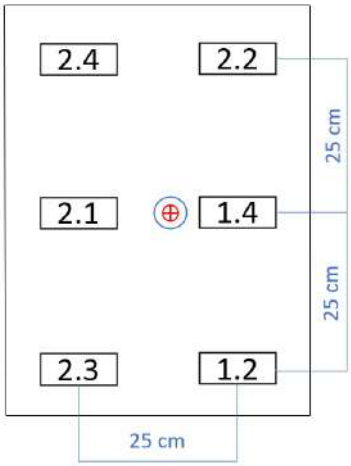

Figure 4.5. 2nd laboratory campaign: scheme of the experimental set-up. In red, the projection of the center of the antenna on the polystyrene panel.

not to overlook any anomalies related to the specific characteristics of a given tag.

The tag were positioned on a polystyrene panel, as represented in Figure 4.5. The Antenna was positioned in front of the panel, at a distance of 62 cm. The projection of the center of the antenna on the panel (in red in Figure 4.5) falls on the central axis of the tags of the central row, specifically at 15 cm from the center of Tag 2.1 and 10 cm from the center of Tag 1.4. The panel was subjected to the same out-of-plane displacements of the 1st campaign, orthogonal to the panel and the antenna, with steps of 5 mm, by the use of a micrometric screw, reaching the final distance of 70 mm respect to the starting position. In this case the acquisition system was set with a power of 24 dBm which was sufficient for a correct reading of each tag. The set-up is shown in figure 4.6.

4.3.2 Results of the laboratory experimental campaigns

In both experimental campaigns, the acquisition of displacement measurement was performed for each step (each 5 mm). In the following figures, for each tag the results of the measurements are reported plotting the mean and standard deviation values of the phase, referring to each step of measurement. Also the Received Signal Strength Indicator (RSSI) is plotted, indicating a good quality of the signal for values around -52 dBm.

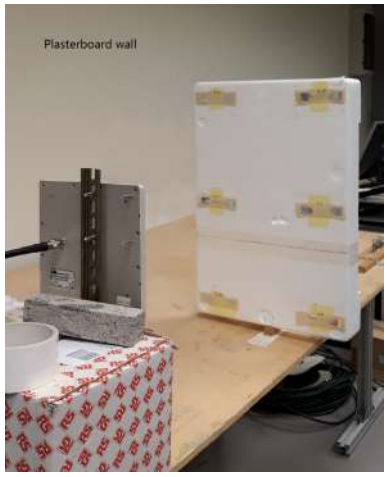

Figure 4.6. 2nd laboratory campaign: experimental set-up.

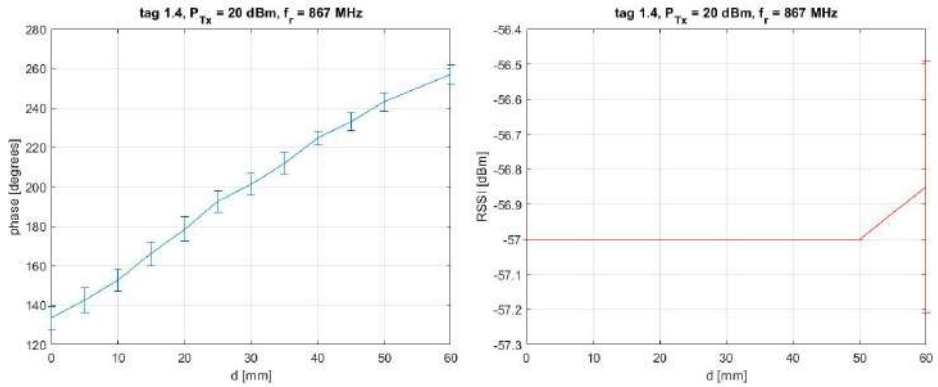

Figure 4.7. 1st laboratory campaign: Tag 1.4. Mean and standard deviation values of the phase and relative RSSI values registered for each step of measurement.

4.3.2.1 Results of the 1st laboratory campaign

In Figure 4.7, Figure 4.8, Figure 4.9, Figure 4.10, Figure 4.11, Figure 4.12 are reported the results of the acquisition systems of the Tag 1.4, Tag 2.1, Tag 1.3, Tag 1.1, Tag 1.5, Tag 2.2 respectively. The mean and standard deviation values of the phase registered for each step of measurement are reported for each Tag together with the relative RSSI values.

As can be observed from the graphs of Figures from 4.7 to 4.12, a difference in the phase values is detected from the starting point 0 mm to the final point 60 mm, in particular linear increasing values of the phase are observed for each step of measurement. This means that the Tags are sensitive to the displacements that have been imposed to them in each step of measurement. The RSSI values are quite constant for Tags 1.4, 1.5, 2.2, and with very small fluctuations for the other

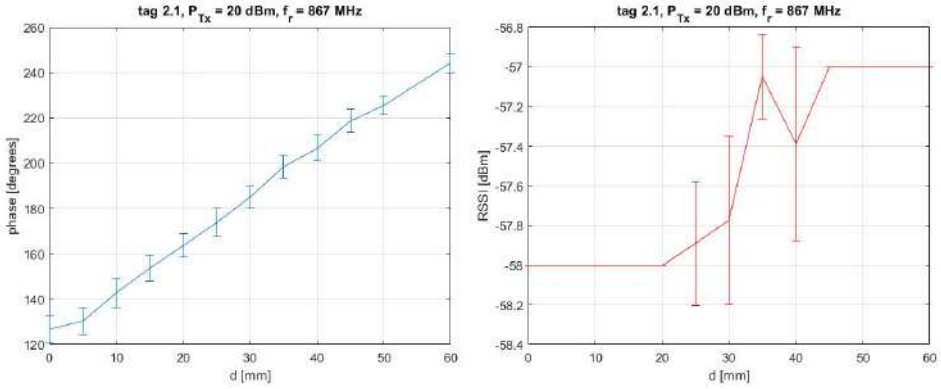

Figure 4.8. 1st laboratory campaign: Tag 2.1. Mean and standard deviation values of the phase and relative RSSI values.

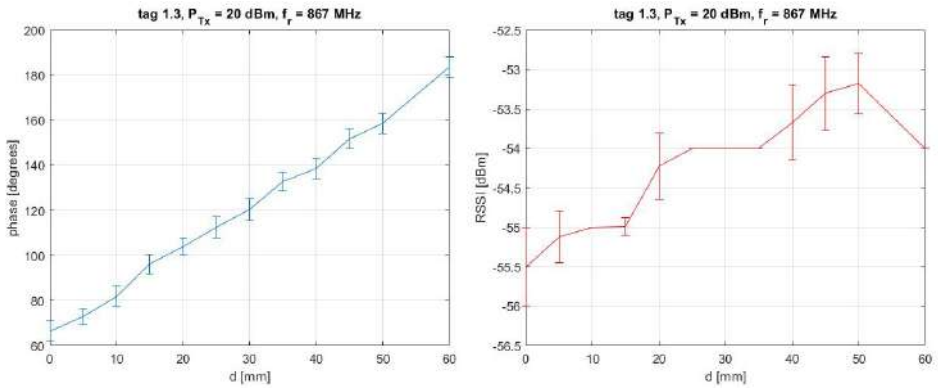

Figure 4.9. 1st laboratory campaign: Tag 1.3. Mean and standard deviation values of the phase and relative RSSI values registered for each step of measurement.

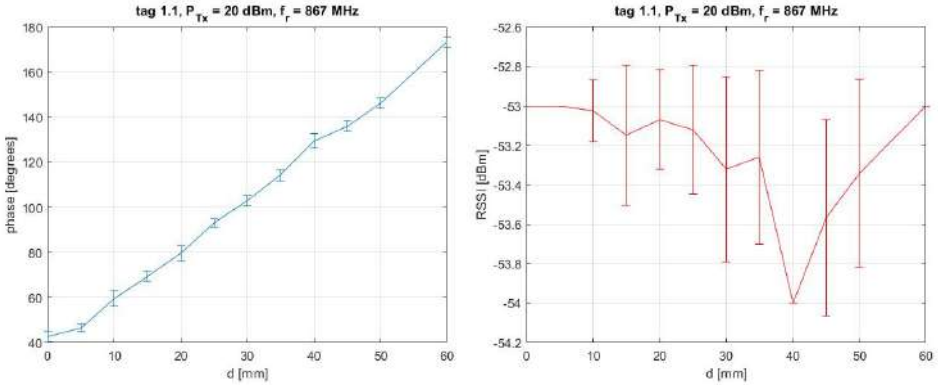

Figure 4.10. 1st laboratory campaign: Tag 1.1. Mean and standard deviation values of the phase and relative RSSI values registered for each step of measurement.

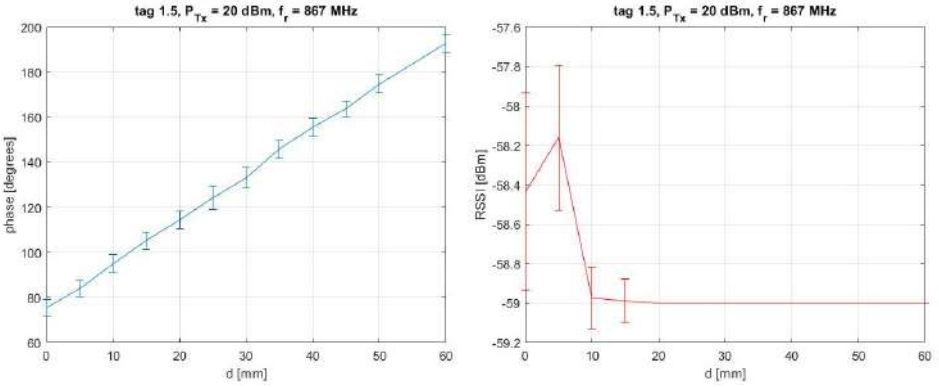

Figure 4.11. 1st laboratory campaign: Tag 1.5. Mean and standard deviation values of the phase and relative RSSI values registered for each step of measurement.

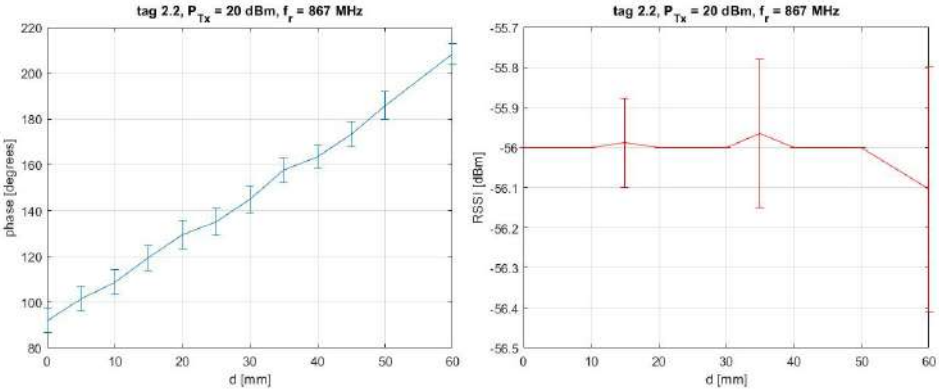

Figure 4.12. 1st laboratory campaign: Tag 2.2. Mean and standard deviation values of the phase and relative RSSI values registered for each step of measurement.

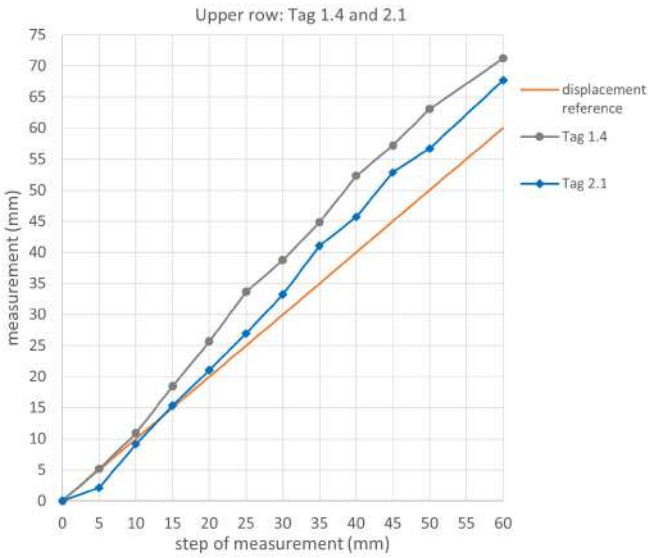

Figure 4.13. 1st laboratory campaign: Upper row Tag 1.4 and 2.1. Displacements detected by the Tags compared to the actual displacements imposed to the panel.

tags, anyway acceptable.

To assess the feasibility of this new wireless monitoring application, the phase difference between a certain step of measurement and the previous one has been converted into distance difference by using the following equation:

$$d - d_0 = \frac{(f - f_0) \cdot \lambda}{4 \cdot 180} \tag{4.1}$$

where $f - f_0$ is the phase difference associated to a certain step of measurement and the previous one, λ represents the wavelength that in this case is equal to 0,346 m.

From this formula, it is determined the distance difference $d - d_0$ that occurs along the three-dimensional path of the electromagnetic waves when the Tag moves from a certain position to another. So it's the spatial difference between the paths linking the center of the antenna and the Tag when the Tag moves.

To determine the distance difference and so the displacement of the tag in the out-of-plane direction (orthogonal to the polystyrene panel on which the Tags are positioned), it has been necessary to geometrically calculate it by a 3D modelling of the set-up.

The results of displacements detected by the Tags have been plotted in graphs, compared to the actual displacements imposed (plotted as displacement reference) in order to assess the feasibility of the technique.

For a faster comprehension, the displacement results have been coupled according to the Tags position in rows (see figure 4.4), distinguishing in upper row, central row and lower row Tags.

In the graph of figure 4.13 are reported the displacements detected by Tag 1.4 and 2.1 compared to the actual displacements imposed to the panel. Figure 4.14 reports the displacements detected by central row Tags 1.3 and 1.1 and Figure 4.15 shows the displacements of the lower row Tags 1.5 and 2.2.

As can be seen from the graphs, the Tags all show quite matching displacements. This is surprising, considering the intrinsic measurement errors of the reader itself and the standard deviations of the mean values calculated for the phases measurements.

More in depth, we can also observe that for the upper row Tags there is the

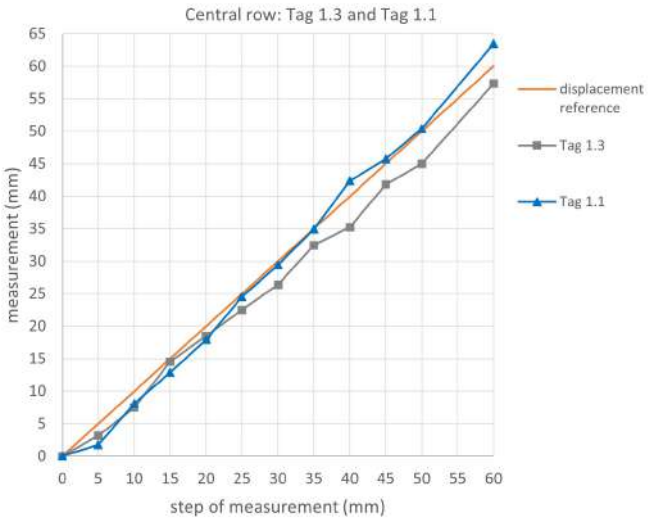

Figure 4.14. 1st laboratory campaign: Central row Tag 1.3 and 1.1. Displacements detected by the Tags compared to the actual displacements imposed to the panel.

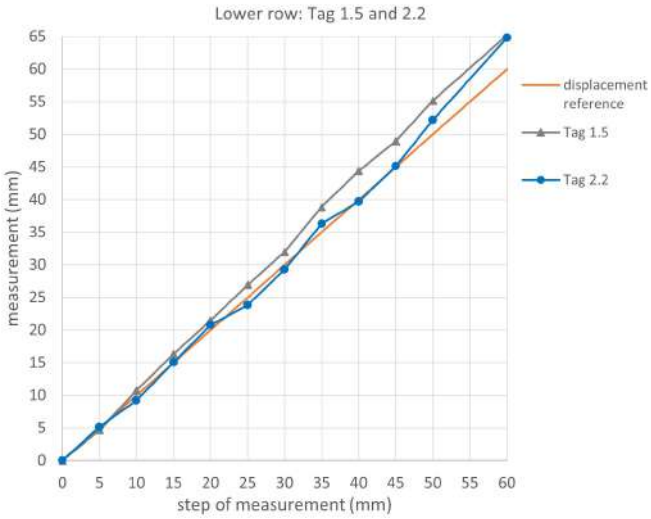

Figure 4.15. 1st laboratory campaign: Lower row Tag 1.5 and 2.2. Displacements detected by the Tags compared to the actual displacements imposed to the panel.

higher error, in particular for Tag 1.4.

It can be supposed that this higher error is due to the position of the antenna that is more distant from these Tags, compared to central and lower row Tags (see Figure 4.4). The discrepancies in the results could be checked into the environment. Observing the environment of the laboratory, depicted in figure **??**, it can be noted that Tag 1.4 is near a plasterboard wall. It can be supposed that the metallic components of the plasterboard wall could have influenced some way the signal, reducing the response of the Tag. Also Tags 1.3 and 1.5 are at the same distance from the plasterboard wall, but their response is better since the antenna is nearer.

4.3.2.2 Results of the 2nd laboratory campaign

In this second campaign, the same Tags 2.1, 1.4, and 2.2 have been used together with new Tags 2.4, 2.3, and 1.2.

In Figure 4.16, Figure 4.17, Figure 4.18, Figure 4.19, Figure 4.20, Figure 4.21 are reported the results of the acquisition systems of the Tag 2.4, Tag 2.2, Tag 2.1, Tag 1.4, Tag 2.3, Tag 1.2 respectively. The mean and standard deviation values of the phase registered for each step of measurement are reported for each Tag together with the relative RSSI values.

As can be observed from the graphs of Figures from 4.16 to 4.21, also in this case

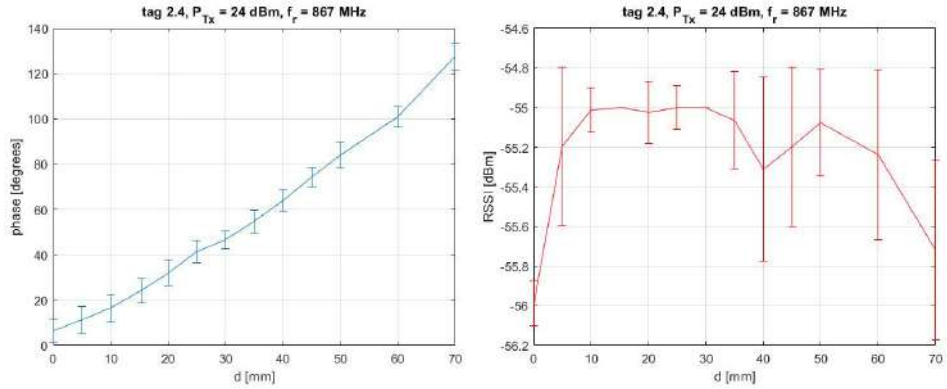

Figure 4.16. 2nd laboratory campaign: Tag 2.4. Mean and standard deviation values of the phase and relative RSSI values registered for each step of measurement.

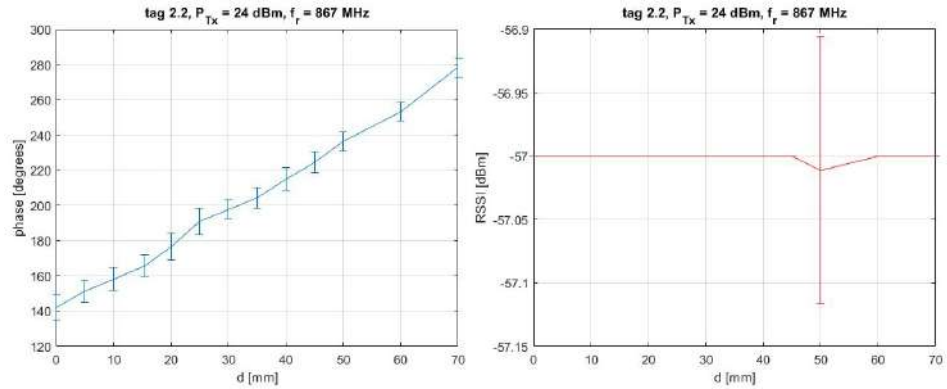

Figure 4.17. 2nd laboratory campaign: Tag 2.2. Mean and standard deviation values of the phase and relative RSSI values registered for each step of measurement.

linearly increasing values of the phase are detected for each step of measurement, from the starting point 0 mm to the final point 70 mm. The RSSI values are acceptable. They are costant for Tags 2.1 and 2.2, and with small fluctuations for the other tags.

The phase difference has been converted into distance difference by using Equation (4.1)

To determine the distance differences and so the displacements of the Tags in the out-of-plane direction, it has been necessary to geometrically calculate them by a 3D modelling of the set-up.

The results of displacements detected by the Tags have been plotted, compared to the actual displacements imposed (plotted as displacement reference) in order to assess the feasibility of the technique.

The displacements results have been coupled according to the Tags position in rows (see figure 4.5), distinguishing in upper row, central row and lower row Tags.

In the graph of figure 4.22 are reported the displacements detected by Tag 2.4

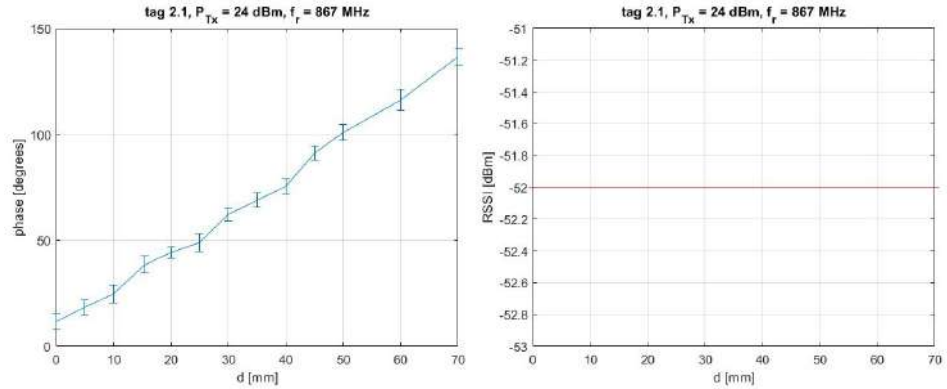

Figure 4.18. 2nd laboratory campaign: Tag 2.1. Mean and standard deviation values of the phase and relative RSSI values.

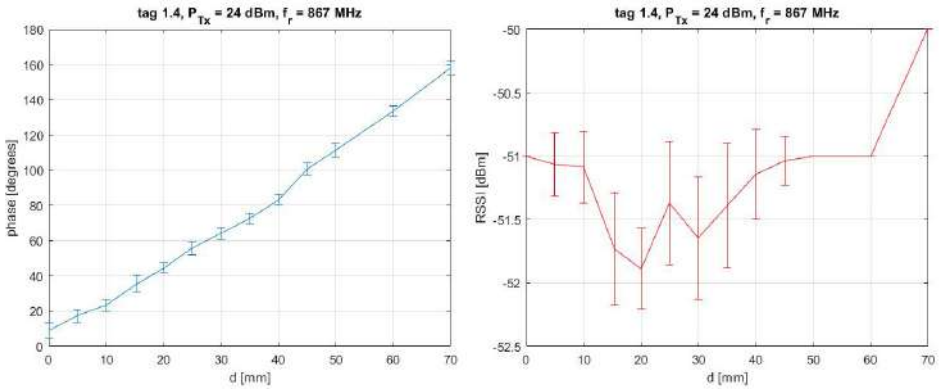

Figure 4.19. 2nd laboratory campaign: Tag 1.4. Mean and standard deviation values of the phase and relative RSSI values registered for each step of measurement.

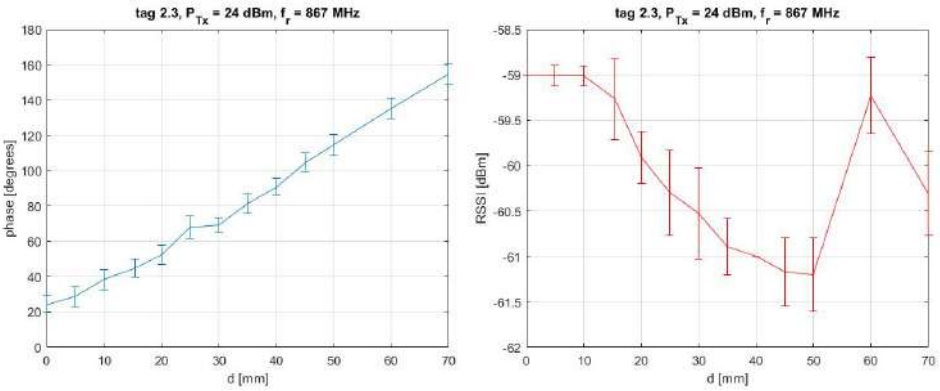

Figure 4.20. 2nd laboratory campaign: Tag 2.3. Mean and standard deviation values of the phase and relative RSSI values registered for each step of measurement.

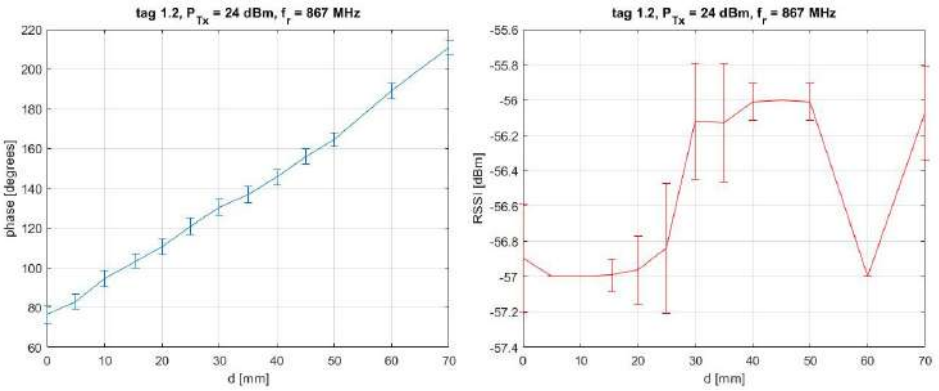

Figure 4.21. 2nd laboratory campaign: Tag 1.2. Mean and standard deviation values of the phase and relative RSSI values registered for each step of measurement.

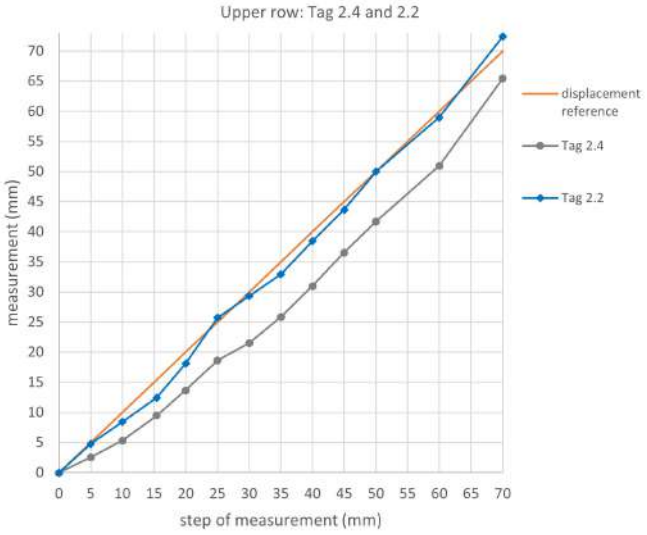

Figure 4.22. 2nd laboratory campaign: Upper row Tag 2.4 and 2.2. Displacements detected by the Tags compared to the actual displacements imposed to the panel.

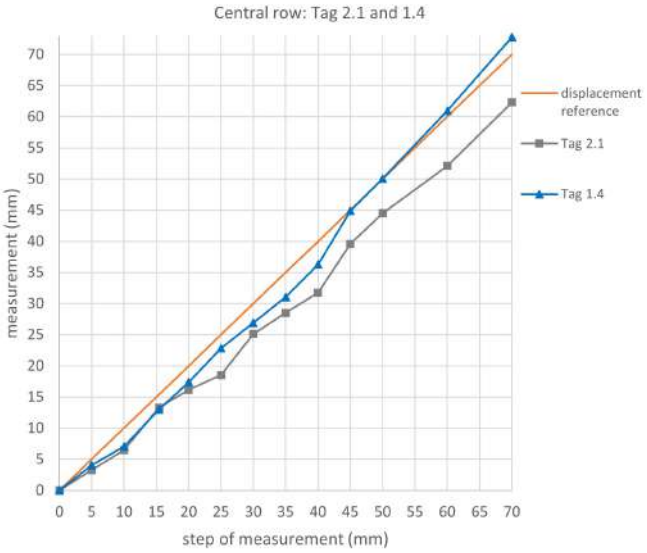

Figure 4.23. 2nd laboratory campaign: Central row Tag 2.1 and 1.4. Displacements detected by the Tags compared to the actual displacements imposed to the panel.

and 2.2 compared to the actual displacemets imposed to the panel. In Figure 4.23 are reported the displacements detected by Tag 2.1 and 1.4 and in Figure 4.24 are shown the displacements of Tag 2.3 and 1.2.

As can be seen from the graphs, also in this case the Tags all show quite matching displacements.

More in depth, we can observe that the Tags that are positioned to the right (Tag 2.2, Tag 1.4, and Tag1.2) detected the displacements almost perfectly.

The Tags positioned to the left are those who presents higher errors, except for Tag 1.2.

It can be supposed that the reduced response of these Tags is due to the position of the antenna that is more distant from these Tags, together with the influence of the plasterboard wall.

4.3.2.3 Short conclusions on the laboratory experimental campaigns

Overall, it can be observed that:

- the displacements detected by the tags match almost perfectly with those actually imposed;

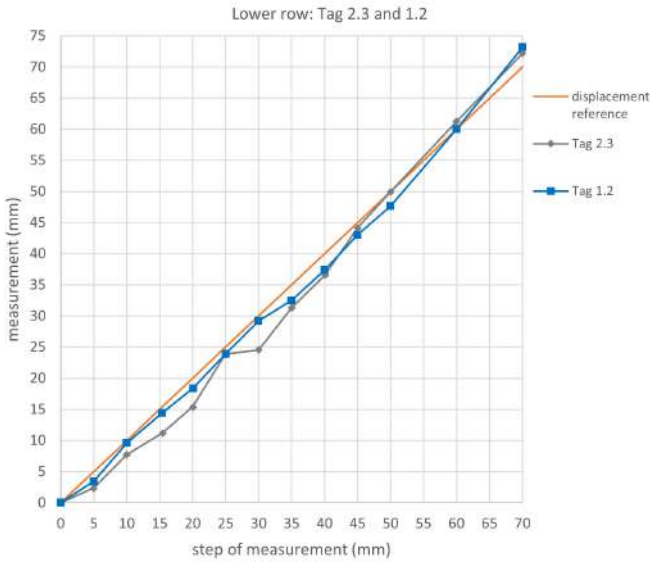

Figure 4.24. 2nd laboratory campaign: Lower row Tag 2.3 and 1.2. Displacements detected by the Tags compared to the actual displacements imposed to the panel.

- a weaker response of some Tags is assumed to be attributed to environmental interference together with the position of the tags with respect to the antenna;
- it should also be considered the intrinsic measurement errors of the reader itself and the errors in processing the received data (standard deviations of the calculated mean values of the phases).

For example, if we consider the Tag 1.4 which has been used in both the experimental campaigns, in the 1st campaign the response of the Tag is not so good because it is positioned at a greater distance from the center of the antenna (upper row) and is near the plasterboard wall (left side). In the 2nd campaign, instead, the same Tag is positioned in the central row (nearer the antenna) and on the right side (more distant from the plasterboard wall) and the response of the Tag is very satisfactory.

The response of the Tags in laboratory environment demonstrated to be very satisfactory, proving that the new application of wireless RFID tags for the monitoring of out-of-plane displacements is feasible.

Considering these results, two experimental campaigns have been performed also in situ and are described in the next section.

4.3.3 Monitoring walls displacements under out-of-plane actions: in situ experiments

The UHF-RFID tags were used to monitor the displacements of two brick walls 2.70 m high and 1 m wide, subjected to ou-of-plane actions induced by a concentrated load along the middle of each wall. The brick walls were realised and tested in situ, in a building site. Fixed constraint is placed along the entire base of each wall and hinge constraint is applied at the top of each wall which is anchored to the metal frame.

For the first wall, the tags were positioned following the 3x2 grid with the same set up distances of the 1st laboratory campaign, in order to make a comparison with the same geometric conditions. The antenna was positioned at a height of 1.27 m. The distance between the center of the antenna and the wall was 0.60 m.

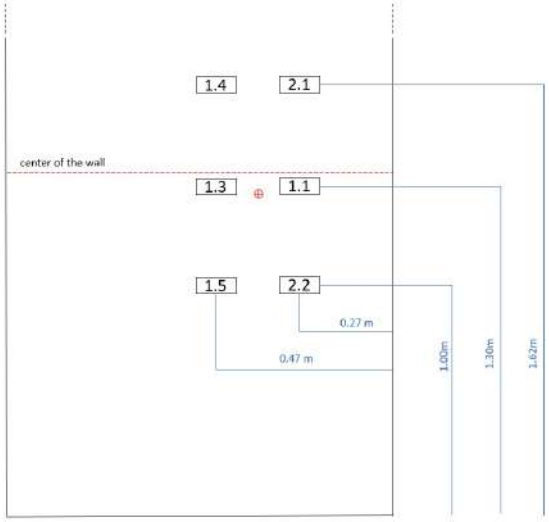

Figure 4.25. Scheme of the experimental set-up of the first wall.

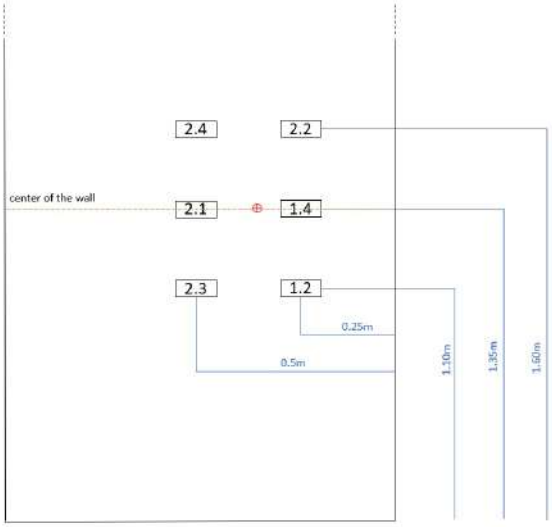

Figure 4.26. Scheme of the experimental set-up of the second wall.

The wireless acquisition of data was made with a power of 20 dBm. The set-up is schematized in figure 4.25.

For the second wall, the same tags of the 2nd laboratory test were used. The tags were positioned following the 3x2 grid with the same set up distances. The distance between the center of the antenna and the wall was 0.62 m. The height of the antenna was 1,35 The wireless acquisition of data was made with a power of 24 dBm. The set-up is schematized in figure 4.26.

To avoid any electromagnetic influence on the response of the tags, due to the material characteristics of the wall, the tags were placed on small 5 cm thick polystyrene spacers.

For both the walls, to validate the measurement a wired displacement transducer was positioned at the half of the wall, in correspondence of the maximum displacement of the wall and in correspondence with the position of the two central row tags. The displacement transducer is positioned about 20 cm from the left-side Tag.

In this case, the walls will not translate rigidly because are constrained and are subjected to deformations. This means that the Tags will not have the same displacements like in the laboratory experiments.

The set up for the experimental test on the 1st wall is shown in Figure 4.27 A). The measurement acquisitions were made at each step of measurement (5

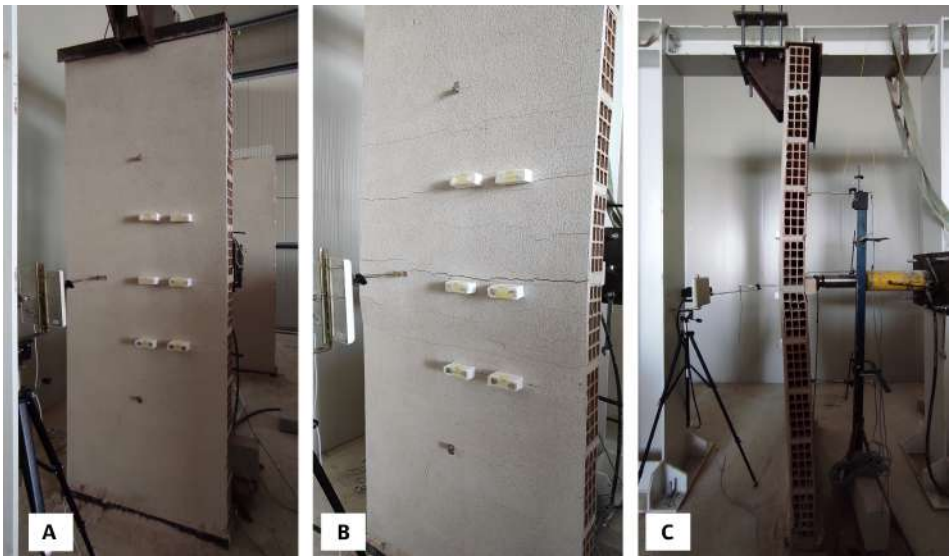

Figure 4.27. In situ experiment on the 1st wall: A) Set-up of the experimental test; B) Detail of the Tags. Deformation and cracks appear at increasing the displacement; C) Complete deformation of the wall at the final displacement of 60 mm.

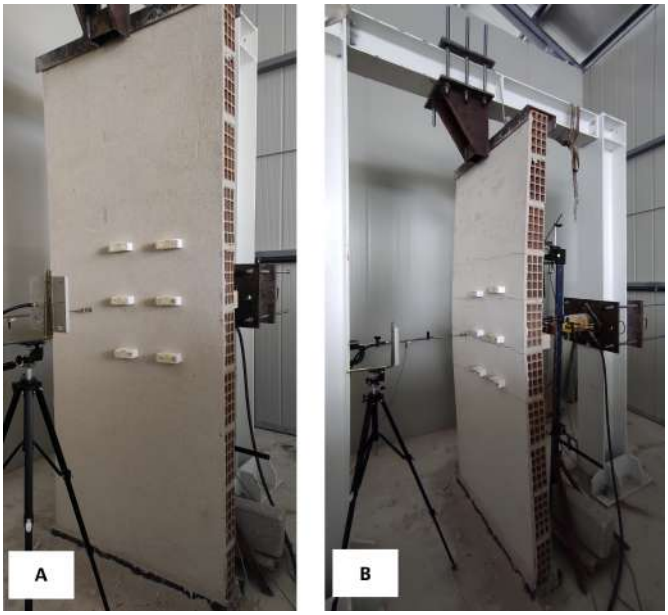

Figure 4.28. In situ experiment on the 2nd wall: A) Set-up of the experimental test; B) Complete deformation of the wall at the final displacement of 70 mm.

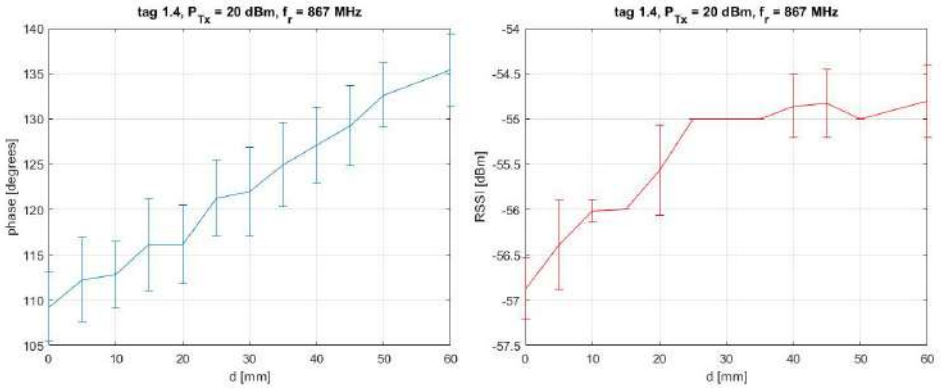

Figure 4.29. In situ experiment on the 1st wall: Tag 1.4. Mean and standard deviation values of the phase and relative RSSI values registered for each step of measurement.

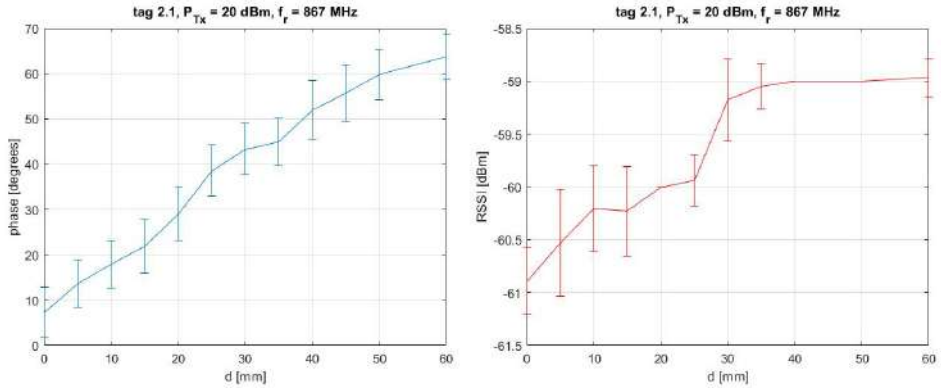

Figure 4.30. In situ experiment on the 1st wall: Tag 2.1. Mean and standard deviation values of the phase and relative RSSI values registered for each step of measurement.

mm). Figure 4.27 B) shows a detail of the wall with deformation and craks. As the displacement increases, the cracks appear and the deformation of the wall increases. The final maximum displacement and deformation are shown in Figure 4.27 C).

The set up for the experimental test on the 2nd wall is shown instead in Figure 4.28 A). The measurement acquisitions were made at each step of measurement (5 mm). Figure 4.27 B) shows a detail of the wall with deformation and craks.

4.4 Results of the in situ experimental tests

4.4.1 UHF-RFID tags displacements compared to wired transducer displacements: test on the 1st wall

The results of the acquisition systems of Tag 1.4, Tag 2.1, Tag 1.3, Tag 1.1, Tag 1.5, Tag 2.2 positioned on the 1st wall are reported in Figure 4.29, Figure 4.30, Figure 4.31, Figure 4.32, Figure 4.33, and Figure 4.34 respectively. The mean and standard deviation values of the phase registered for each step of measurement are reported for each Tag together with the relative RSSI values.

As can be observed from the graphs of Figures from 4.29 to 4.34, linear increasing values of the phase are observed for each step of measurement. This means that the Tags are sensitive to the displacements obtained at each step of measurement. The RSSI values are acceptable, quite costant for Tags 1.1, 1.3, 2.2, and with very small fluctuations for the other tags.

The detected phase differences have been converted into distance differences by using Equation (4.1).

The displacements of the tags in the out-of-plane direction, have been geometrically

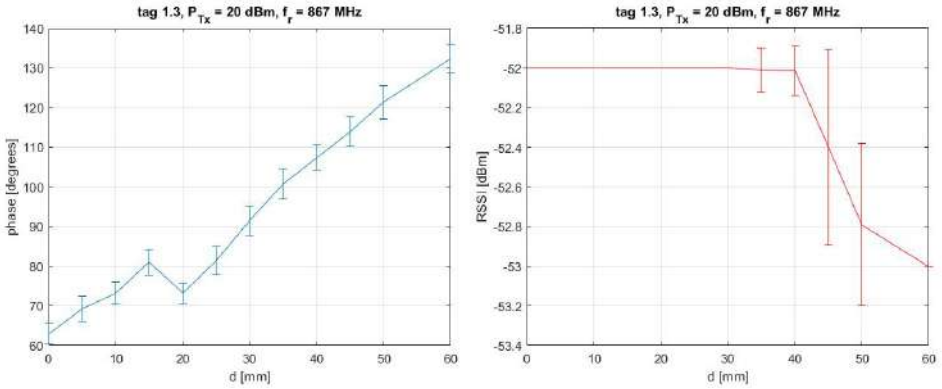

Figure 4.31. In situ experiment on the 1st wall: Tag 1.3. Mean and standard deviation values of the phase and relative RSSI values registered for each step of measurement.

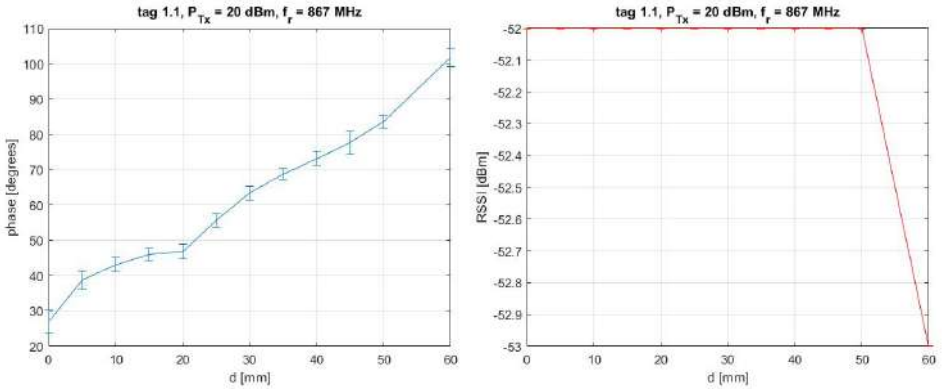

Figure 4.32. In situ experiment on the 1st wall: Tag 1.1. Mean and standard deviation values of the phase and relative RSSI values registered for each step of measurement.

calculated by a 3D modelling of the set-up. The results of displacements detected by the tags have been plotted in the following graphs, compared to the displacements detected by the wired transducer.

It is important to point out that the wall is subjected to deformations as the load cell imposes forces in the out-of-plane direction. For this reason, for the Tags positioned in the upper and lower rows it is not possible to consider as reference the measurements detected by the wired transducer that is positioned in correspondence of the central row Tags, i.e. the maximum displacement region.

The reference measurements for the upper and lower tags have been calculated according to the deformation theory, considering the wall as a beam with concentrated load in the middle and constrained with fixed joint and hinge joint.

The displacements results have been reported according to the Tags position in rows (see figure 4.25), distinguishing in upper row, central row and lower row Tags. The actual displacements detected by the wired transducer (and those calculated for the upper and lower row tags) have been plotted together for reference.

In the graph of figure 4.35 are reported the displacements detected by Tag 1.4 and 2.1 compared to the calculated displacements detected by the wired transducer (plotted as displacement reference). Figure 4.36 reports the displacements detected by central row Tags 1.3 and 1.1 and Figure 4.37 shows the displacements of the lower row Tags 1.5 and 2.2.

As can be observed from the graphs in Figures 4.35, 4.36, and 4.37, the displacements detected by the Tags during the in situ experimental test on the 1st wall are lower than those recorded by the wired transducer. Analyzing the situation in detail, some hypotheses can be advanced.

Since it was previously demonstrated that the Tags gave a good response during the laboratory tests, and since the geometry, mutual distances and power of the

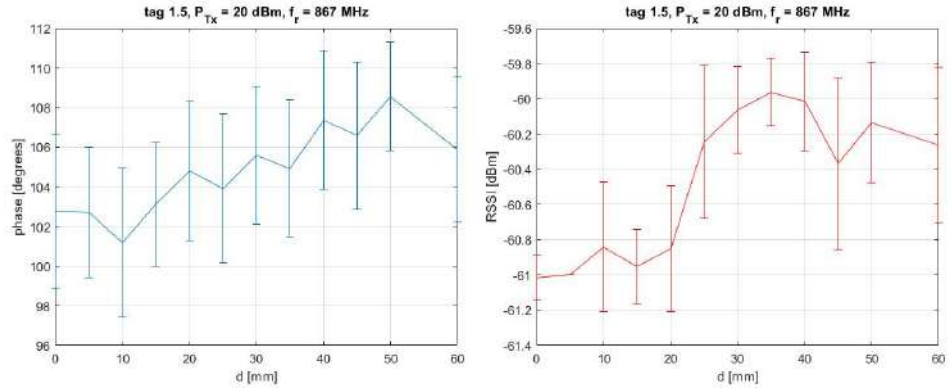

Figure 4.33. In situ experiment on the 1st wall: Tag 1.5. Mean and standard deviation values of the phase and relative RSSI values registered for each step of measurement.

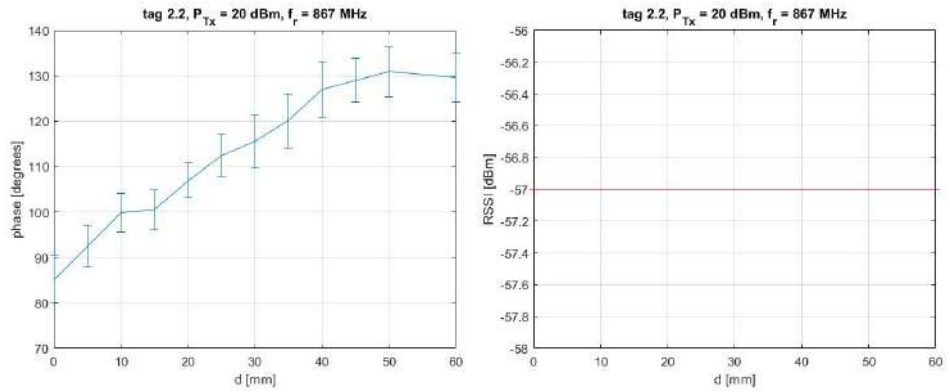

Figure 4.34. In situ experiment on the 1st wall: Tag 2.2. Mean and standard deviation values of the phase and relative RSSI values registered for each step of measurement.

acquisition system have been kept unchanged, the causes of the response anomalies are to be found in the environmental conditions of the experimental set up.

For this kind of in-situ tests, in fact, the experimental set-up requires a metal frame to constraint the wall and to fix the load cell. Moreover, the location of the steel frame necessarily near the metal wall of the building site creates a disadvantage. The high presence of metal has a negative influence on the response of the tags, showing decreased displacements compared to the actual ones.

A stronger decrease of displacements is observed for all the tags positioned on the left side of the 3x2 grid (Tag 1.4, 1.3, 1.5), compared to the tags positioned on the right side (Tag 2.1, 1.1, 2.2). This may be due to the presence of the metal wall, shown in Figure 4.27 which, despite being about 140 cm away from the tags, affected the transmission of the signal, modifying the phases and so the distances detected.

Among all the tags, the central row tags 1.3 and 1.1 shows a better response because they are nearer to the antenna.

4.4.2 UHF-RFID tags displacements compared to wired transducer displacements: test on the 2nd wall

In regards to the test performed on the 2nd wall, the results of the signal acquisition of Tag 2.4, Tag 2.2, Tag 2.1, Tag 1.4, Tag 2.3, Tag 1.2 are reported in Figure 4.38, Figure 4.39, Figure 4.40, Figure 4.41, Figure 4.42, and Figure 4.43, respectively. The mean and standard deviation values of the phase registered for each step of measurement are reported for each Tag together with the relative RSSI values.

The displacements of the tags in the out-of-plane direction, have been geometrically calculated by the 3D modelling of the set-up. The results of the tags displacements

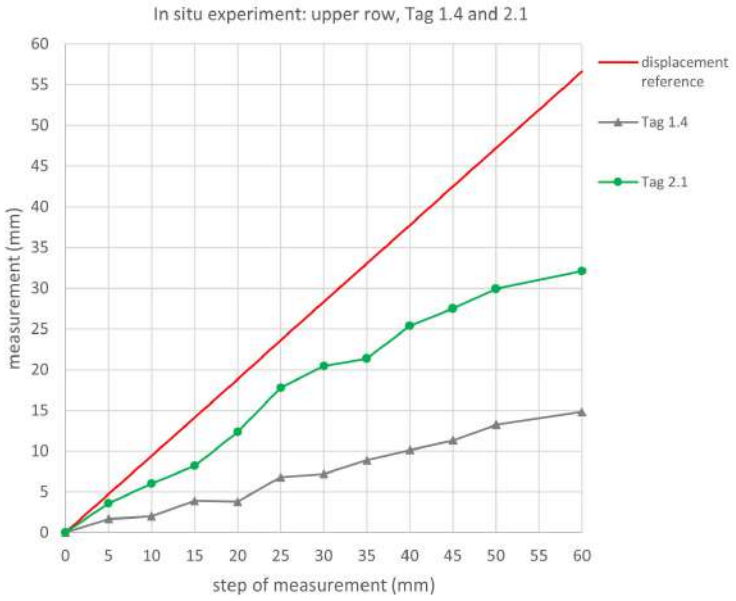

Figure 4.35. In situ test on the 1st wall: Upper row Tag 1.4 and 2.1. Displacements detected by the Tags compared to the calculated displacements detected by the wired transducer.

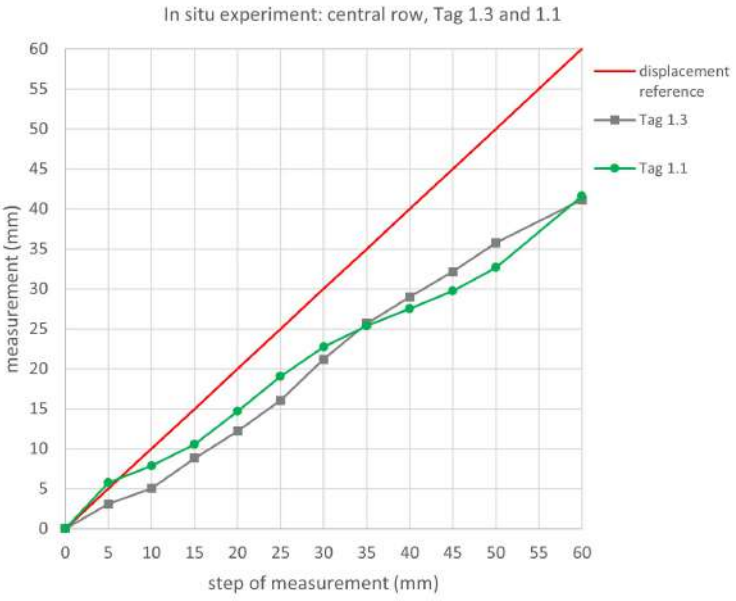

Figure 4.36. In situ test on the 1st wall: Central row Tag 1.3 and 1.1. Displacements detected by the Tags compared to the displacements detected by the wired transducer.

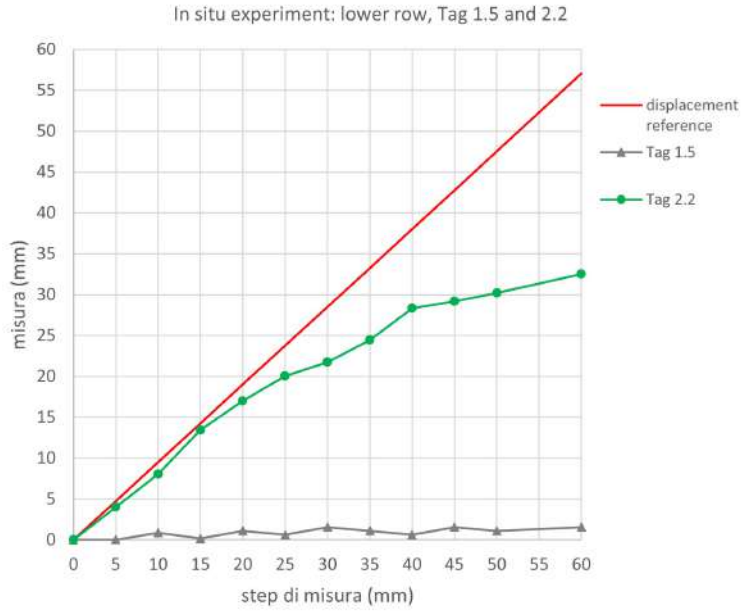

Figure 4.37. In situ test on the 1st wall: Lower row Tag 1.5 and 2.2. Displacements detected by the Tags compared to the calculated displacements detected by the wired transducer.

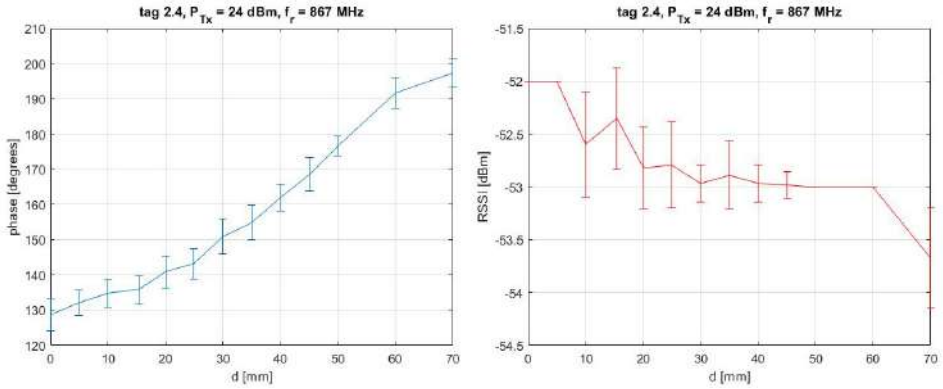

Figure 4.38. In situ experiment on the 2nd wall: Tag 2.4. Mean and standard deviation values of the phase and relative RSSI values registered for each step of measurement.

have been plotted in the following graphs, compared to the displacements detected by the wired transducer.

Also in this case, The reference displacements for the upper and lower row tags have been calculated according to the deformation theory, and have been plotted together with the results of the tags for reference.

The displacements results have been reported according to the Tags position in rows (see figure 4.26).

As can be observed from the graphs of Figures from 4.38 to 4.43, linear increasing phase values at each step of measurement are detected from the starting point 0 mm to the final point 70 mm. Also in this case the Tags are sensitive to the displacements of the wall. The distance differences have been calculated according to Equation (4.1).

In the graph of figure 4.44 are reported the displacements detected by Tag 2.4 and 2.2 compared to the calculated displacements detected by the wired transducer (plotted as displacement reference). Figure 4.45 reports the displacements detected by central row Tags 2.1 and 1.4 and Figure 4.46 shows the displacements of the lower row Tags 2.3 and 1.2.

As can be observed from the graphs in Figures 4.44, 4.45, and 4.46, the displacements detected by the Tags during the in situ experimental test are lower than those recorded by the wired transducer also in this case. Substantially, the

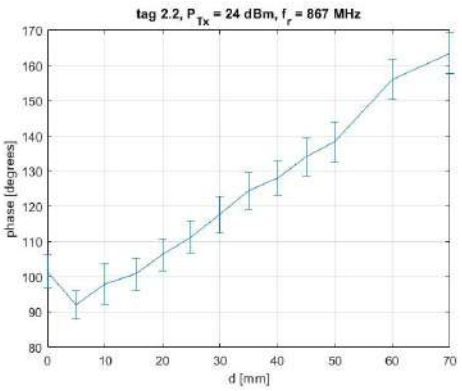

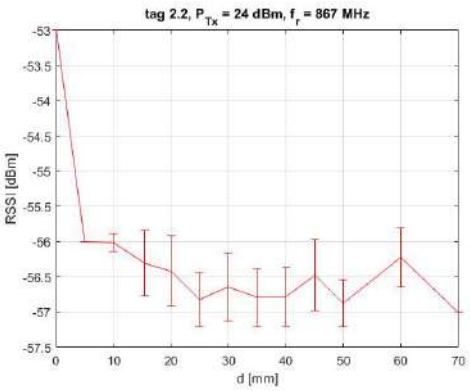

Figure 4.39. In situ experiment on the 2nd wall: Tag 2.2. Mean and standard deviation values of the phase and relative RSSI values registered for each step of measurement.

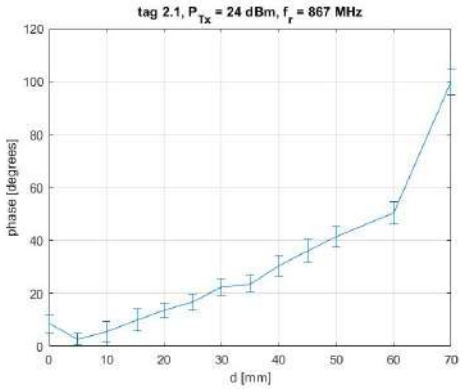

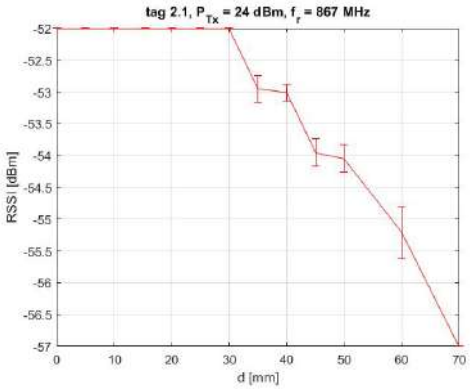

Figure 4.40. In situ experiment on the 2nd wall: Tag 2.1. Mean and standard deviation values of the phase and relative RSSI values registered for each step of measurement.

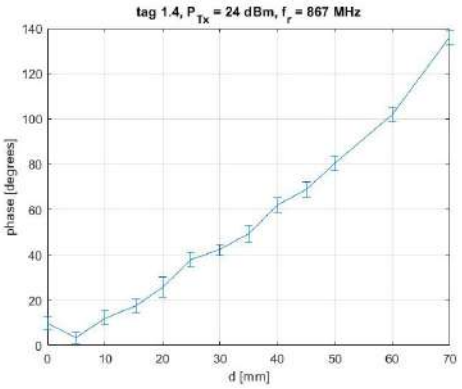

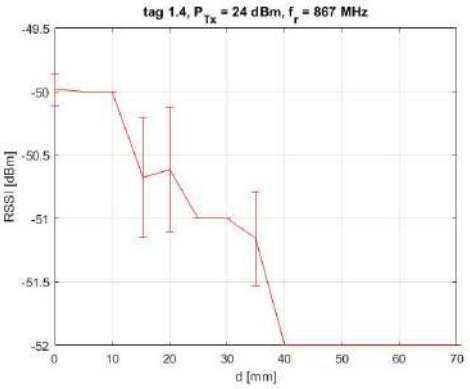

Figure 4.41. In situ experiment on the 2nd wall: Tag 1.4. Mean and standard deviation values of the phase and relative RSSI values registered for each step of measurement.

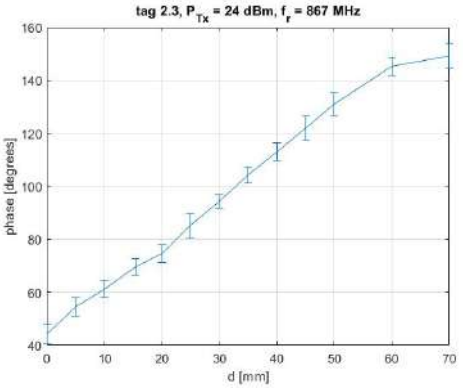

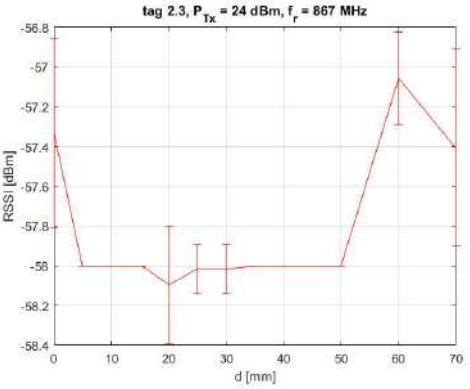

Figure 4.42. In situ experiment on the 2nd wall: Tag 2.3.

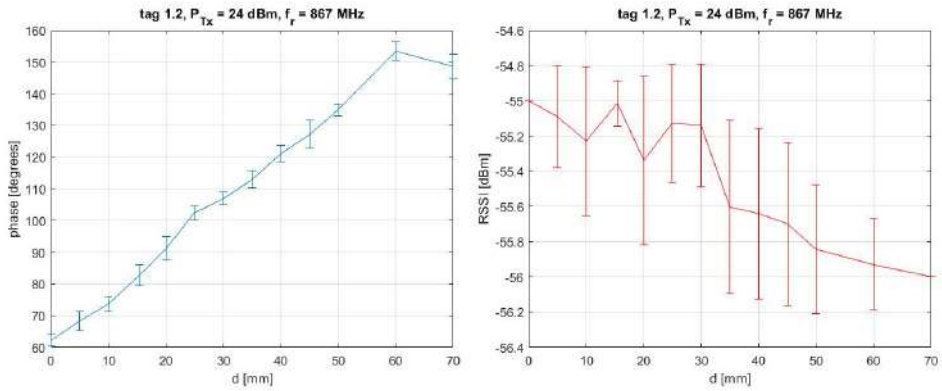

Figure 4.43. In situ experiment on the 2nd wall: Tag 1.2. Mean and standard deviation values of the phase and relative RSSI values registered for each step of measurement.

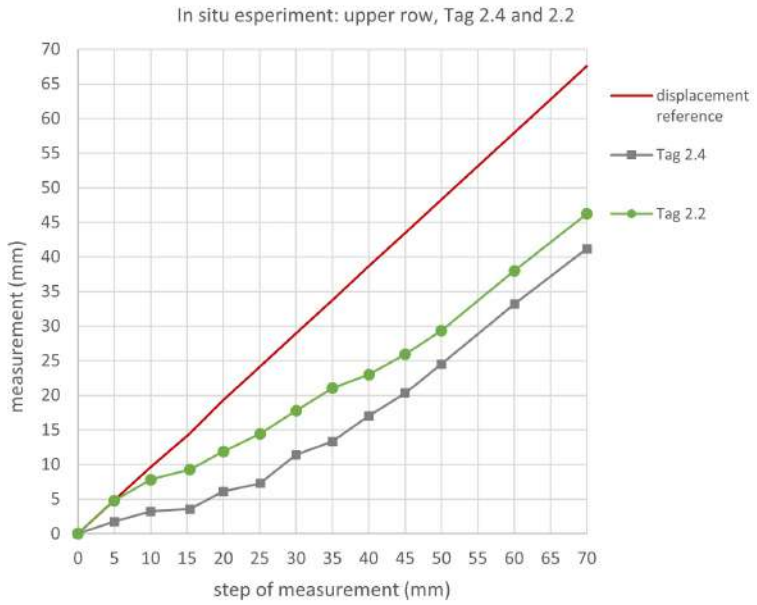

Figure 4.44. In situ test on the 2nd wall: Upper row Tag 2.4 and 2.2. Displacements detected by the Tags compared to the calculated displacements detected by the wired transducer.

Figure 4.45. In situ test on the 2nd wall: Central row Tag 2.1 and 1.4. Displacements detected by the Tags compared to the displacements detected by the wired transducer.

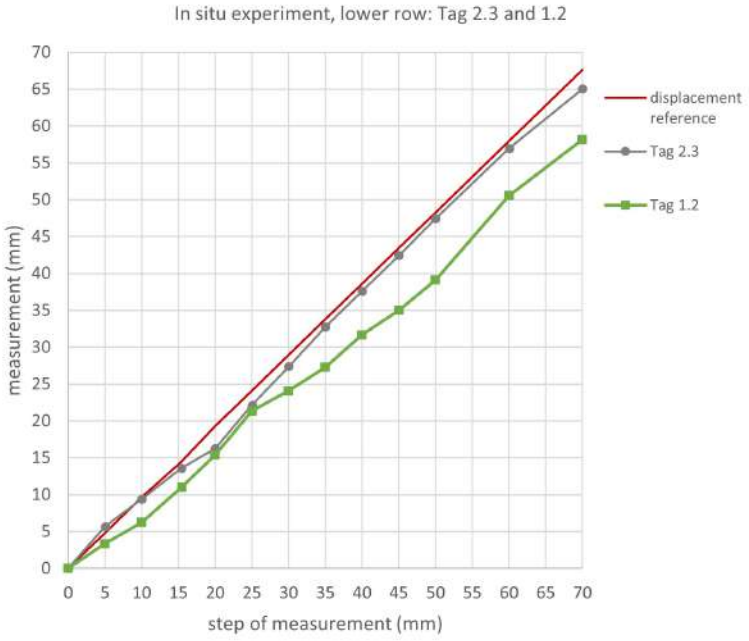

Figure 4.46. In situ test on the 2nd wall: Lower row Tag 2.3 and 1.2. Displacements detected by the Tags compared to the calculated displacements detected by the wired transducer.

same hypotheses made for the test on the 1st wall can be advanced.

Also in this case, since the geometry, mutual distances and power of the acquisition system have been kept unchanged (compared to the laboratory test with the same tags), the causes of a lower response are due to the environmental conditions of the experimental set up.

The metal frame used to constraint the wall and to fix the load cell, the metal wall of the building site, all contribute to negatively affect the response of the tags, showing decreased displacements compared to the actual ones.

In particular, also in this test a stronger decrease of displacements is observed for the tags positioned on the left side of the 3x2 grid (Tag 2.4 and 2.1), except for Tag 2.3.

Tag 2.3 in fact is the only Tag that correctly matches the actual displacements.

The tags positioned on the right side are less affected by the presence of the metal, in particular Tag 1.4 and 1.2.

In this test, it is observed a general better response for the lower row Tags. It's not easy to establish the causes, but it is supposed that the environment and its interferences are crucial in determining a good response.

4.5 Conclusions

In this study, the use of commercial UHF-RFID tags (not embedded in antennas) has been investigated to be employed for civil engineering purposes, specifically for the monitoring of out-of-plane displacements of brick walls. The innovation of the research is represented by the novelty of the application of commercial tags, usually used in logistic and other purposes, in civil engineering. The feasibility of the application of this technique was asses by experimental campaigns carried out first in laboratory, then in situ. The experimental set-up of the laboratory campaigns was organised taking into account the in-situ distances and spaces, in order to make then a comparison of the results in the same conditions, except for

the environment.

The laboratory campaigns showed a very good response of the tags. The displacements in fact matched almost perfectly with those imposed. A weaker response of some Tags can be attributed to environmental interference together with the position of the tags with respect to the antenna. Moreover, the intrinsic measurement errors of the reader itself and the errors in processing the received data (standard deviations of the calculated mean values of the phases) should be considered.

The response of the Tags in laboratory environment demonstrated to be very satisfactory, proving that the new application of wireless RFID tags for the monitoring of out-of-plane displacements is feasible and potentially very reliable.

In situ experiments showed a weaker response of the Tags which registered displacements lower than those recorded by the wired transducer used as reference. The environmental conditions can be supposed to be the causes. The high presence of metal affected negatively the transmission of the electromagnetic signals, modifying the phases and consequently the indirect measures of displacements.

Unluckily, the set-ups of the in-situ tests required steel frames to constraint the single walls and to fix the load cell. Moreover, the position of the experimental set-ups necessarily near the metal wall of the building site contributed to negatively affect the displacements results.

According to the experimental results, the application of these specific commercial Tags can not be considered completely reliable, since are strongly affected by the environment conditions.

Technology limits related to environment interference can be overcome with the design of different UHF-RFID Tags with specific features. Of course the design of a new tag should guarantee the same advantages of the tags currently available on the market (cost-effectiveness, small size) with better performances in regards to the influence of metallic object and areas in the environment.

In conclusion, it can be stated that the application of UHF-RFID tags in civil engineering applications is promising and opens up new scenarios for the design of new wireless devices suitable to meet the required needs. The use of this new measurement technology allows the advantage of a wireless, low-cost, non-invasive, and widespread monitoring.

New wireless RFID sensor for crack width monitoring

5.1 Introduction

All structures are subject to deformation and cracks, due to fatigue, stress and/or environmental factors. It is therefore of maximum importance to monitor the mechanical condition of critical structures, in order to prevent catastrophic failures, but also to minimize maintenance costs. Several technologies and systems can be used for this purpose: among them, proposing the use of wireless passive RFID crack width sensors has a strong potential, in terms of simplicity of installation and measurement, and low cost.

In the present work the development and application of a new wireless RFID sensor for crack width monitoring is presented. The device was conceived together with colleagues of the Department of Industrial and Information Engineering and Economics (DIIIE) of the University of L'Aquila. It is conceived as an RFID tag with bifilar transmission line which is able to detect sub-millimeter deformations occurring on the crack area. A design method based on high sensitivity phase detection is shown.

To evaluate the effectiveness of the proposed measuring method and device, an experimental campaign was carried out. In particular, three-point bending tests were carried out on bricks of three different materials (unreinforced mortar, reinforced mortar with PVA fibers, and reinforced mortar with basalt fibers). Crack width measurements were carried out using the wireless crack meter and, at the same time, a wired displacement transducer for comparison. The feasibility of this new method and device was investigated.

5.2 Background: crack width monitoring sensors and methods

In the assessment of the general state of the health of a structure, cracks must be reliably quantified. Detailed visual inspection of the surface of the structure remains a common method for detecting cracks; systematic crack mapping allows inspectors to monitor the progression of cracks and to hypothesize the nature of

their origins (Bungey and Grantham, 2006). Frequency of inspection depends on the design, past performance, or age of the structure. Generally, after suspicious cracks are detected, nondestructive and partially-destructive testing are carried out to determine crack features that may fall below the surface. However, all of these methods require the use of trained personnel for execution, resulting in tedious, time consuming, and expensive procedures.

During the past years, a wide variety of approaches have been proposed for the monitoring of cracks. These techniques can be divided into wired and wireless technologies, according to their use.

Among the wired ones, Lecompte et al. (2006) used the application of digital imaging processing techniques for the identification of crack locations and widths, implementing the use of charge-coupled device (CCD) cameras to capture photographic images. Johnson (2006) used a built C-shaped crack gauge to observe the surface crack in concrete members. The C-shaped gauge measured the relative movement between the two ends of the mechanism. Kuang et al. (2003) proposed instead the use of optical fibers to detect hairline cracks and to monitor cracks propagation up to the point of ultimate failure. Also Ravet et al. (2009) used fiber optic systems.

However, such systems involve a time consuming installation, due, among others, to wiring problems; moreover, they are quite expensive, because of the complicated manufacturing as well as the extensive signal processing.

In this regard, wireless sensors are gaining a growing interest thanks to the fast and easy installation (Saad, 2011).

In particular, passive wireless systems which harvest their energy from the environment or collect it from the powered read-out unit during the wireless communication have a simpler electronics and enable hence lower costs. A large deployment of such sensors can be used as a "monitoring ecosystem", where the passive sensors would detect problems with a low cost infrastructure spread out over the area to monitor (Caizzone and DiGiampaolo, 2015). This concept is well suited for monitoring the evolution also of already existing cracks in historical buildings.

In this case, the low-cost wireless passive sensor proposed, able to detect sub-millimeters crack width variations in a range of few millimeters, at distances of few meters, could represent a new promising monitoring system.

5.3 New wireless crack width sensor: RFID Tag with bifilar transmission line

The proposed instrument is a completely passive tag composed of a pair of coupled dipole antennas. The dipoles are made of copper (350 μm thick) on an FR4 substrate. The total dimensions of the tag are $134 \times 50 \times 0.8$ mm^3. Dipoles ports are respectively connected to a NPX G2XM series UHF-RFID chip, and to a bifilar transmission line, consisting of two 50 mm long, parallel copper conductors with a diameter of 0.8 mm, posed at a distance of 2 mm from each other. The tag is presented in Figure 5.1.

In the proposed tag, the UHF-RFID chip has certain impedance characteristics at the frequency of interest (867 MHz) that is counterbalanced by the bifilar transmission line impedance. By varying the distance between the two filiform conductors, an impedance variation due to their progressive electromagnetic decoupling

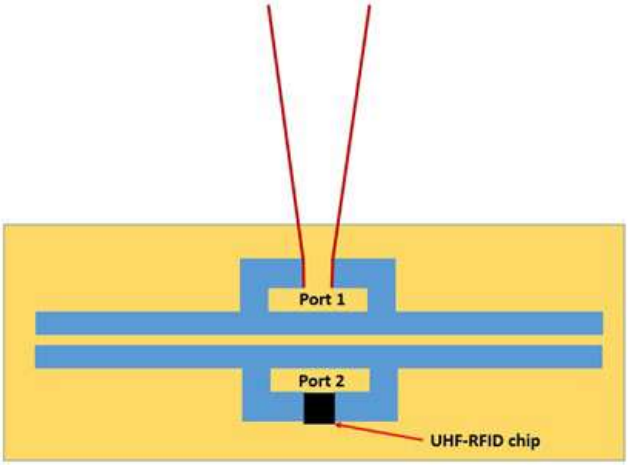

Figure 5.1. Proposed bifilar transmission line based UHF-RFID tag.

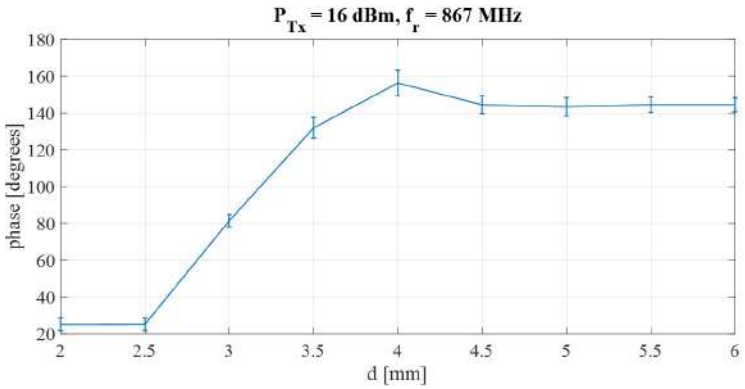

Figure 5.2. Measured backscattered phase signal vs. distance between filar conductors.

is applied. This phenomenon can be verified during the reading phase of the tag. As the distance between the filar conductors varies, a variation in the phase of the tag back-scattered signal occurs.

The determination of the behavior just described and the final length, are obtained by solving the Riccati equations, which cannot be calculated in closed form. This problem was solved through analyzes based on the method of moments, which better approximate this type of scenario. Figure 5.2 shows the measured back-scattered phase signal vs. distance between the bifilar conductor. This phase is obtained with the antenna positioned at a distance of 1 m from the tag. As shown in figure 5.2, at the moment the proposed tag is able to read width from 2.5 mm to a maximum of 4.5 mm, with a sensitivity of 0.001 mm.

5.4 Experimental investigation: three-point bending tests on lime-based mortar bricks

To evaluate the effectiveness of the proposed device and measuring method, an experimental campaign was carried out. Three-point bending tests were carried out on bricks of three different materials: unreinforced mortar, reinforced mortar with PVA fibers, and reinforced mortar with basalt fibers, for a total of 9 samples, in order to monitor the width of the generated crack.

The preference of a reinforced mortar with fiber is due to the ability of short-fibers to enhance the mechanical properties of materials characterized by a brittle nature with a low tensile strength and strain capacity (Pakravan et al., 2017).

Figure 5.3. Detail of the specimens of mortar with the notch and the thin wooden rods.

In fact, incorporating fibers increases the strength (Lee and Ryu, 1999), and also provides great benefits especially in the softening phase when the maximum resistance of the material is achieved, preventing the brittle collapse of the material and permitting to have a more controlled initiation and propagation of cracks (Yao et al., 2003), very suitable for the monitoring purpose of this study. Moreover, These kinds of new reinforced mortar are conceived to be compatible with the old constituent material of existing historical masonry, in fact they are used recently in reinforcement systems for the strengthening of the walls of historical stone buildings because they may ensure an adequate safety level for seismic forces acting in any direction. The monitoring of cracks is very important to prevent damage, especially in historical buildings, and for all these reasons, the tests has been conducted with this kind of materials.

It is necessary to specify that the study of the mechanical properties and composition of the different materials and fibers is not of interest in order to monitor the cracks width. For this reason, they are not reported in this study.

Crack width measurements were carried out using the wireless crack meter and, at the same time, a wired displacement transducer was placed on the sample for comparison.

The test was performed on a displacement controlled hydraulic testing machine (Zwick—Roell). Three samples of three different kind of mortar were tested. The 28 days bricks were casted with dimensions of 160 mm x 4 mm x 4 mm according to the standard code EN 1015-11 (European Committee for Standardization, 2007).

A 2 mm thick notch was realized on each sample with a depth of 6 mm by using a sawing, resulting with a notch-to-beam depth ratio of 0.15. The notches were realized on the samples to minimize irreversible deformations outside the fracture zone, avoiding large parts with high stresses outside this zone (Angiolilli et al., 2020).

For each sample, over each side of the notch, two wooden rods thin 0.8 mm were glued, which serve to accompany the opening of the bifilar transmission line of the wireless sensor as the opening of the crack progresses, thus allowing to register the progressive crack width (see figure 5.3). The wooden rods were positioned with a mutual distance of 2 mm (the minimum distance between the two threads of the bifilar line of the sensor in the starting condition).

The specimens were loaded at a constant displacement rate of 0.3 mm/min until a maximum width of 6 mm was achieved.

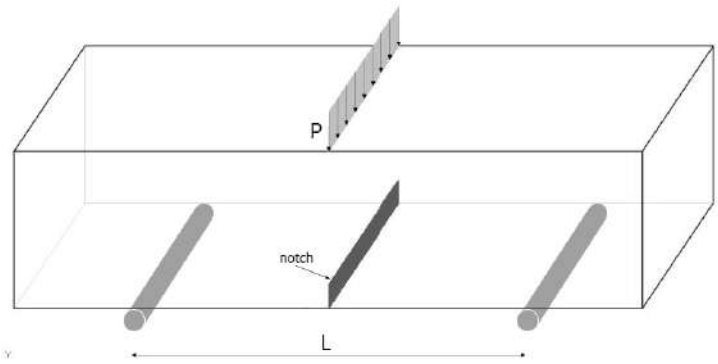

Figure 5.4. Scheme of the three-point bending test on the specimens

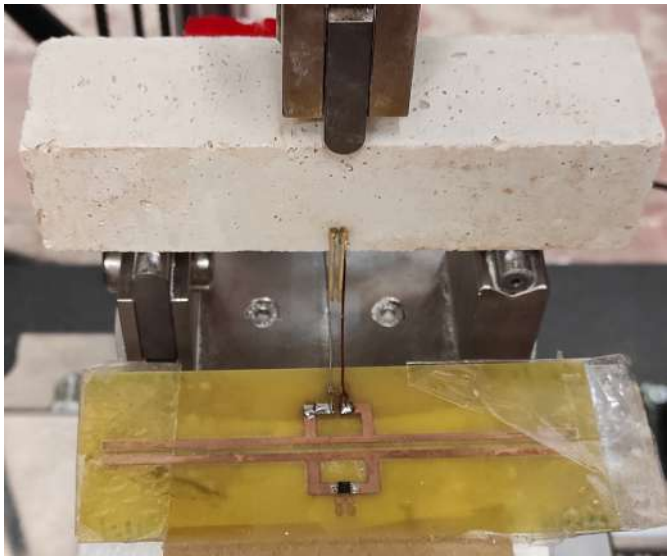

Figure 5.5. Detail of the wireless Tag with the wooden rods inside the bifilar line of the tag which allow to record the crack width opening.

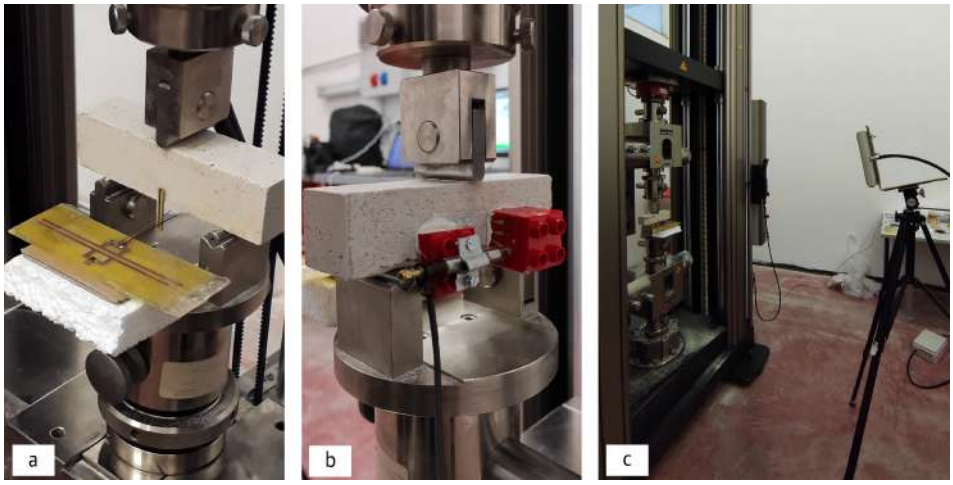

Figure 5.6. Experimental set up: a) detail of the front side of the sample and wireless tag; b) detail of the back of the sample and wired displacement transducer; c) complete set up with the antenna at 1.5 m.

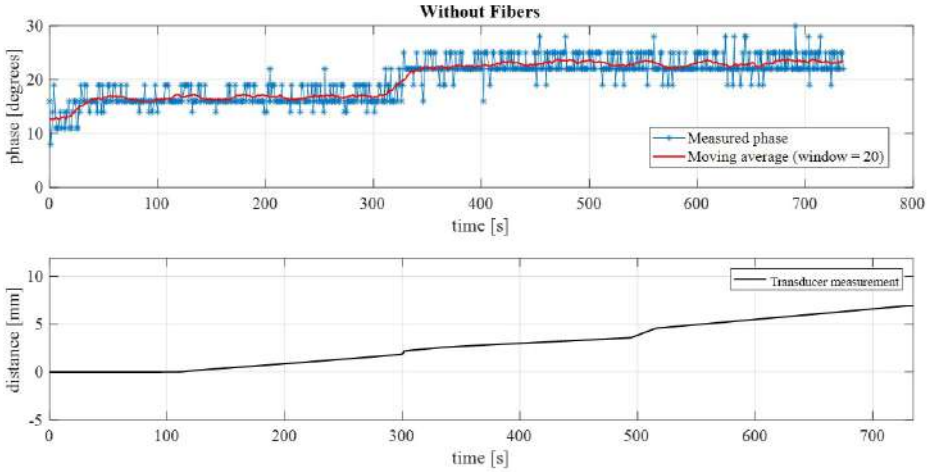

Figure 5.7. Mortar without fibers: phase values recorded by the wireless tag compared to the crack width recorded by the displacement transducer.

The scheme of the set up for the three-point bending test is illustrated in Figure 5.4. In particular, the nominal distance L between the supports was 100 mm, whereas both the width and thickness of each sample were equal to 40 mm. The loading P was introduced at the mid-span of the brick. The two rollers at the bottom allowed for the free horizontal movement.

The wireless Tag was positioned near the plate of the testing machine, with the bifilar line in correspondence of the notch and the wooden rods (see Figure 5.5) and the antenna was positioned at a distance of 1.5 m.

On the opposite side of each sample, a wired displacement transducer was fixed as reference for the crack width measuring, in order to validate the proposed sensor and method.

Details of the set up are depicted in Figure 5.6. In particular, in Figure 5.6 a) it is shown the front size of the sample, with the new tag, whereas in Figure 5.6 b) it is shown the back side of the sample on which the wired displacement transducer was positioned for reference. In figure 5.6 c) instead it is represented the entire set up including th antenna positioned at a distance of 1.5 m.

The antenna operates at 867 MHz and the power of the signal was set up at 24 dBm. The specimens were loaded at a constant displacement rate of 0.3 mm/min until the maximum value of the crack width. The acquisition of the signal by the wireless tag was continuous during the entire duration of the test, with a sampling rate of 2 seconds. The acquisition of the wired transducer was also continuous and set at the same sampling rate. The acquisition of the wireless tag and the wired transducer were synchronized to obtain comparable results.

5.5 Experimental results

For each type of material, the clearer recorded phase signal has been reported in the following graphs, compared to the relative displacement transducer measurement. In figure 5.7 two graphs relative to the mortar without fibers are shown. In the first graph, the phase values recorded by the wireless tag have been reported. The moving average of the phase values has been highlighted in red. In the second graph, the values of the crack width vales recorded at the same time by the wired displacement transducer have been reported for comparison.

A slight increasing of the phase signal can be noticed, in particular with a phase

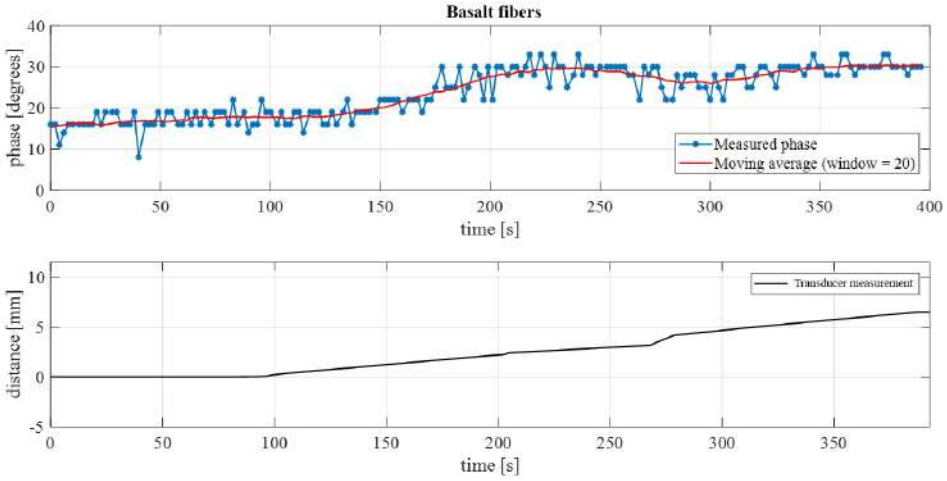

Figure 5.8. Mortar with basalt fibers: phase values recorded by the wireless tag compared to the crack width recorded by the displacement transducer.

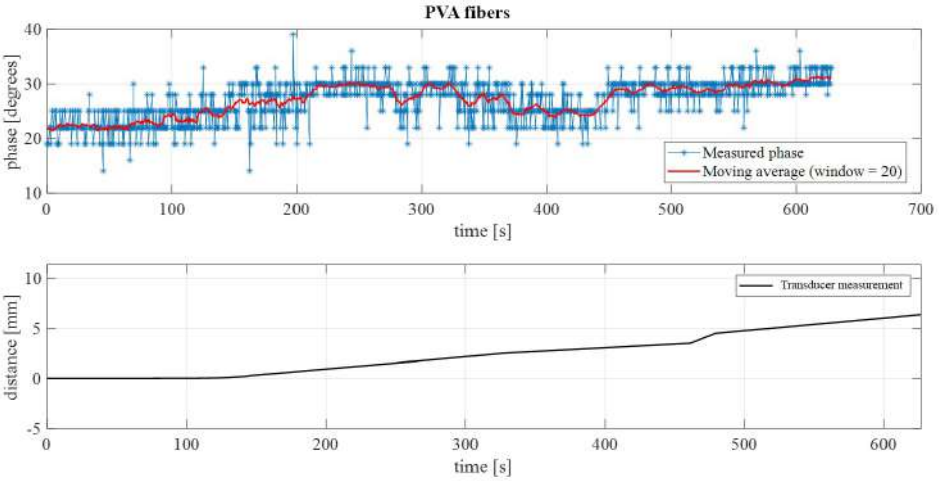

Figure 5.9. Mortar with pva fibers: phase values recorded by the wireless tag compared to the crack width recorded by the displacement transducer.

jump in correspondence of the interval between 300 and 500 seconds. Since both the sensors were synchronized before starting the acquisition, it can be reasonably assumed the the phase jump corresponds to the interval between 2.5 mm and 4.5 mm, which is the one in which the wireless senor is sensitive.

In figure 5.8 the graphs relative to the mortar with basalt fibers are reported. In the first graph, the phase values recorded by the wireless tag have been reported, with the moving average in red. In the second graph, the values of the crack width recorded at the same time by the wired displacement transducer are reported.

In this case, results in figure 5.8 show that the phase increases progressively. Its seems to have detected the increasing opening of the crack. The same can be noticed in Figure 5.9 which reports the results relative to the mortar with pva fibers.

Comparing these results with the expected response of the wireless tag in Figure 5.2, it is noted that for the same distance (2.5 - 4.5 mm)the phase jump is lower in the experimental campaigns. In fact, in Figure 5.2 the phase jumps is about 100 degrees and in the experimental tests the maximum phase jump is about 15 degrees. It can be supposed that the high quantity of metal of the test machine may have strongly influenced the signal reception. Of course, it is demonstrated that the metal strongly affect the acquisition of the signal and consequently the phase-to-distance correspondence. At least, in figure 5.9 the graphs relative to the mortar with pva fibers are reported. In the first graph, the phase values recorded by the wireless tag are reported with the moving average in red. In the second graph, the values of the crack width recorded at the same time by the wired displacement transducer are reported.

5.6 Conclusions

The new wireless RFID sensor developed to monitor crack width gave a discrete response. It should be considered that the devise is in a raw form and requite technological development in order to be improved and applied on a large scale, but the potential in structural monitoring could be very high. Many difficult aspects like the strong influence of metal can be overcome in the next step of design of the tag. Compared to traditional crack width measurement procedures, the proposed new technique results potentially more suitable. In fact, the interrogation distance in this raw state is 1.5 m which is notable, and could be extended more to allow the positioning of these devices in points difficult to access with traditional wired devices. Moreover the proposed wireless sensor is made with low cost components and this represents of course and advantage in widespread monitoring. Further investigation is surely required.

Dynamic assessment, modelling, and parametric updating of a butterfly-arch stress-ribbon pedestrian bridge

6.1 Introduction

In this chapter a large-scale approach to wireless structural monitoring is reported. This study has been developed in collaboration with Fuzhou University, in Fuzhou, China. The dynamic identification and finite element (FE) modelling of a butterfly-arch stress-ribbon pedestrian bridge located in Fuzhou University was developed.

The current research focuses on the dynamic assessment (through the use of a WSN) and finite element (FE) modelling of a stress-ribbon footbridge located in Fuzhou University, Fuzhou, Fujian, China. The current case study is the first example of this structural system in China (He et al., 2019) and not many others of this particular kind are present worldwide, representing an important reason for investigating it. In particular, the structure considered in this study is not similar to conventional stress-ribbon footbridges, being based on a novel design concept: the combination of a stress-ribbon deck and a butterfly-arch bridge that provides the solution for a self-anchored structural system (Strasky, 2010).

The aim of this research is to study the dynamic behaviour of the structure and develop a sensitivity-based FE model which can serve as the baseline for a long-term monitoring of the bridge during its life-cycle. Besides, the study of this particular structure can also show some recommendations for the modelling and analysis of this particular kind of footbridges.

6.1.1 background: Stress-ribbon structures

Stress-ribbon structures represent an elegant and environmental-friendly solution for pedestrian bridges (Briseghella et al., 2012; Liu et al., 2016; Strasky, 2005; Zordan et al., 2014). The elegance of the structures originates from the structural system's simplicity, consisting of a prestressed concrete deck supported by suspension

cables. The suspension cables are embedded in the deck, which follows a catenary arch between the supports. The environmental-friendly characteristic of these structures derives from the economy of building materials requested for their erection. The first stress-ribbon bridge was the Leonel Viera Bridge, completed in 1965, and after this, several similar structures were built worldwide. Stress-ribbon bridges are a very appealing architectural system due to the aesthetic balance of the structural layout. However, fashion attractiveness derives from structural slenderness, which may imply several drawbacks. These structures are characterised by very low natural frequencies, making the deck sensitive to the effect of human-induced vibrations. Therefore, several scholars dedicated their research efforts to the dynamic identification and long-term monitoring of these structures. Caetano and Cunha (2004); Cunha et al. (2005); Hu et al. (2013) focused on the dynamic characterisation and subsequent long-term monitoring of a stress ribbon footbridge constructed in Porto, Portugal. The first researches reported dynamic identification via Input-Output and Output-only methods, the more recent one presents the results from long-term dynamic monitoring. The bridge is a very slender structure with first natural frequency close to 0.9 Hz. Consequently, this bridge is very prone to exhibit uncomfortable vibrations due to walking excitation. They observed that existing formulations for predicting the maximum acceleration response overestimate the experimental finding. Specifically, they measured an approximate 0.44 m/s^2 maximum acceleration due to a walking pedestrian. Additionally, they found that the synchronised motion of 22 pedestrians with a pacing rate of about 2 Hz did not cause accelerations over 2 m/s^2. Interestingly, stress-ribbon bridges with a reduced span may exhibit a vibration response lower than expected. Cara et al. (2017); Soria et al. (2016) also investigated the dynamic response of stress-ribbon structures, but they did not direct on the estimation of the human-induced vibrations. The proneness to exhibit uncomfortable vibrations entailed the development of passive (Caetano et al., 2010,?; Sétra, 2006) and active vibration control systems (Bleicher et al., 2011).

6.2 Description of the butterfly-arch stress-ribbon pedestrian bridge in Fuzhou, Fujian, China

The butterfly-arch stress-ribbon pedestrian bridge in Fuzhou is composed of a stress-ribbon deck and two outward inclined Concrete-Filled Steel Tubular (CFST) arches with interconnecting steel beams (Figure 6.1). Since the construction site is on deep soft soils, the structural solution of a stress-ribbon arch bridge became a perfect choice for its aesthetic values and the self-anchored system, which loads the foundation only in the vertical direction. The span of the prominent steel tubular arches is 25 m with a rise of 5.5 m, see Figure 6.1 and Figure 6.2. The dimensions of the cross sections are 42.6 cm-diameter and 1.6 cm-thickness. An outward inclination angle of 30 degrees (counted from the vertical direction) is provided for the prominent arches known as the butterfly arches. There are also secondary steel tubular arches with a smaller cross section of 37.7 cm-diameter and 1.6 cm-thickness, for a span of 16 m. Welded joints are designed between the main and secondary arches and between the cross beams and secondary arches. The stress-ribbon deck is assembled from precast concrete segments (each one 6 m in width, 1.15 m in length and 0.25 m in thickness) and is prestressed by two external

Figure 6.1. The butterfly-arch stress-ribbon pedestrian bridge in Fuzhou University, Fuzhou, Fujian, China.

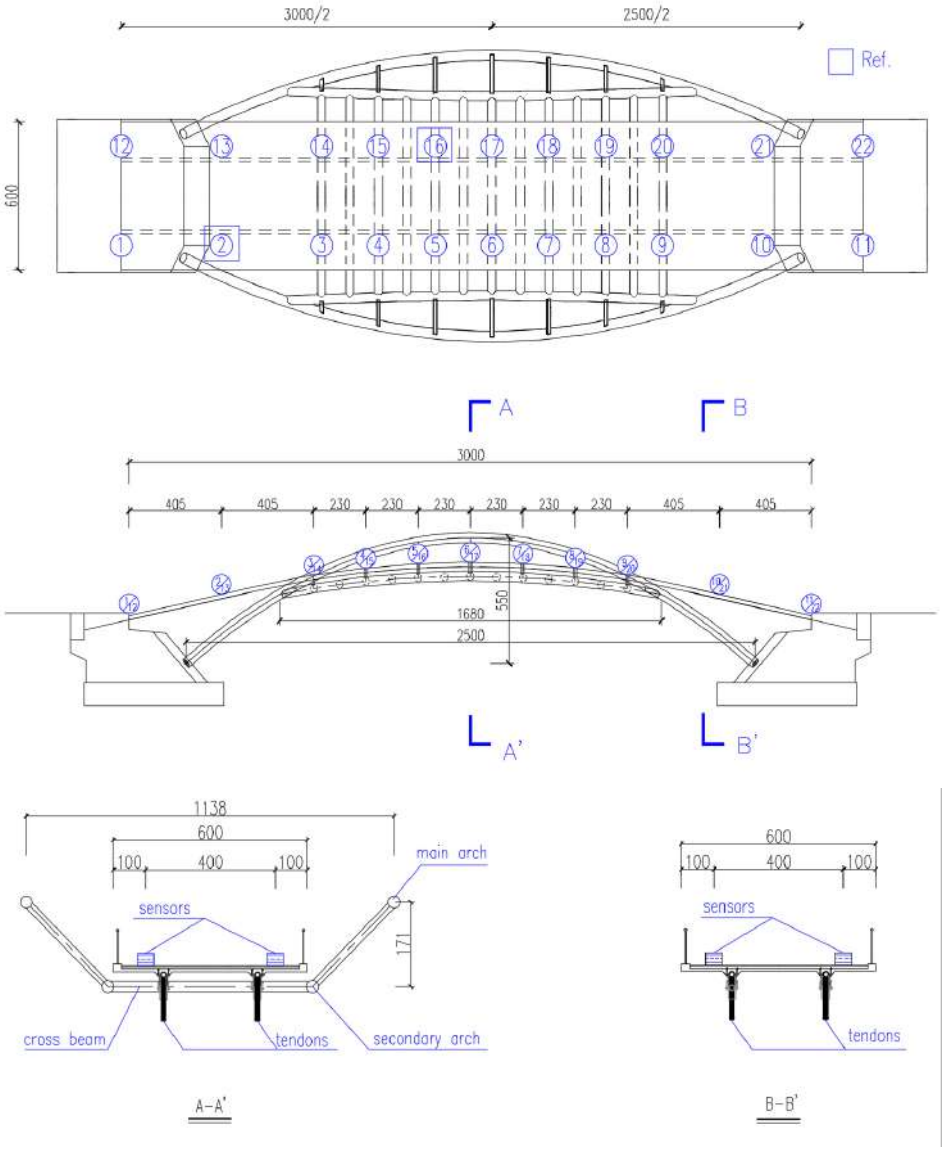

Figure 6.2. Locations of the measurement nodes, labelled from 1 to 22: top view (a), front view (b), sections (c). The reference nodes are node 2 and node 16. (units in cm).

tendons. The tendons are formed by two bundles of 12×Φ15.2 mm mono-strands grouted inside the galvanised steel tubes. The central part of the deck over the river simply rests on the cross beams, while the side parts of the deck hang down freely between the cross beams and the abutments.

6.3 Dynamic assessment

6.3.1 Operational Modal Analysis

Operational Modal Analysis (OMA) was performed on the bridge in March, 2019. In total, twenty-two nodes were measured on the bridge deck. Figure 6.2 explains the setup for the measurement nodes. The acquisition system used was the GMSplus wireless measurement system of the GeoSIG company, sampling at 200 Hz. Two reference sensors and two roving sensors were used for a total of 11 experimental setups. For each setup, the reference sensors were fixed in Node 2 and Node 16. The choice of reference nodes was derived from a study of the numerical modal characteristics as predicted by a preliminary FE model. The roving sensors, instead, were moved from the right side of the bridge to the left side of the bridge (see Figure 6.2) i.e. for setup no. 1 at Node 11 and Node 22, for setup no. 2 at Node 10 and Node 21, and so on, until setup no. 11 at Node 1 and Node 12. The roving sensors were placed adjacent to the reference ones at the reference nodes. Each sensor unit was embedded with the tri-axial MEMS accelerometer, which allowed for the synchronous record of the structural vibration responses in all the vertical, transversal and longitudinal directions. The measurements period was 15 minutes for each experimental setup. During the testing period, the bridge was under ambient excitation, which included mild winds and low-density pedestrians. In particular, the traffic situations can be classified as "individual pedestrians and small groups" (Feldman, 2008).

6.3.2 Signal processing and modal identification

Signal processing and system identification were carried out by using the MACEC software (Reynders et al., 2011). Modal identification was performed by using the reference-based Stochastic Subspace Identification (SSI) algorithm (Peeters and De Roeck, 1999). Identification results of the OMA are provided in 6.3. In particular, eight modes were identified: five vertical bending modes V1, V2, V3, V4, V5, and three torsional modes T1, T2, T3. Most of the identified experimental modes are symmetric and anti-symmetric and it corresponds to the fact that the structure is symmetric. Losses of symmetry are found for the last two vertical bending modes, V4 and V5. It might be due to the uneven distribution of the stiffness or mass, such as those related to the uncertainty of the stress ribbon deck. Moreover, experimental errors and construction uncertainties (e.g., difference from design drawings and as-built, materials properties and so on) might also have contributed to some irregularity in the mode shapes.

The fundamental frequency was found at 3.59 Hz in vertical bending. Moreover, no lateral bending mode was found. Generally, the usual fundamental frequencies of this kind of structures are in the range (2Hz - 4Hz) even though Živanović et al. (2005) stresses that the range could be different, depending on the rigid surface on which the measurement are done. Modal Assurance Criterion (MAC) values were

Figure 6.3. Experimental mode shapes.

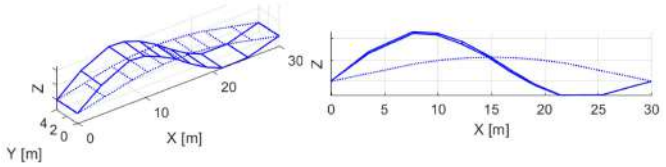

(a) The 1st vertical bending mode (V1): f=3.59 Hz, ξ=0.7%.

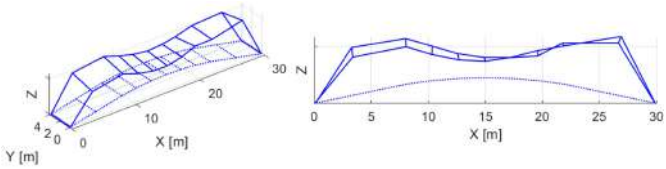

(b) The 2nd vertical bending mode (V2): f=5.28 Hz, ξ=3.9%.

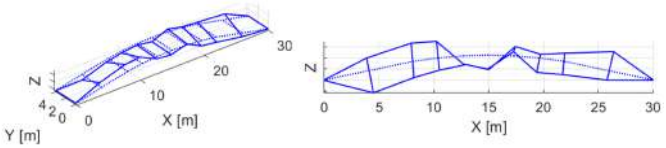

(c) The 1st torsion mode (T1): f=6.91 Hz, ξ=1.6%.

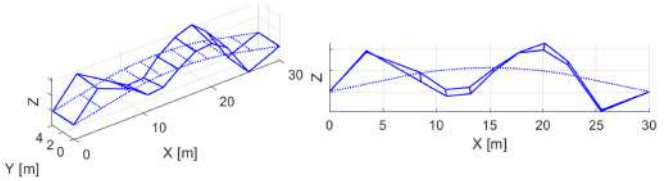

(d) The 3rd vertical bending mode (V3): f=7.79 Hz, ξ=1.2%.

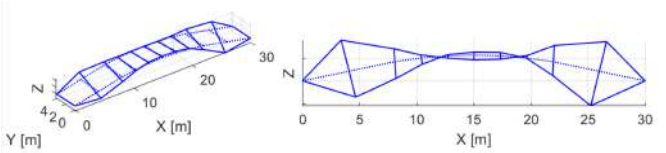

(e) The 2nd torsion mode (T2): f=9.17Hz, ξ=1.1%.

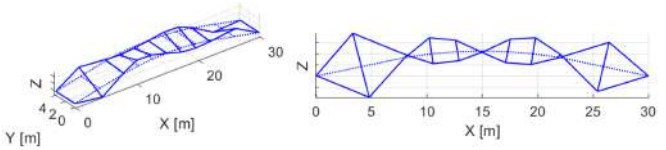

(f) The 3rd torsion mode (T3): f=10.98Hz, ξ=1.0%.

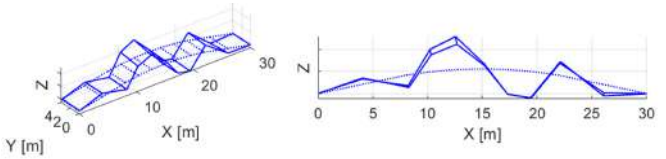

(g) The 4th vertical bending mode (V4): f=14.45 Hz, ξ=0.8%.

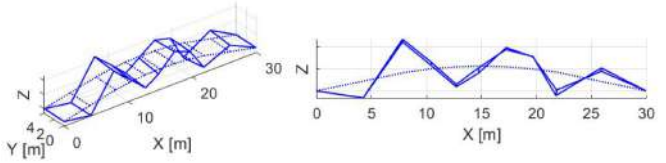

(h) The 5th vertical bending mode (V5): f=14.92 Hz, ξ=0.6%.

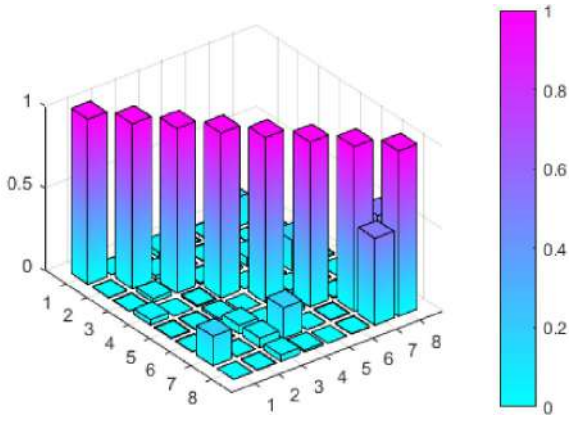

Figure 6.4. The MAC values calculated between the experimental modes (ordered in frequency from low to high).

also calculated between the experimental modes and are reported in Figure 6.4. In general, they were found to be no higher than 0.1 for the first six modes. This suggests that the identified modes were almost linearly independent. Nevertheless, relatively high similarity was found between the 7th and 8th mode, as indicated by the MAC value equal to 0.5. The identified damping ratios ξ varied in the range 0.6%-3.9%.

Nr. of modes	1	2	3	4	5	6	7	8
Type	V1	V2	V3	V4	V5	V6	V7	V8
$\mu(f_{exp,i})$ [Hz]	3.586	5.280	6.911	7.790	9.172	10.982	14.448	14.917
$\sigma(f_{exp,i})$ [Hz]	0.040	0.111	0.195	0.155	0.220	0.185	0.150	0.197
$\mu(\tilde{\sigma}(f_{exp,i})$ [Hz]	0.007	0.076	0.077	0.027	0.037	0.044	0.097	n/a
$\mu(\xi_{exp,i})$ [%]	0.74	3.86	1.61	1.21	1.09	1.01	0.85	0.63
$\sigma(\xi_{exp,i})$ [%]	0.20	1.79	1.64	0.42	0.31	0.42	0.73	0.40
$\mu(\tilde{\sigma}(\xi_{exp,i})$ [%]	0.16	1.41	1.02	0.39	0.46	0.33	0.57	n/a

Table 6.1. Identified natural frequencies $f_{exp,i}$ and damping ratios $\xi_{exp,i}$ of the bridge: $\mu(*)$ is the sample mean of the results across different setups, $\sigma(*)$ is the standard deviation of the results across different setups and $\tilde{\sigma}(*)$ is the standard deviation of the results estimated for a single setup.

Table 6.1 provides a summary of the identification results and the uncertainty quantification of the experimental frequencies and damping ratios. Two approaches were compared with each other for the estimation of standard deviation of the modal parameters. The first one calculates the mean values and standard deviation of the results directly across the eleven setups, as listed in the first and second rows of Table 6.1 for the natural frequencies and fourth and fifth rows for the damping ratios. The second approach is based on the theory of uncertainty propagation derived from the linear property of the Normal distribution. An estimate of the standard deviation can be obtained for the identified modal characteristics in each individual setup by using the covariance-driven SSI algorithm (Reynders et al., 2008); (Reynders et al., 2016). The third and sixth rows of Table 6.1 provides the mean values of the estimated standard deviations for the natural frequencies and damping ratios, respectively, averaged across the eleven setups. The first approach provides a measure of the variance in the experimental results during the whole measurements, while the second one gives an insight into the uncertainty of the results for each setup. Since the modal frequencies of the bridges are influenced by environmental factors, such as temperature, it is expected that the variance of the results during the whole measurements should be larger than those

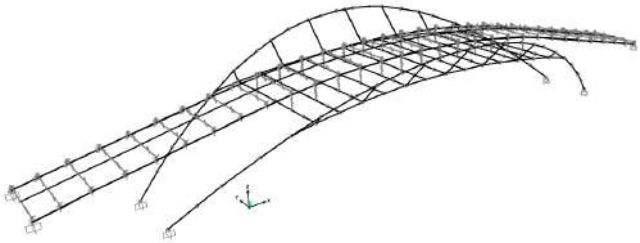

(a) 1st FE model with fixed boundaries and without the abutments.

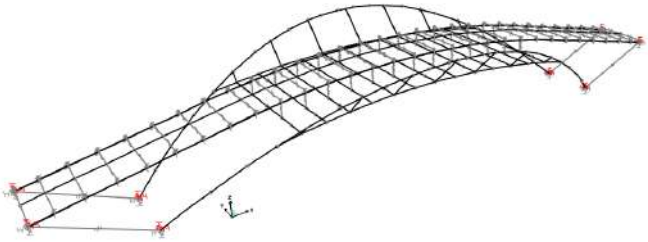

(b) 2nd FE model with soil springs and rigid elements for the abutments.

Figure 6.5. View of the 1st and 2nd FE models with only 3D-beam elements.

estimated within an individual setup. The results in Table 6.1 confirm this point. In particular, the last mode V5 could not be identified when a lower system order is employed in the identification process, which is the case for the second approach of the uncertainty quantification. It might be due to the fact that this mode was not well excited.

6.4 Finite Element modelling

6.4.1 Preliminary modelling and progressive implementation

During the design stage, a preliminary FE model was developed in SAP2000, see Figure 6.5 (a). The arches, cross beams, and prestressed tendons were modelled as 3D-beam elements. The pre-casted concrete slabs were also modeled by longitudinal beams and rigid links were added between the slabs and the tendons to represent the mutual offsets in the real structure. Fixed boundaries on both the main arches springs and the stress ribbons anchors/tendons were adopted. Since the material properties of the bridge are not known, the following first-attempt material properties have been considered in the model: equivalent elastic modulus of concrete E_c=36.750 MPa, density of concrete ρ_c=2500 kg/m^3, equivalent elastic modulus of steel E_s=210.000 MPa, density of steel ρ_s=7850 kg/m^3. Table 6.2 presents the results of this 1st FE model. $\Delta f = (f_{FEM} - f_{EXP})/f_{EXP}$ defines the relative differences between the natural frequencies and the numerical ones. The Modal Assurance Criterion (MAC) is used to express the correspondence between the numerical and experimental modal parameters. It can be noted that the MAC values are higher than 0.6 overall. In particular, the torsion modes T1 and T2 present MAC values equal to 0,6 and also present higher relative differences in frequency compared to the vertical bending modes.

Moreover, the third torsional mode T3, the vertical mode V4 and the vertical mode V5 are not predicted by this model. It was concluded that the model did not

Nr. of modes	type	f_{exp}(Hz)	f_{fem1}(Hz)	Δf_1[%]	MAC_1
1	V1	3.59	4,08	13,8%	0.98
2	V2	5.28	7,35	39,2%	0.81
3	T1	6.91	10,71	55,0%	0.58
4	V3	7.79	9,74	25,0%	0.66
5	T2	9.17	16,24	77,1%	0.62

Table 6.2. Comparison between experimental and numerical modal parameters and the 1st FE model.

reflect the real structure's behaviour as a self-balanced system and a 2nd FE model, depicted in Figure 6.5 (b), was developed. In this 2nd model, fixed constraints were removed and spring elements were introduced in the three-axial directions to represent the soil effects. Additionally, rigid link elements were added between the ends of the deck and the arches springs to simulate the abutments. Table 6.3 reports the natural frequencies of this model compared to the experimental modes.

Nr. of modes	type	f_{exp}(Hz)	f_{fem2}(Hz)	Δf_1[%]	MAC_2
1	V1	3.59	3.71	3.3%	0.99
2	V2	5.28	4.51	-14.5%	0.81
3	T1	6.91	8.21	18.8%	0.61
4	V3	7.79	11.28	44.8%	0.94

Table 6.3. Comparison of the experimental modal data with the results of the 2nd FE model.

Compared to the first model, this second model considers the actual behaviour of the abutments. Despite the lower differences in frequency compared to those observed in the 1st model, in this 2nd model the torsional modes T2 and T3, together with the vertical modes V4 and V5 are not found. It is plausible that, the discrepancies originate from adopting beam-like elements. Since the bridge deck was simplified into longitudinal beam elements, the torsional behaviour of the structure cannot be accurately predicted (Aloisio et al., 2020a); (Aloisio et al., 2020b).

For these reasons, a third FE model was implemented, shown in Figure 6.6. In this model, shell elements, 6 m wide, 1.15 m long and 0.25 m thick, replaced the 3D-beam elements as better representatives of the concrete deck. A sensitivity analysis confirmed that a mesh size of 0.5 m x 0.29 m is the optimum balance between the computational costs and the accuracy of the results. Moreover, the 3D-beams of the CFST arches, cross beams, and hangers, were modelled more accurately according to their actual shape, see Figure 6.6 (b). The materials properties set for the 3rd model are: equivalent elastic modulus of the concrete deck E_c=40.000 MPa, density of the concrete deck ρ_c=2600 kg/m^3, equivalent elastic modulus of the filling concrete inside the tubular steel E_{cf}=42.000 MPa, density of the filling concrete ρ_{cf}=2400 kg/m^3, equivalent elastic modulus of steel E_s=210.000 MPa, density of steel ρ_s=7850 kg/m^3, equivalent elastic modulus of tendons E_t=206.000 MPa, density of tendons ρ_t=7850 kg/m^3. Table 6.4 summarizes the mutual differences in natural frequencies between the experimental and numerical data. Compared to the previous models, the 3rd model determines a tangible improvement in frequency agreement. The relative frequency differences for the

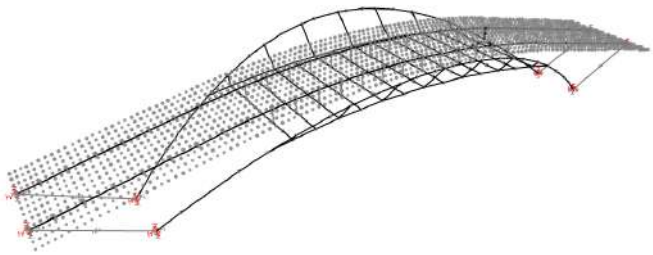

(a) 3rd FE model - standard view.

(b) 3rd FE model - extruded view.

Figure 6.6. View of 3rd FE model with shell elements for the concrete deck.

torsional modes T1 and T2 reduced from 55,0% to -11.01% and from 77.1% to -1.68%, respectively. Interestingly, the third torsional mode T3 was found with a 1.81% relative difference. The vertical bending modes V4 and V5 were instead not found. In this regard, it should be noted that, for these two vertical modes, the MAC values calculated for the experimental modal parameters were quite low, 0.4 and 0.5, respectively.

6.4.2 Parametric updating

In order to minimize the differences between the numerical and experimental results, a sensitivity-based model updating (Fa et al., 2016; Mottershead et al., 2011) of the 3rd FE model was performed. In detail, the following nonlinear least-squares problem was solved:

$$\hat{\boldsymbol{\theta}} = \arg\min_{\boldsymbol{\theta}} J(\boldsymbol{\theta}) = \arg\min_{\boldsymbol{\theta}} \sum_{i} w_{\epsilon,i} \left(\epsilon_{z,i}(\boldsymbol{\theta})\right)^2 \tag{6.1}$$

where $\epsilon z, i$ denotes the residuals between the experimental and numerical modal data z. Herein, only the undamped eigenvalue $z = \lambda$ is involved by considering $\lambda_i = (2\pi f_i)^2$

$$\epsilon_{\lambda_i}(\boldsymbol{\theta}) = \frac{\lambda_i(\boldsymbol{\theta}) - \tilde{\lambda_i}}{\tilde{\lambda_i}} | i \in \{1 - n\} \tag{6.2}$$

where the upper tilde denotes the experimental values and f stands for the natural frequency. In Equation (6.1), $w_{\epsilon,i}$ is the weighting factor. The aforementioned sensitivity-based model updating was implemented into an interactive procedure based on MATLAB and SAP2000. Herein, we assumed $w_{\epsilon,i} = 1$. For this case study, only the natural frequencies were considered for the updating, checking the mode shape correlation at the end since, as compared to the natural frequencies, the identified mode shapes are more prone to the influence of experimental errors, as for the current case study the ambient vibration tests were performed under

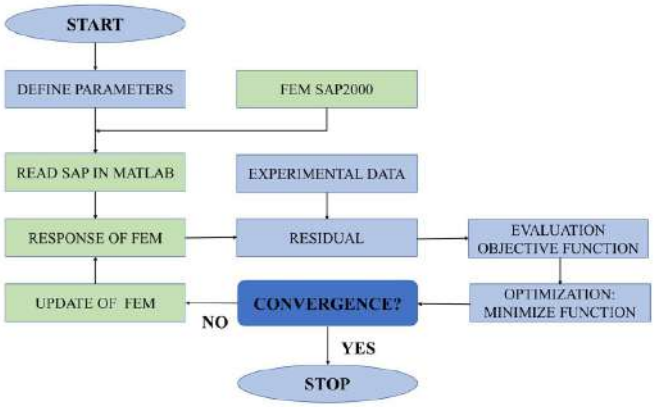

Figure 6.7. Flowchart of the procedure for parametric updating of the FE model.

low level of excitation. For instance, it can be observed the non-smoothness of the mode shape at the middle of the span for T1 mode and the difference of the modal displacements at the upper and lower stream sides of each cross section for V3 mode. Therefore, it was decided to not include the mode shapes into the objective function in order to reduce the effects of experimental errors. Similar practice is found in Brownjohn et al. (2003).

The flowchart in Figure 6.7 shows the procedure for the parametric updating. The stiffness of the springs, the elastic modulus of the deck E_c and the elastic modulus of the tendons E_t were chosen as updating parameters for a total of 8 parameters. The choice was made based on a sensitivity analysis which included also E_{cf} and E_s.

The modal parameters are found to be sensitive to the elastic modulus of steel E_s (arches, hangers and cross beams). Nevertheless, structural steel that is generally used in steel structures exhibits an elastic modulus with a limited variability, approximately equal to 210000 MPa. Therefore, E_s was not included in the updating process. Table 6.4 reports the modal data of the updated 3rd model and Figure 6.8 illustrates the mode shapes. The updated model shows reduced relative differences of frequency for a maximum of -5.85%. MAC values result higher than 0.82.

For an overall comparison between all the implemented models, Equation (6.3) and (6.4) are introduced. Equation (6.3) defines the average relative difference in the natural frequencies and Equation (6.4) defines the average MAC for comparison between experimental and numerical mode shapes.

$$\Delta f = \sqrt{\frac{\sum_i (\Delta f_i)^2}{n_\lambda}} \tag{6.3}$$

$$\text{MAC} = \frac{\sum_i (\text{MAC})}{n_\lambda} \tag{6.4}$$

The average relative difference in frequency for the first model Δf_{FEM1} is 47.58%, for the second model Δf_{FEM2} is 25%, while for the third model, Δf_{FEM3} = 8.71%. A progressive improvement from the 1st model to the 3rd model, which yielded Δf_{FEM3ud}=4,13% after updating, was observed. Similarly, the average MAC from the updated model is 0.91, while the average MAC from the model before updating was 0.85.

These results confirm that the updated 3rd model provides more accurate

Modes	type	f_{exp}(Hz)	f_{fem3}(Hz)	Δf_3[%]	MAC_3	f_{fem3ud}(Hz)	Δf_{3ud}[%]	MAC_3 ud
1	V1	3.59	3.07	-14.25%	0,97	3.38	-5.85%	0,99
2	V2	5.28	4,73	-10.35%	0,94	5.01	-5.02%	0.97
3	T1	6.91	6.15	-11,01%	0,79	6.71	-2.83%	0.89
4	V3	7.79	8.11	4.14%	0,86	8.14	4.53%	0.87
5	T2	9.17	9.02	-1.68%	0,83	9.51	3.74%	0.89
6	T3	10.98	11.18	1.81%	0,71	10.94	-0.41%	0.82

Table 6.4. Comparison of the experimental modal data with the results of the 3rd FE model and the relative updated model.

Figure 6.8. Mode shapes of the updated 3rd FE model. They correspond to the experimental mode shapes.

(a) The 1st vertical bending mode (V1): f=3.38 Hz

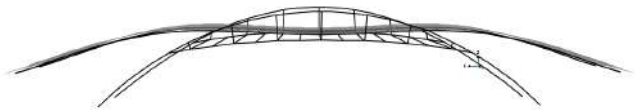

(b) The 2nd vertical bending mode (V2): f=5.01 Hz

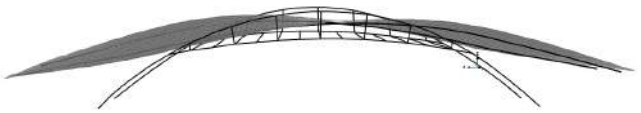

(c) The 1st torsional mode (T1): f=6.71 Hz

(d) The 3rd vertical bending mode (V3): f=8.14 Hz

(e) The 2nd torsional mode (T2): f=9.51 Hz

(f) The 3rd torsional mode (T3): f=10.94 Hz

and reliable predictions of the current modal characteristics of the structure. The values of the parameters obtained after the updating are E_c=57600 MPa and E_t=225100 MPa, which are realistic values for the representing parameters, considering a high strength concrete used for the precast panels which may include also reinforcing bars. The improved modelling and parametric updating minimised the differences between the numerical and experimental modal parameters, endorsing the accuracy of the obtained FE model. At this purpose, a remark should be done: since footbridges are structures having a predominant dimension, simple FE models using only beam elements are generally employed with good results (Pimentel, 1997) to simulate their dynamic behaviour. However, it is observed sometimes that simplified models fail in simulating complex mechanisms and this is the case. Of course, improved FE models can be characterised by several levels of complexity and computational cost (Gregori et al., 2021; Mercuri et al., 2020) and the choice of the most appropriate modelling approach depends on the desired levels of accuracy and simplicity at the same time. In this case, an accurate modelling resolution is required to simulate adequately the behaviour of the structure under ambient vibration.

6.4.3 Effect of non-structural elements in the FE modelling

Generally, the most uncertain and sensitive parameters considered in the updating of footbridges are material properties, boundary conditions, and structural and non-structural elements, which have the potential to influence significantly the dynamic behaviour of the structure (Živanović et al., 2005). In particular, modelling the handrails has been identified as a potential way to increase the stiffness and thus the natural frequencies of footbridges, with an increasing starting from about 0.4% when handrails are added in the model as a uniformly distributed mass, and up to 20% when the handrails are modelled as 3D-beam elements attached to the deck (Pimentel, 1997).

The increase in stiffness and consequently on the natural frequencies that could come from including the handrails in the FE model was investigated. Starting from the generated 3rd model, the handrails were added as continuous tubular steel frames rigidly attached to the deck of the stress-ribbon bridge, following its catenary shape. The Young's modulus of elasticity of the handrails steel was fixed equal to E_s=210000 MPa and the dimensions of the hollow cross sections of the handrails components were set as follows: top and bottom rails: ϕ100 mm x 3.2 mm thickness; infill bars ϕ30 mm x 3.2 mm thickness (considering three per 300 mm). The height of the top rail was 1.10 m above the surface of the deck. Figure 6.9 shows the updated model with handrails (named 4th FE model) and the natural frequencies obtained for this model are presented in Table 6.5 compared to the frequencies obtained for the 3rd model (without handrails).

The improvement obtained by modelling the handrails is evident. The frequency of the first mode showed the higher increase +5.40% and also the frequencies of the other modes increased with a minimum of +0.35% on the T3 mode. Almost certainly, the model with handrails can be more accurate in representing the dynamic behaviour of the stress-ribbon footbridge. To confirm this, the relative differences in frequency between the numerical and experimental frequencies and the MAC values were calculated, and also a new sensitivity-based model updating of the 4th FE model was performed with the same assumptions discussed in the

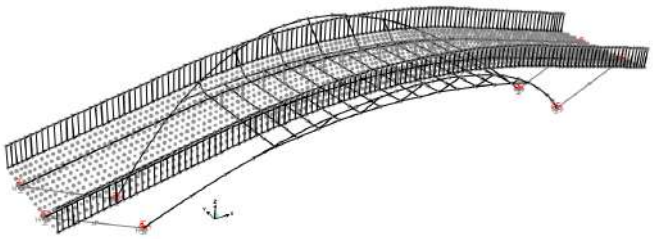

Figure 6.9. View of 4th FE model: handrails rigidly attached to the deck.

Nr. of modes	type	f_{fem3}(Hz)	f_{fem4}(Hz)	Δf[%]
1	V1	3.07	3.24	+5.40
2	V2	4,73	4.76	+0.51
3	T1	6.15	6.20	+0.78
4	V3	8.11	8.38	+3.34
5	T2	9.02	9.14	+1.33
6	T3	11.18	11.22	+0.35

Table 6.5. Comparison between the 3rd FE model (without handrails) and the 4th FE model (with handrails).

previous section. The overall results are presented in Table 6.6.

Modes	type	f_{exp}(Hz)	f_{fem4}(Hz)	Δf_4[%]	MAC_4	f_{fem4ud}(Hz)	Δf_{4ud}[%]	MAC_4 *ud*
1	V1	3.59	3.24	-9.62%	0,98	3.49	-2.56%	0,99
2	V2	5.28	4,76	-9.89%	0,95	4.98	-5.69%	0.97
3	T1	6.91	6.20	-10.31%	0,88	6.90	-0.16%	0.99
4	V3	7.79	8.38	7.62%	0,87	8.22	5.47%	0.87
5	T2	9.17	9.14	-0.38%	0,86	9.27	1.09%	0.91
6	T3	10.98	11.22	2.16%	0,88	10.75	-2.11%	0.92

Table 6.6. Comparison of the experimental modal data with the results of the 4th FE model and the relative updated model.

The values of the parameters obtained after the updating are E_c=64000 MPa and E_t=155800 MPa, which are reliable values for the representing parameters. Actually, the value of E_c refers to the elastic modulus of the entire slab (considering a high strength concrete used for the precast panels, which may include uncertainties due to the thickness of the slab, the contribution of reinforcements, and pavements). In regard to E_t, its value refers to the elastic modulus of tendons which are assumed to be formed by two bundles of 12×Φ15.2 mm monostrands grouted inside galvanised steel tubes. Uncertainties about the real geometry and materials can justify variations in the value of E_t with respect to the hypothesized initial value.

The average difference in frequency for the 4th model after updating is Δf_{FEM4ud}=3.53%, resulting reduced in comparison to the 3rd updated model that reached Δf_{FEM3ud}=4.13%. The average MAC from the 4th updated model is 0.95, while the MAC from the 3rd updated model is 0.91. In civil engineering applications (as in this case), it is worth to note that MAC values as low as 0.8 are anyway acceptable, due to imperfect measurements typically made in noisy environments (Živanović et al., 2005), so the average MAC value obtained is more than acceptable.

The results in Table 6.6 confirm that the updated 4th model provides more accurate and reliable predictions of the modal characteristics of the stress-ribbon footbridge. The parametric updating minimised the differences between the numerical

and experimental modal parameters and thus the obtained accurate FE model can be used as the baseline model for long-term monitoring of the pedestrian bridge.

It can be concluded that a good representation of the dynamic behaviour of the structure is obtained by modelling handrails as attached frames to the deck. The handrails have the potential to affect the natural frequencies and it is recommended to include their stiffness in the analysis.

6.4.4 Effect of prestress on the natural frequencies

In pedestrian bridges subjected to dynamic excitation, the influence of prestress force magnitude on the natural frequencies is of particular interest. However, for existing tendons it is hard to estimate the prestress force and therefore stress and deformations at the specific time when dynamic identification is performed, since the natural frequencies of in-service tendons change when the prestress force changes over time.

The topic is widely debated in literature: some state that the natural frequencies of external prestressed tendons tend to decrease as the magnitude of the prestressing force is increased (Bai-jian et al., 2018; Law and Lu, 2005; Miyamoto et al., 2000); others suggest that the influence of the prestress force on the natural frequencies is negligible (Deák, 1996; Hamed and Frostig, 2006; Reynders et al., 2007). Other researchers, instead, found that the natural frequencies increased as the prestress force in tendons was increased (Noble et al., 2016; Saiidi et al., 1996).

In this study, the prestress force effect on the first-order frequency of the stress-ribbon bridge was investigated, since the first-order vibration is usually the most affected and the most important for the practical engineering. The investigation was conducted by modelling the tendons as "tendon elements" in Sap2000 (a total of 60 elements with equal length to follow the catenary shape of the bridge) varying the prestress force in each tendon in a range from 0 kN to 500 kN (0 kN to 30000 kN on the whole structure). Results are listed in Table 6.7.

Prestress in the element (kN)	Prestress in the structure (kN)	f_{fem}(Hz)	Change rate [%]
0	0	3.49	-
25	1500	3.47	-0.80
50	3000	3.44	-1.52
75	4500	3,42	-2.24
100	6000	3,39	-2.93
250	15000	3,24	-7.36
500	30000	3,02	-13.65

Table 6.7. First-order frequencies of the stress-ribbon pedestrian bridge under different prestress forces.

When the prestress force in the structure increases from 0 kN to 30000 kN, the simulated values of the first-order frequency reduce gradually, reaching a maximum relative difference of -13.65%. The reduction is not constant but decreases at the increasing of the prestress force. Also, it is observed that the prestress effect is much weaker for the higher-order frequencies and thus it is reported just the first-order ones.

As the prestress force changes over time, the natural frequencies of in-service tendons change, and it is hard to estimate the prestress force and therefore the current state of stress and deformations at the specific time when dynamic identification is performed on the structure. So, the modelling of the prestress effect could be

useful to point out the behaviour of the structure in long-time monitoring, and deserves further investigation that could be examined in depth in future works.

6.5 Conclusions

This study presents the outcomes of the dynamic identification and finite element modelling and updating of a butterfly-arch stress-ribbon pedestrian bridge located in Fuzhou, Fujian, China. The structure is not similar to conventional stress-ribbon footbridges, being based on a novel design concept which is the combination of a stress-ribbon deck and a butterfly-arch bridge that provides the solution for a self-anchored structural system. For this reason, an accurate modelling resolution was required to simulate adequately the behaviour of this kind of structure under ambient excitation. Four different FE models with increasing accuracy were developed. The discrepancies originated from adopting beam-like elements were overcome using shell elements to better represent the behaviour of the concrete deck. The modelling of non-structural elements (handrails) contributed to increase the stiffness of the whole system and with the parametric optimisation procedure a satisfactory agreement between the model prediction and the experimental data was achieved. Moreover, it was investigated that with the increment of the prestressing force, a gradual reduction of the natural frequencies can occur. This could be useful to eventually estimate the prestress force and therefore stresses and deformations in long-term monitoring, when dynamic identification of the bridge will be performed again, since the natural frequencies of in-service tendons change when the prestress force changes over time. In the SHM field, this study demonstrates the importance of the modelling strategy in simulating the dynamic behaviour of complex footbridges, as the one considered in this research, in comparison to traditional bridges which can be modelled following simplified modelling procedures. The developed FE model could be used as baseline for long-term monitoring of the bridge and could represent a guide to practitioners and scholars for the modelling and analysis of this particular kind of structures.

[Blank page]

Concluding remarks

Concluding remarks and final observations arising from the experimental works and numerical analyses are drawn here.

The research aimed to develop, implement, and apply innovative technologies for remote and widespread monitoring of the historical and civil structures in general, inspired by the principles of low cost, miniaturization, system energy autonomy, and measurement reliability. Different methods and devices have been proposed for different monitoring purposes. These methods and devices have been developed and tested trough experimental campaigns, in laboratory and in situ, and have been validated with wired traditional techniques for comparison.

In particular, a new method for measuring strains has been presented and discussed in Chapter 3. It consists in a semi-passive wireless technique based on a traditional strain gauge integrated into an electrical circuit together with an RFID tag. In the proposed new method, an interrogating antenna is used to detect the modulation frequency of an electromagnetic signal that varies in accordance with the strain to be measured. The feasibility of this new method has been proved with experimental tests, determining a unique clear relationship among the strain values and the measured frequency changes. Experiments assessed that the tag sensor is able to measure static and dynamic phenomena with vibrations of tens of Hz. In comparison with a traditional strain measuring procedure, the accuracy of the proposed new technique has been proved to be potentially higher, with a maximum interrogating distance of 20 meters in laboratory and outdoor, making this new strain measuring technique suitable for structural monitoring.

The use of commercial UHF-RFID tags (not embedded in antennas) has been investigated to be employed for civil engineering purposes, specifically for the monitoring of out-of-plane displacements (as presented in Chapter 4). The innovation of this research is represented by the novelty of the application of commercial tags, usually used in logistic and other purposes, in civil engineering. The feasibility of the application of this technique was asses by the experimental campaigns carried out first in laboratory, then in situ. The response of the Tags in laboratory environment demonstrated to be very satisfactory, proving that the new application of wireless RFID tags for the monitoring of out-of-plane displacements is feasible and potentially very reliable. In situ experiments showed a weaker response of the Tags which registered displacements lower than those recorded by the wired transducer used as reference. The environmental conditions are responsible for this result: the high presence of metal in the environment affected negatively

the transmission of the electromagnetic signal, modifying the signal phases and consequently the indirect measurements of displacements. Technology limits related to environment interference by metallic objects can be overcome with a specific design of the Tags for engineering purposes, guaranteeing the same advantages (cost-effectiveness, small size) of the tags currently available on the market. In conclusion, the application of UHF-RFID tags in civil engineering applications is promising and opens up new scenarios for the design of new wireless devices suitable to meet the required needs. The use of this new measurement technology allows the advantage of a wireless, low-cost, non-invasive, and widespread monitoring.

The study described in Chapter 5 demonstrated that the new wireless RFID sensor for crack width monitoring gave a discrete response. Compared to traditional crack-width measurement procedures, the proposed new technique results potentially more suitable. The interrogation distance in this raw state reached 1.5 m, which is a lot, and could be extended more to allow the positioning of these devices in points difficult to access with traditional wired ones.

It should be considered that these devices are in a raw form and require technological development in order to be applied on large scale, but the potential in structural monitoring could be very high. Many difficult aspects like the strong influence of metal should be taken into account and can be overcome in the next steps of design of the sensors. Moreover the proposed wireless sensors are made with low cost components and this represents of course and advantage in widespread monitoring. Further investigation is surely required and deserve to be carried on in the next future.

In this thesis a large-scale approach to wireless structural monitoring has been also investigated. A sensor network with commercial wireless tri-axial MEMS accelerometers was deployed on the deck of a butterfly-arch stress-ribbon pedestrian bridge located in Fuzhou, Fujian, China, to record the structural response under ambient vibration and perform dynamic identification, finite element modelling and parametric updating. Different FE models with increasing accuracy were required to simulate adequately the behaviour of this specific footbridge. The most accurate model has been developed to be used as baseline for long-term monitoring of the bridge. The modelling of non-structural elements (handrails) and shell elements for the concrete deck contributed to increase the stiffness of the whole system and with the parametric optimization procedure a satisfactory agreement between the model prediction and the experimental data was achieved. Moreover, it has been investigated that with the increment of the prestressing force, a gradual reduction of the natural frequencies can occur. This could be useful to eventually estimate the prestress force and therefore stresses and deformations in long-term monitoring, when dynamic identification of the bridge will be performed again, since the natural frequencies of in-service tendons change when the prestress force changes over time. In the SHM field, this study demonstrates the importance of the modelling strategy in simulating the dynamic behaviour of complex structures, as the one considered in this research, in comparison to traditional ones which can be modelled following simplified modelling procedures.

7.1 Future research

Important and promising results have been achieved and presented in this work. The proposed techniques of measurement and devices are quite efficient, but surely deserve further investigation to overcome some limits. Proposals for future research include surely the improvement of the proposed wireless measurement techniques and devices.

In particular, objectives for a future research will include:

- the increase of the measuring distances currently reached by the devices;
- a better design, a targeted choice of the hardware components of the tag sensors, in order to eliminate any interference (most of all the interference of metallic parts) that may limit their operation, and adapt them to specific measurement needs with high accuracy and precision;
- perform large-scale applications of the proposed devices for widespread and long-term monitoring;
- the proposal of new measuring thechniques and devices for new monitoring purposes.

References

Aloisio, A., Alaggio, R., and Fragiacomo, M. (2020a). Dynamic identification and model updating of full-scale concrete box girders based on the experimental torsional response. *Construction and Building Materials*, 264:120146.

Aloisio, A., Alaggio, R., and Fragiacomo, M. (2020b). Time-domain identification of the elastic modulus of simply supported box girders under moving loads: Method and full-scale validation. *Engineering Structures*, 215:110619.

Angiolilli, M., Gregori, A., and Vailati, M. (2020). Lime-based mortar reinforced by randomly oriented short fibers for the retrofitting of the historical masonry structure. *Materials*, 13(16):3462.

Bai-jian, T., Fei, W., and Song, C. (2018). Effect of prestress force on natural bending frequency of external prestressed steel beams. *The Open Civil Engineering Journal*, 12(1).

Bleicher, A., Schlaich, M., Fujino, Y., and Schauer, T. (2011). Model-based design and experimental validation of active vibration control for a stress ribbon bridge using pneumatic muscle actuators. *Engineering structures*, 33(8):2237–2247.

Briseghella, B., Chen, A., Li, X., Zordan, T., Lan, C., and Mazzarolo, E. (2012). Analysis on applicability of health monitoring techniques on a curved cable stayed bridge. In *Bridge Maintenance, Safety, Management, Resilience and Sustainability–Proceedings of the Sixth International Conference on Bridge Maintenance, Safety and Management*, pages 2617–2624.

Brownjohn, J., Tjin, S., Tan, G., Tan, B., and Chakraboorty, S. (2004). A structural health monitoring paradigm for civil infrastructure. In *1st FIG International Symposium on Engineering Surveys for Construction Works and Structural Engineering*, volume 28.

Brownjohn, J. M. W., Moyo, P., Omenzetter, P., and Lu, Y. (2003). Assessment of highway bridge upgrading by dynamic testing and finite-element model updating. *Journal of Bridge Engineering*, 8(3):162–172.

Bungey, J. H. and Grantham, M. G. (2006). *Testing of concrete in structures*. Crc Press.

Caetano, E. and Cunha, A. (2004). Experimental and numerical assessment of the dynamic behaviour of a stress-ribbon footbridge. *Structural concrete*, 5(1):29–38.

Caetano, E., Cunha, Á., Magalhães, F., and Moutinho, C. (2010). Studies for controlling human-induced vibration of the pedro e inês footbridge, portugal. part 1: Assessment of dynamic behaviour. *Engineering Structures*, 32(4):1069–1081.

Caizzone, S. and DiGiampaolo, E. (2015). Wireless passive rfid crack width sensor for structural health monitoring. *IEEE Sensors Journal*, 15(12):6767–6774.

Caizzone, S., DiGiampaolo, E., and Marrocco, G. (2014). Wireless crack monitoring by stationary phase measurements from coupled rfid tags. *IEEE Transactions on Antennas and Propagation*, 62(12):6412–6419.

Caizzone, S., DiGiampaolo, E., and Marrocco, G. (2015). Constrained pole-zero synthesis of phase-oriented rfid sensor antennas. *IEEE Transactions on Antennas and Propagation*, 64(2):496–503.

Cara, J., Magdaleno, A., and Lorenzana, A. (2017). Input/output versus output only modal ana-lysis of a stress-ribbon footbridge. In *IOMAC 2017–7th Int. Oper. Modal Anal. Conf.*

Catbas, F. N., Brown, D. L., and Aktan, A. E. (2004). Parameter estimation for multiple-input multiple-output modal analysis of large structures. *Journal of engineering mechanics*, 130(8):921–930.

Celebi, M. (2002). Seismic instrumentation of buildings (with emphasis on federal buildings). Technical report, Report No. 0-7460-68170, United States Geological Survey, Menlo Park, CA.

Chang, P. C., Flatau, A., and Liu, S. (2003). Health monitoring of civil infrastructure. *Structural health monitoring*, 2(3):257–267.

Cunha, Á., Caetano, E., Moutinho, C., and Magalhães, F. (2005). Damping identification in a stress-ribbon footbridge. *Structural Dynamics-EURODYN 2005, Vols 1-3*.

Deák, G. (1996). Discussion of "prestress force effect on vibration frequency of concrete bridges" by m. saiidi, b. douglas, and s. feng. *Journal of Structural Engineering*, 122(4):458–459.

Di Giampaolo, E., Di Carlofelice, A., and Gregori, A. (2016). An rfid-enabled wireless strain gauge sensor for static and dynamic structural monitoring. *IEEE sensors journal*, 17(2):286–294.

Dyke, S. J., Caicedo, J. M., and Johnson, E. A. (2000). Monitoring of a benchmark structure for damage identification. In *Proceedings of the Engineering Mechanics Speciality Conference*, pages 21–24. Austin, TX.

European Committee for Standardization, B. (2007). Methods of test for mortar for masonry—part 11. *Belgium*.

Fa, G., He, L., Fenu, L., Mazzarolo, E., Briseghella, B., and Zordan, T. (2016). Comparison of direct and iterative methods for model updating of a curved cable-stayed bridge using experimental modal data. In *Proceedings of the IABSE Conference, Guangzhou, China*, pages 8–11.

Farinholt, K. M., Miller, N., Sifuentes, W., MacDonald, J., Park, G., and Farrar, C. R. (2010). Energy harvesting and wireless energy transmission for embedded shm sensor nodes. *Structural Health Monitoring*, 9(3):269–280.

Farrar, C. and Worden, K. (2006). An introduction to structural health monitoring. *Philosophical Transactions of the Royal Society A: Mathematical, Physical and Engineering Sciences*, 365:303 – 315.

Feldman, M. (2008). Hivoss—human-induced vibrations of steel structures. *Office for Official Publications of the European Communities, Luxembourg.*

Gasco, F., Feraboli, P., Braun, J., Smith, J., Stickler, P., and DeOto, L. (2011). Wireless strain measurement for structural testing and health monitoring of carbon fiber composites. *Composites Part A: Applied Science and Manufacturing*, 42(9):1263–1274.

Gregori, A., Castoro, C., Mercuri, M., and Angiolilli, M. (2021). Numerical modelling of the mechanical behaviour of rubbercrete. *Computers & Structures*, 242:106393.

Hamed, E. and Frostig, Y. (2006). Natural frequencies of bonded and unbonded prestressed beams–prestress force effects. *Journal of sound and vibration*, 295(1-2):28–39.

He, L., Zhang, Z., Marano, G. C., Briseghella, B., Xue, J., and Ni, Z. (2019). Dynamic characterization of a stress ribbon and butterfly arch pedestrian bridge using wireless measurements. In *Proceedings of ARCH 2019: 9th International Conference on Arch Bridges*, volume 11, page 395. Springer Nature.

Hu, W.-H., Caetano, E., and Cunha, Á. (2013). Structural health monitoring of a stress-ribbon footbridge. *Engineering Structures*, 57:578–593.

Ibrahim, A. and Cumming, D. (2011). Passive single chip wireless microwave pressure sensor. *Sensors and Actuators A: Physical*, 165(2):200–206.

Živanović, S., Pavic, A., and Reynolds, P. (2005). Vibration serviceability of footbridges under human-induced excitation: a literature review. *Journal of Sound and Vibration*, 279(1):1–74.

Jang, S.-D., Kang, B.-W., and Kim, J. (2012). Frequency selective surface based passive wireless sensor for structural health monitoring. *Smart Materials and Structures*, 22(2):025002.

Jang, S.-D. and Kim, J. (2012). Passive wireless structural health monitoring sensor made with a flexible planar dipole antenna. *Smart materials and structures*, 21(2):027001.

Jeong, M., Bae, J.-G., and Koh, B.-H. (2010). A feasibility study of damage tracking through the diffusive communication of wireless sensors. *International Journal of Precision Engineering and Manufacturing*, 11(1):23–29.

Johnson, G. P. (2006). *Structural health monitoring systems for civil and architectural structures: LVDT-taut-wire baselines, crack monitoring devices, and strain based deflection monitoring algorithms*, volume 68.

Kesavan, A., John, S., and Herszberg, I. (2008). Strain-based structural health monitoring of complex composite structures. *Structural Health Monitoring*, 7(3):203–213.

Köppe, E. and Bartholmai, M. (2011). Wireless sensor network with temperature compensated measuring technology for long-term structural health monitoring of buildings and infrastructures. *Procedia Engineering*, 25:1032–1036.

Kuang, K., Cantwell, W., Thomas, C., et al. (2003). Crack detection and vertical deflection monitoring in concrete beams using plastic optical fibre sensors. *Measurement Science and Technology*, 14(2):205.

Law, S. and Lu, Z. (2005). Time domain responses of a prestressed beam and prestress identification. *Journal of sound and vibration*, 288(4-5):1011–1025.

Lecompte, D., Vantomme, J., and Sol, H. (2006). Crack detection in a concrete beam using two different camera techniques. *Structural Health Monitoring*, 5(1):59–68.

Lee, D. and Ryu, S. (1999). The influence of fiber aspect ratio on the tensile and tear properties of short-fiber reinforced rubber. *ICCM12: Paris, France*.

Lin, J.-T., Walsh, K. W., Jackson, D., Aebersold, J., Crain, M., Naber, J. F., and Hnat, W. P. (2007). Development of capacitive pure bending strain sensor for wireless spinal fusion monitoring. *Sensors and Actuators A: Physical*, 138(2):276–287.

Liu, L. and Yuan, F. (2008). Wireless sensors with dual-controller architecture for active diagnosis in structural health monitoring. *Smart Materials and Structures*, 17(2):025016.

Liu, T., Zhang, Q., Zordan, T., and Briseghella, B. (2016). Finite element model updating of canonica bridge using experimental modal data and genetic algorithm. *Structural Engineering International*, 26(1):27–36.

Lynch, J. P. and Loh, K. J. (2006). A summary review of wireless sensors and sensor networks for structural health monitoring. *Shock and Vibration Digest*, 38(2):91–130.

Lynch, J. P., Sundararajan, A., Law, K. H., Kiremidjian, A. S., Kenny, T., and Carryer, E. (2003). Embedment of structural monitoring algorithms in a wireless sensing unit. *Structural Engineering and Mechanics*, 15(3):285–297.

Mascarenas, D. D., Flynn, E. B., Todd, M. D., Overly, T. G., Farinholt, K. M., Park, G., and Farrar, C. R. (2010). Development of capacitance-based and impedance-based wireless sensors and sensor nodes for structural health monitoring applications. *Journal of Sound and Vibration*, 329(12):2410–2420.

Melik, R., Perkgoz, N. K., Unal, E., Puttlitz, C., and Demir, H. V. (2008). Bio-implantable passive on-chip rf-mems strain sensing resonators for orthopaedic applications. *Journal of Micromechanics and Microengineering*, 18(11):115017.

Melik, R., Unal, E., Kosku Perkgoz, N., Puttlitz, C., and Demir, H. V. (2009). Flexible metamaterials for wireless strain sensing. *Applied Physics Letters*, 95(18):181105.

Mercuri, M., Pathirage, M., Gregori, A., and Cusatis, G. (2020). Computational modeling of the out-of-plane behavior of unreinforced irregular masonry. *Engineering Structures*, 223:111181.

Mitchell, K., Sana, S., Balakrishnan, V. S., Rao, V. S., and Pottinger, H. J. (1999). Microsensors for health monitoring of smart structures. In *Smart Structures and Materials 1999: Smart Electronics and MEMS*, volume 3673, pages 351–358. International Society for Optics and Photonics.

Miyamoto, A., Tei, K., Nakamura, H., and Bull, J. W. (2000). Behavior of prestressed beam strengthened with external tendons. *Journal of Structural Engineering*, 126(9):1033–1044.

Mohammad, I. and Huang, H. (2011). An antenna sensor for crack detection and monitoring. *Advances in Structural Engineering*, 14(1):47–53.

Mottershead, J. E., Link, M., and Friswell, M. I. (2011). The sensitivity method in finite element model updating: A tutorial. *Mechanical systems and signal processing*, 25(7):2275–2296.

Noble, D., Nogal, M., Pakrashi, V., et al. (2016). The effect of prestress force magnitude and eccentricity on the natural bending frequencies of uncracked prestressed concrete beams. *Journal of Sound and Vibration*, 365:22–44.

Ou, J. (2006). Research and practice of intelligent sensing technologies in civil structural health monitoring in the mainland of china. In *Nondestructive Evaluation and Health Monitoring of Aerospace Materials, Composites, and Civil Infrastructure V*, volume 6176, page 61761D. International Society for Optics and Photonics.

Paggi, C., Occhiuzzi, C., and Marrocco, G. (2013). Sub-millimeter displacement sensing by passive uhf rfid antennas. *IEEE Transactions on Antennas and Propagation*, 62(2):905–912.

Pakravan, H., Latifi, M., and Jamshidi, M. (2017). Hybrid short fiber reinforcement system in concrete: A review. *Construction and building materials*, 142:280–294.

Park, G., Rosing, T., Todd, M. D., Farrar, C. R., and Hodgkiss, W. (2008). Energy harvesting for structural health monitoring sensor networks. *Journal of Infrastructure Systems*, 14(1):64–79.

Peeters, B. and De Roeck, G. (1999). Reference-based stochastic subspace identification for output-only modal analysis. *Mechanical systems and signal processing*, 13(6):855–878.

Pimentel, R. (1997). Vibrational performance of pedestrian bridges due to human-induced loads. *Ph.D. Thesis, Univeristy of Sheffield, Sheffield, UK*.

Ravet, F., Briffod, F., Glisic, B., Nikles, M., and Inaudi, D. (2009). Submillimeter crack detection with brillouin-based fiber-optic sensors. *IEEE Sensors Journal*, 9(11):1391–1396.

Reynders, E., Maes, C., Lombaert, G., and Roeck, G. D. (2016). Uncertainty quantification in operational modal analysis with stochastic subspace identification: validation and applications. *Mechanical Systems and Signal Processing*, 66-67:13–30.

Reynders, E., Pintelon, R., and Roeck, G. D. (2008). Uncertainty bounds on modal parameters obtained from stochastic subspace identification. *Mechanical Systems and Signal Processing*, 22(4):948–969.

Reynders, E., Roeck, G. D., Gundes Bakir, P., and Sauvage, C. (2007). Damage identification on the tilff bridge by vibration monitoring using optical fiber strain sensors. *Journal of engineering mechanics*, 133(2):185–193.

Reynders, E., Schevenels, M., and De Roeck, G. (2011). Macec 3.2: A matlab toolbox for experimental and operational modal analysis-user's manual. *Katholieke Universiteit, Leuven.*

Roy, S., Jandhyala, V., Smith, J. R., Wetherall, D. J., Otis, B. P., Chakraborty, R., Buettner, M., Yeager, D. J., Ko, Y.-C., and Sample, A. P. (2010). Rfid: From supply chains to sensor nets. *Proceedings of the IEEE*, 98(9):1583–1592.

Saad, S. M. (2011). *A wireless system for crack monitoring in concrete structures.* University of Northern Iowa.

Saiidi, M., Douglas, B., and Feng, S. (1996). Prestress force effect on vibration frequency of concrete bridges. discussion and closure. *Journal of Structural Engineering*, 122(4).

Sétra, F. (2006). Assessment of vibrational behaviour of footbridges under pedestrian loading. *Technical guide SETRA, Paris, France.*

SMbulletin (2002). Wireless structural damage monitoring. *Smart Materials Bulletin*, 2002.

Son, B., Her, Y.-s., and Kim, J.-G. (2006). A design and implementation of forest-fires surveillance system based on wireless sensor networks for south korea mountains. *International Journal of Computer Science and Network Security (IJCSNS)*, 6(9):124–130.

Soria, J. M., Díaz, I. M., García-Palacios, J. H., and Ibán, N. (2016). Vibration monitoring of a steel-plated stress-ribbon footbridge: uncertainties in the modal estimation. *Journal of Bridge Engineering*, 21(8):C5015002.

Spencer, B. (2003). Opportunities and challenges for smart sensing technology. In *1st International Conference on Structural Health Monitoring and Intelligent Infrastructure, SHMII-1'2003*, pages 65–71.

Steel, B. (1978). concrete and composite bridges. specification for loads, bs 5400: Part 2. *British Standard Institution.*

Straser, E., Kiremidjian, A., Meng, T., and Redlefsen, L. (1998). A modular, wireless network platform for monitoring structures. In *Proceedings-SPIE The International Society for Optical Engineering*, volume 1, pages 450–456. Citeseer.

Strasky, J. (2005). *Stress ribbon and cable-supported pedestrian bridges*. Thomas Telford.

Strasky, J. (2010). Stress-ribbon pedestrian bridges supported by arches. *Concrete international*, 32(5):28–33.

Tata, U., Deshmukh, S., Chiao, J., Carter, R., and Huang, H. (2009). Bio-inspired sensor skins for structural health monitoring. *Smart Materials and Structures*, 18(10):104026.

Yao, W., Li, J., and Wu, K. (2003). Mechanical properties of hybrid fiber-reinforced concrete at low fiber volume fraction. *Cement and concrete research*, 33(1):27–30.

Yu, Y., Li, H., and Ou, J. (2004a). Wireless acceleration sensor used for civil engineering structure monitoring and its integration technique. In *The 3rd International Symposium on Instrumentation Science and Technology*, volume 1, pages 741–748.

Yu, Y., LI, H.-w., and Ou, J.-p. (2004b). Design and development of wireless acceleration sensor applied to civil engineering structure monitoring. *Journal of Transcluction Technology*, 3.

Yu, Y. and Ou, J. (2008). Wireless sensing experiments for structural vibration monitoring of offshore platform. *Frontiers of Electrical and Electronic Engineering in China*, 3(3):333–337.

Zordan, T., Briseghella, B., and Liu, T. (2014). Finite element model updating of a tied-arch bridge using douglas-reid method and rosenbrock optimization algorithm. *Journal of Traffic and Transportation Engineering (English Edition)*, 1(4):280–292.

List of Terms

CCD charge-coupled device.

CFST Concrete-Filled Steel Tubular.

CW continuous wave.

FE Finite Element.

IC integrated circuit.

MAC Modal Assurance Criterion.

MEMS Micro-electromechanical Systems.

OMA Operational Modal Analysis.

RFID Radio-Frequency IDentification.

RSSI Received Signal Strength Indicator.

SHM Structural Health Monitoring.

SSI Stochastic Subspace Identification.

UHF Ultra High Frequency.

WSHMS Wireless Structural Health Monitoring Systems.

WSN Wireless Sensor Network.

List of Publications

The following papers are indexed on ISI/Scopus and/or of A level in ANVUR ranking.

- He, L., **Castoro, C.**, Aloisio, A., Zhang, Z., Marano, G.C., Gregori, A., Deng, C., Briseghella, B.(2021). *Dynamic assessment, FE modelling and parametric updating of a butterfly-arch stress-ribbon pedestrian bridge.* Structure and Infrastructure Engineering. DOI:10.1080/15732479.2021.1995444.
- Gregori, A., & **Castoro, C.**(2021). *Modelling mechanical properties and bond behaviour of rubbercrete.* Construction and Building Materials, 305, 124735.
- Gregori, A., **Castoro, C.**, Venkiteela, G. (2021). *Predicting the compressive strength of rubberized concrete using artificial intelligence methods.* Sustainability, 13(14), 7729.
- Gregori, A., **Castoro, C.**, Mercuri, M., Angiolilli, M. (2021). *Numerical modelling of the mechanical behaviour of rubbercrete.* Computers & Structures, 242, 106393.
- Gregori, A., **Castoro, C.**, Mercuri, M., Angiolilli, M. (2020). *Modeling the Mechanical Response of Rubberised Concrete.* Advanced Structured Materials. Developments and Novel Approaches in Biomechanics and Metamaterials, 132, 341.
- Gregori, A., **Castoro, C.**, Marano, G. C., Greco, R. (2019). *Strength reduction factor of concrete with recycled rubber aggregates from tires.* Journal of Materials in Civil Engineering, 31(8), 04019146.
- Gregori, A., Di Giampaolo, E., Di Carlofelice, A., **Castoro, C.**(2019). *Presenting a New Wireless Strain Method for Structural Monitoring: Experimental Validation.* Journal of Sensors, 5370838.

International and national conference papers

- Sciomenta, M., DeSantis, Y., **Castoro, C.**, Spera, L., Rinaldi, V., Bedon, C., Fragiacomo, M., Gregori, A. *Finite elements analyses of timber-concrete and timber-rubberised concrete specimens with inclined screws.* WCTE-2021 Conference.
- Fu, H., **Castoro, C.**, Zhou, L. (2020). *Finite element simulation study on mechanical properties of FRP-concrete-steel double-tube composite long columns to prevent engineering risks.* 7^{th} Young Researchers' Round Table 2020
- Gregori, A., **Castoro, C.**, Mercuri, M., Angiolilli, M. (2019). *Using rubber aggregates from tyres in concrete: a numerical investigation.* In Proceedings of the 5^{th} Workshop on New Boundaries of Structural Concrete 2019, ACI Italy Chapter.
- Gregori, A., **Castoro, C.**, Marano, G.C., Greco, R. (2019). *Compressive Strength of Concrete Containing Rubber Aggregates from Waste Tyres.* In Proceedings of the 5^{th} Workshop on New Boundaries of Structural Concrete 2019, ACI Italy Chapter.
- Gregori, A., **Castoro, C.**, Venkiteela, G. (2019). *Advanced modeling of rubbercrete compressive strength based on experimental works.* CIVIL-COMP-OPTI 2019
- Gregori, A., **Castoro, C.**, Mercuri, M., Angiolilli, M. (2019). *Modelling the mechanical behaviour of concrete with scrap tyre rubber aggregates.* CIVIL-COMP 2019
- Gregori, A., Di Giampaolo, E., Di Carlofelice, A., **Castoro, C.**(2019). "*Structural monitoring: a new wireless strain measuring method.* Conference proceedings ANIDIS 2019, Ascoli Piceno (Italy), Pisa University press, 2-9.
- **Castoro, C.**(2018) *Mitigation of the risk: area and rural building heritage of Murgia.* Conference Poster, 5^{th} Young Researchers' Round Table 2018, L'Aquila (Italy).

La borsa di dottorato è stata cofinanziata con risorse del Programma Operativo Nazionale 2014-2020 (CCI 2014IT16M2OP005), Fondo Sociale Europeo, Azione I.1 “Dottorati Innovativi con caratterizzazione industriale”